Modeling Approaches to Characterize the Disposition of Monoclonal Antibodies

from Detailed PBPK Models to Classical Compartment Models

Dissertation zur Erlangung des akademischen Grades
eines Doktors der Naturwissenschaften (Dr. rer. nat.)
an der Mathematisch-Naturwissenschaftlichen Fakultät
der Universität Potsdam

vorgelegt von

Ludivine Fronton

November 2014

A la mémoire de ma Sorcière Bien-Aimée, mon Mentor, ma Confidente,

Tante Hélène Bagot-Robert.

1954 – 2012

Acknowledgments

I first express my gratitude to my PhD supervisor, Prof. Dr. Wilhelm Huisinga for the grand opportunity he offered me to join the mathematicians' world, for his trust, support and guidance to carry out this challenging but how much rewarding PhD project. My PhD work could reach maturity thanks to Wilhelm's constant and unerring commitment to high standard work.

I also thank my co-supervisor, Prof. Dr. Charlotte Kloft for valuable discussions and comments on my PhD project and for her support to foster a continual collaboration between the groups of the PharMetrX program from Potsdam University and Free University. I am also thankful to my mentor, Dr. Stefanie Reif for offering me the opportunity to present my PhD project at Bayer and for bringing the perspective from industry into my work. I am very grateful to Dr. Thierry Lavé, Dr. Antje Walz and colleagues from the Modeling & Simulation group at Roche, Basel, for their support and to Drs. Stefanie Bendels and Michael Gertz for their help for the German translation of the abstract. I greatly thank Prof. Dr. Joachim Selbig and Prof. Dr. Michel Tod for reviewing this PhD thesis.

I warmly thank my PhD colleagues from the PharMetrX program at Potsdam University and at Free University for our regular, stimulating and always lively interactions both professionally and personally. My warm thanks go to Sathej Gopalakrishnan for being such a wonderful office mate and a true friend. I also want to greet Dr. Buket Benek Gursoy and Dr. Fernando Lopez who I met at the Hamilton Institute during the first months of my PhD, in Ireland, and who are dear friends.

I want to thank my dancing friends, Romuald Wokam for being such a fabulous salsa partner and friend, the Basel Kiz' Team, Djazia Djaffer, Eva Lopez, Didier Fortes, Rafael Lahoz, Gilles Lollia, Philippe Moniz and Arnaud Wustmann – c'est un véritable bonheur de les avoir rencontrés. I also thank Mirian Liu for her patience and support during the time of PhD writing. My warm feelings go to Julia and Gabrielle Tarsten who welcomed me in Berlin and supported me as I were part of their admirable family. My deep thanks go to Henrik Åkesson for his constant supportive and carrying friendship for the past ten years.

Finally, my greatest gratitude goes to my family. Je remercie mes parents Françoise et Bernard, ma soeur Pauline et mon frère Adrien, de leur soutien et de leur présence aux moments importants. Je remercie aussi immensément Mamie de sa grande sagesse qui guide chacun de mes pas.

Abstract

Monoclonal antibodies (mAbs) are engineered immunoglobulins G (IgG) used for more than 20 years as targeted therapy in oncology, infectious diseases and (auto-)immune disorders. Their protein nature greatly influences their pharmacokinetics (PK), presenting typical linear and non-linear behaviors.

While it is common to use empirical modeling to analyze clinical PK data of mAbs, there is neither clear consensus nor guidance to, on one hand, select the structure of classical compartment models and on the other hand, interpret mechanistically PK parameters. The mechanistic knowledge present in physiologically-based PK (PBPK) models is likely to support rational classical model selection and thus, a methodology to link empirical and PBPK models is desirable. However, published PBPK models for mAbs are quite diverse in respect to the physiology of distribution spaces and the parameterization of the non-specific elimination involving the neonatal Fc receptor (FcRn) and endogenous IgG (IgGendo). The remarkable discrepancy between the simplicity of biodistribution data and the complexity of published PBPK models translates in parameter identifiability issues.

In this thesis, we address this problem with a simplified PBPK model—derived from a hierarchy of more detailed PBPK models and based on simplifications of tissue distribution model. With the novel tissue model, we are breaking new grounds in mechanistic modeling of mAbs disposition: We demonstrate that binding to FcRn is indeed linear and that it is not possible to infer which tissues are involved in the unspecific elimination of wild-type mAbs. We also provide a new approach to predict tissue partition coefficients based on mechanistic insights: We directly link tissue partition coefficients (K_{tis}) to data-driven and species-independent published antibody biodistribution coefficients (ABC_{tis}) and thus, we ensure the extrapolation from pre-clinical species to human with the simplified PBPK model. We further extend the simplified PBPK model to account for a target, relevant to characterize the non-linear clearance due to mAb-target interaction.

With model reduction techniques, we reduce the dimensionality of the simplified PBPK model to design 2-compartment models, thus guiding classical model development with physiological and mechanistic interpretation of the PK parameters.

We finally derive a new scaling approach for anatomical and physiological parameters in PBPK models that translates the inter-individual variability into the design of mechanistic covariate models with direct link to classical compartment models, specially useful for PK population analysis during clinical development.

Publications

Parts of this thesis have been published during the PhD.

Chapters 3 to 5 and Section 6.2 of Chapter 6 have been published in The journal of Pharmacokinetics and Pharmacodynamics in collaboration with Sabine Pilari and Wilhelm Huisinga, with the title: "Monoclonal antibody disposition: a simplified PBPK model and its implications for the derivation and interpretation of classical compartment models".

Sections 7.1, 7.2 and 7.5 are part of a paper published in CPT: Pharmacometrics & Systems Pharmacology in collaboration with Wilhelm Huisinga, Alexander Solms and Sabine Pilari with the title: "Modeling Interindividual Variability in Physiologically Based Pharmacokinetics and Its Link to Mechanistic Covariate Modeling".

Acronyms

ABC antibody biodistribution coefficient

AUC area under the curve

Bmax maximal concentration of drug that can distribute into the receptor system

BSA body surface area

BW body weight

CLint intrinsic clearance

CLplasma plasma clearance

CO cardiac output

E extraction ratio

eMM extended Michaelis-Menten

Fab fragment of antigen binding

Fc fragment crystallizable

FcRn neonatal Fc Receptor

FcRn-KO FcRn-knockout

FDA Food and Drug Administration

IIV inter individual variability

IgG immunoglobulin G

IgGendo endogenous IgG

K partition coefficient

Km Michaelis-Menten constant

KO knockout

mAb monoclonal antibody

NCA non-compartmental analysis

NHP non human primate

ODE ordinary differential equation

OW organ weight

PBPK physiologically-based pharmacokinetic

PD pharmacodynamcis

PK pharmacokinetics

RME receptor-mediated endocytosis

SMD small molecule drug

TMDD target mediated drug disposition

WT wild type

List of Figures

List of Tables

Contents

General introduction

Since the concept of the magic bullet introduced by Paul Ehrlich [1] in 1878, bio-pharmaceutical products and in particular monoclonal antibodies (mAbs) have been exponentially used as analytical, diagnostic tools and therapeutic agents for treatment of a variety of diseases, mainly cancers, infections, diabetes, (auto-)immune and cardiovascular disorders [2, 3, Tab. 1]. Monoclonal antibodies are hydrophilic and charged molecules presenting a high molecular weight (> 150 kDa) and a high specificity for their target. These properties greatly influence their pharmacokinetics (PK) and limit their distribution into tissues [4–7]. Even with growing knowledge on molecular processes governing mAbs disposition, it is still a challenge to understand and predict their PK, an area which can gain insights from modeling and simulation.

Important biological considerations for mAbs disposition

Structure of mAbs   Antibodies, also known as immunoglobulins (Igs), are large endogenous Y-shaped proteins that play a key role in the humoral immunity by identifying and neutralizing foreign agents such as bacteria and viruses. They have two functional domains: the fragment of antigen binding (Fab) responsible for specific recognition and binding to the antigen and the fragment crystallizable (Fc) region that interacts with Fc receptors present at the surface of effector cells and endothelial cells [8–10]. Figure 1.1 (upper half) provides a representation of the structure of an Ig. In human, there are five isotypes of Igs, i.e. alpha (IgA), delta (IgD), epsilon (IgE), gamma (IgG) and mu (IgM) with different molecular weights, biophysical properties, antigen-binding sites and immunological functions. The most prevalent isotype is IgG and represents 70-80% of total Ig level in serum [11]. IgGs possess a long half-life of ~ 20 days for IgG1, IgG2, IgG4 subtypes and ~ 7 days for IgG3 subtype [4].

Monoclonal antibodies are immunoglobulins (mostly IgG1) produced by a single type of immune cells that are all clones from a parent cell. Therefore, they are identical and monospecific Igs which production is reproducible and allow their use as therapeutics.

Pharmacokinetic properties of mAbs   Pharmacokinetics refers to a branch of pharmacology aiming at studying the fate of administered drugs in body fluids (e.g.
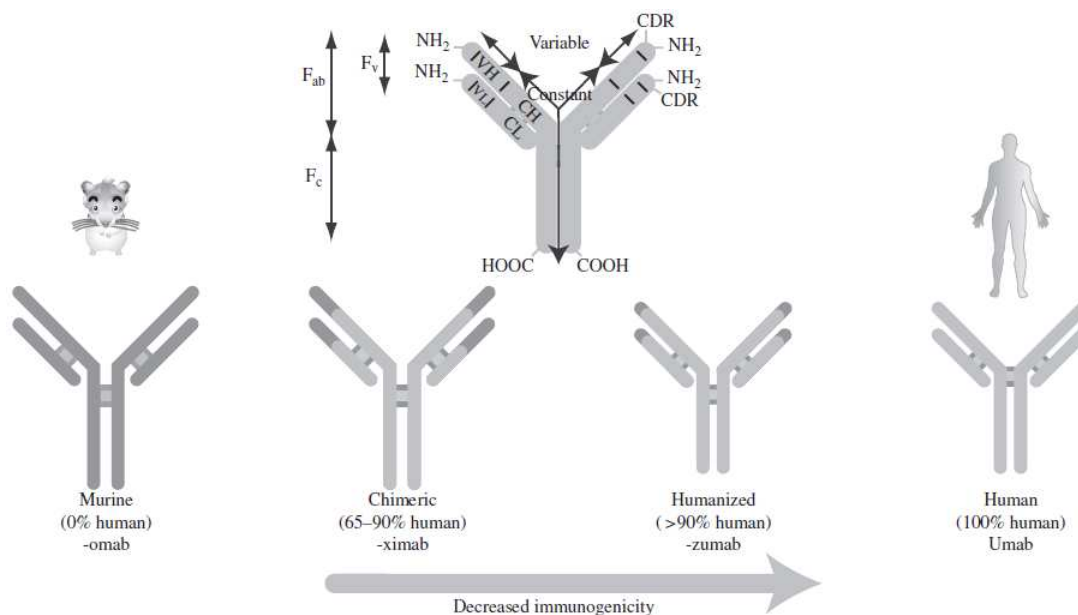
Figure 1.1: *Typical mAb structure and four types of IgGs used as therapeutics (from [12]).*

blood, plasma, interstitial fluid) and in tissues/organs [13]. In this section, we present the principal properties of mAbs which impact their pharmacokinetics.

Monoclonal antibodies are charged therapeutic proteins of high molecular mass ($\sim$ 150 kDa). These aspects are reflected in specific ADME properties. Convective transport, transcytosis, target-mediated disposition, pinocytosis, lysosomal degradation are key mechanisms governing the disposition of mAbs.

As proteins, mAbs are catabolized by proteases, present at high concentration in the gastro-intestinal (GI) tract. Along with their charge and size, GI proteolysis prevents from oral administration. Therefore, intravenous (IV), subcutaneous (SC) or intramuscular (IM) injections are favored routes of administration for mAbs.

Studies of uptake into the systemic circulation following SC administration highlighted the importance of the lymphatic system in the distribution of mAbs [5, 14, 15]. After SC administration, mAbs are present in the interstitial fluid of the skin from which they are drained via the lymph through lymphatic vessels to the bloodstream. Of note, due to a lack of a pumping system, the lymph flow is 100-500 times slower than the blood flows [16]. From the bloodstream, mAbs distribute to the tissues by extravasation from the vascular space to the interstitium across the endothelium. According to the two-pore formalism [6], fluids and large molecules are transported across the endothelium through large pores ($\sim$ 250 Å) while small molecules are 'filtrated' through small pores ($\sim$ 45 Å). The difference of hydrostatic pressure between the two spaces creates a convective transport, characteristic to mAbs tissue-distribution, which results in their extravasation through the large pores into the interstitial fluid

FcRn-mediated transcytosis also plays an important role in the extravasation of mAbs in the interstitium. The relevance of the neonatal Fc receptor (FcRn) stems from the fact that it protects IgGs from catabolism [17] and is responsible of the homeostasis of endogenous IgG and the observed long half-life of IgG1 mAbs in plasma. IgGs bind to FcRn, via their Fc part, in a pH-dependent manner with a high and strong affinity at acidic pH (< 6.5). It was previously reported in [18] that FcRn protein is expressed by a wide variety of tissues e.g., renal proximal tubules, endothelial cells of most organs vasculature, keratinocytes, hepatocytes, mammary epithelium, monocytes, intestinal macrophages, dendritic cells, aortic endothelial cells, and spleen. FcRn resides in the endosomal vesicles within those cells. Following pinocytosis, endogenous IgG and mAb bind to FcRn in acidic sorting endosomes. IgG-FcRn complexes are bidirectionally transported to the cell surface and once outside the cell, at physiological pH, the IgGs dissociate from FcRn and are released in the extra-cellular space. The FcRn-mediated salvage mechanism contributes to the delivery of IgGs to plasma and interstitium and protects from the non-specific elimination by lysosomal degradation in the tissue. Figure 1.2 proposed in [19] illustrates this mechanism.

Immunoglobulins also bind to cell-surface Fcγ receptors (FcγR), implicated in IgG-induced phagocytosis of microbes and cancer cells [25]. Their role on the pharmacokinetics of IgGs is not fully understood [10].

High specific binding of mAbs to their pharmacological target (affinities K_D are commonly in the range of the pM to nM) is responsible of the saturable target-mediated elimination, also known as target-mediated drug disposition (TMDD). It is reflected in the non-linear PK at doses inferior to target saturation [26]. Binding to the target triggers internalization of the mAb-target complex which is thereafter catabolized by lysosomal proteases.

Relevance of modeling & simulation in understanding pharmacological processes of therapeutic drugs

Modeling and simulation methods play an important role in supporting the discovery and the development of new molecule drugs and the optimization of marketed medicines. The fields covered by modeling and simulation activities extend from identification and validation of new targets, selection of lead candidate molecules, description and prediction of pharmacokinetic properties, i.e. absorption, distribution, metabolism, excretion (ADME), efficacy and safety of drug candidates [27–33]. The integration in mathematical models of the knowledge acquired through the development of a drug aids at predicting the human dose, developing new formulations, designing safety and efficacy trials, and guiding regulatory decisions to develop a medicine with the best efficacy/safety profile [13, 34] for a given population. Most
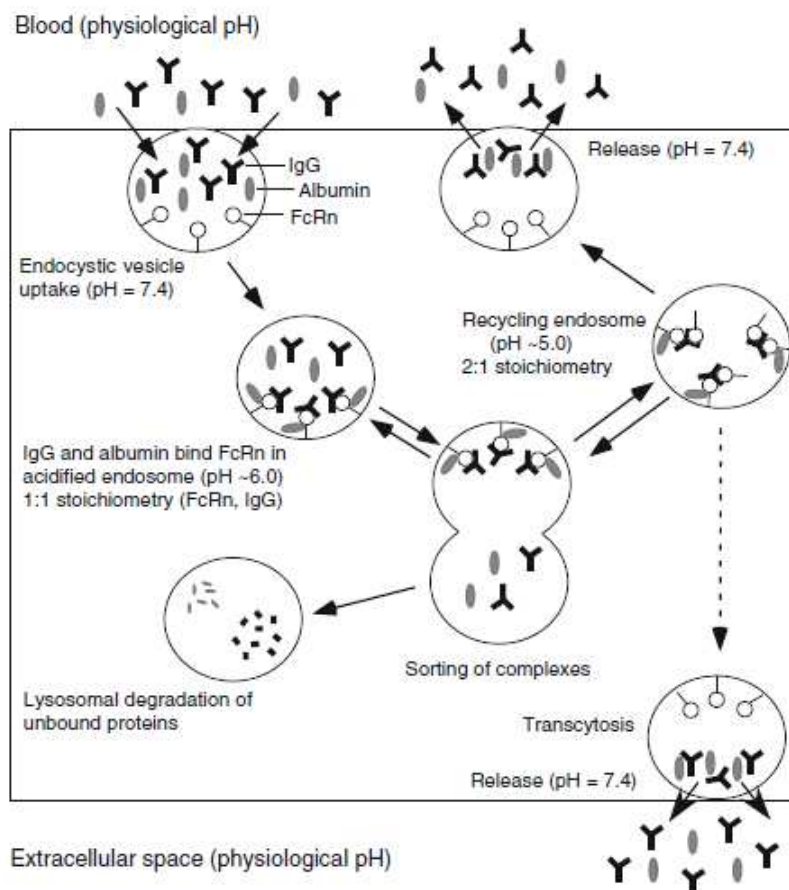
Figure 1.2: *Proposed FcRn-mediated salvage mechanism that occurs in the endothelial cells (from [19]). In short, circulating molecules of IgGs (endogenous IgGs and therapeutic mAbs) in the vascular space are taken up by endothelial cells via spontaneous pinocytosis (also referred to as a fluid phase endocytosis). The pH decreases in newly formed endosomes from physiological pH = 7.4 to acidic pH = 6.0. At acidic pH, IgGs bind with high affinity to FcRn [20], in the range of nM [21–24]. Sorting of the endosomes directs remaining unbound species towards lysosomal degradation while FcRn-bound species are recycled to plasma or delivered to the interstitial fluid space via transcytosis when the binding of IgG-FcRn is cleaved at the contact of physiological pH.*

models are developed and used in a build-validate-learn-refine cycle in which the available knowledge is initially captured during model building and compared to actual data to gain confidence during model evaluation and refinement [27, 35–39]. Fig. 1.3 illustrates the various areas supported by modeling and simulation along the value-chain.

Pharmacokinetic modeling is a mathematical means which uses the concentration-time profiles to provide quantitative and dynamic information about the processes that affect the kinetics of a drug, i.e. absorption, distribution, metabolism, excretion (ADME properties), see Fig. 1.4 [13, 34, 43]. All models are a representation
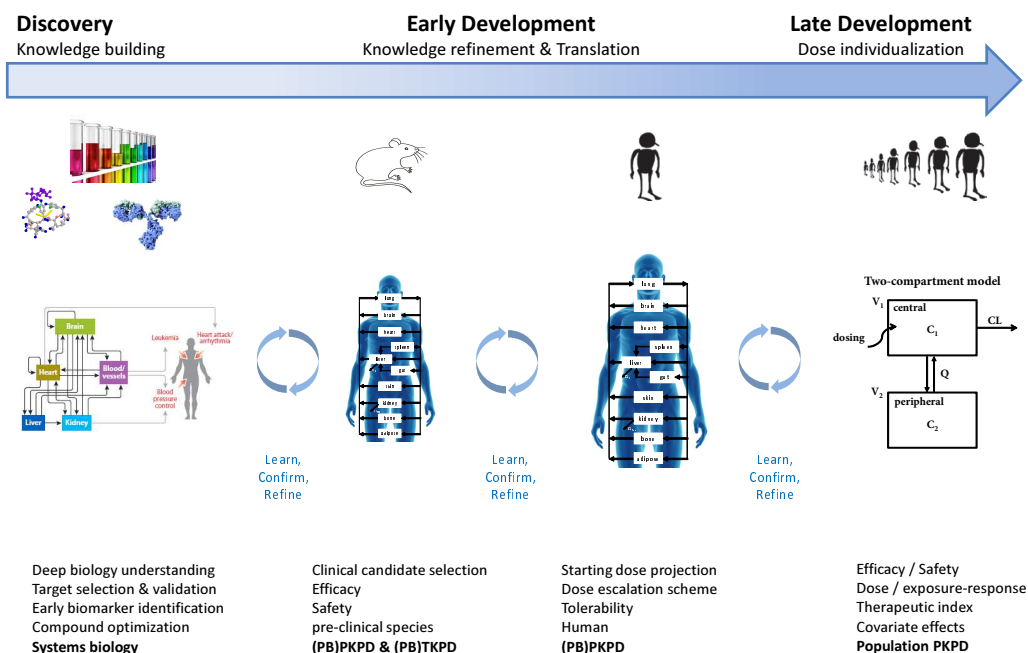
Figure 1.3: *Drug development and modeling & simulation: Build-validate-learn-refine paradigm along the value-chain (inspired from [30, 40–42]).*

of the body which is discretized into spaces referred to as compartments. The simplicity/complexity of the models varies as per their data-driven or mechanistic nature.

The non-compartmental approach allows to derive descriptive PK parameters from the experimental data, i.e. area under the curve (AUC), peak exposure (Cmax), time at which occurs Cmax (Tmax) [44, 45]. Non-compartmental analysis (NCA) provides an initial descriptive analysis to assess dose proportionality, characterize general drug disposition and determine the degree of exposure following the administration of a drug.

Classical compartmental modeling is a data-driven approach. The body is represented by a system of compartments, typically one to three, where the drug is assumed to distribute instantaneously and homogeneously. The structure and parameterization of the empirical models are directly dictated by the experimental data and derived by non-linear fitting means [38]. The choices of the structure of such models is based on the goodness-of-fit to the experimental data [38]. Fig. 1.5 gives a representation of the most commonly used empirical compartmental models governed by first-order distribution processes. The empirical character of these models prevents from extrapolation beyond the range of doses, dose routes, species and population used to build them. As for NCA, this approach is rather employed for exploratory data-analysis.
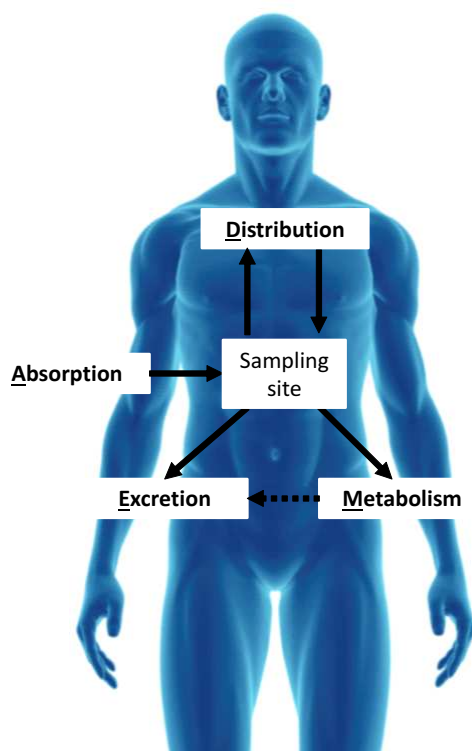
Figure 1.4: *ADME processes influencing the pharmacokinetics of drugs: Absorption, Distribution, Metabolism, Excretion.*

Mechanistic PK models consider the system under study with more physiological meaning and take into consideration some physical and chemical properties of the drug. Three types of mechanistic modeling approaches are mainly used and applied to kinetic modeling: systems biology, systems pharmacology and physiologically-based pharmacokinetic (PBPK) modeling [46–48]. While the two first are still emerging disciplines in drug discovery and development, PBPK models have been more widely applied to characterize and predict the biodistribution of small molecule drugs (SMDs) [39, 48–53].

PBPK models offer a unique framework to use actual knowledge and new understandings of the physiological, anatomical and biophysical aspects of the system and of the biochemical properties of the drug, generated from various *in vitro* and *in vivo* experiments at all stages of the pre-clinical and clinical development [39, 50, 51]. Whole-body PBPK models aim at analyzing, understanding, interpreting and predicting the PK of drugs from cellular level, tissues, organs to the whole organism level. They consist of multiple compartments that represent the most relevant anatomical spaces of the body connected by arterial and venous blood flows, as depicted in Fig. 1.6. The level of granularity of these anatomical spaces depends on the ADME properties and the mechanism of action of the drug and extends from molecular reactions at the cellular level to the overall organ or tissue. Commonly, PBPK models,

One-compartment model

$$V_d \frac{d}{dt} C_1 \;=\; -CL \cdot C_1 + r_{\text{admin}}$$

Two-compartment model

$$
\begin{aligned}
V_1 \frac{d}{dt} C_1 &= Q \cdot (C_2 - C_1)\\
&\quad -CL \cdot C_1 + r_{\text{admin}}\\
V_2 \frac{d}{dt} C_2 &= Q \cdot (C_1 - C_2)
\end{aligned}
$$
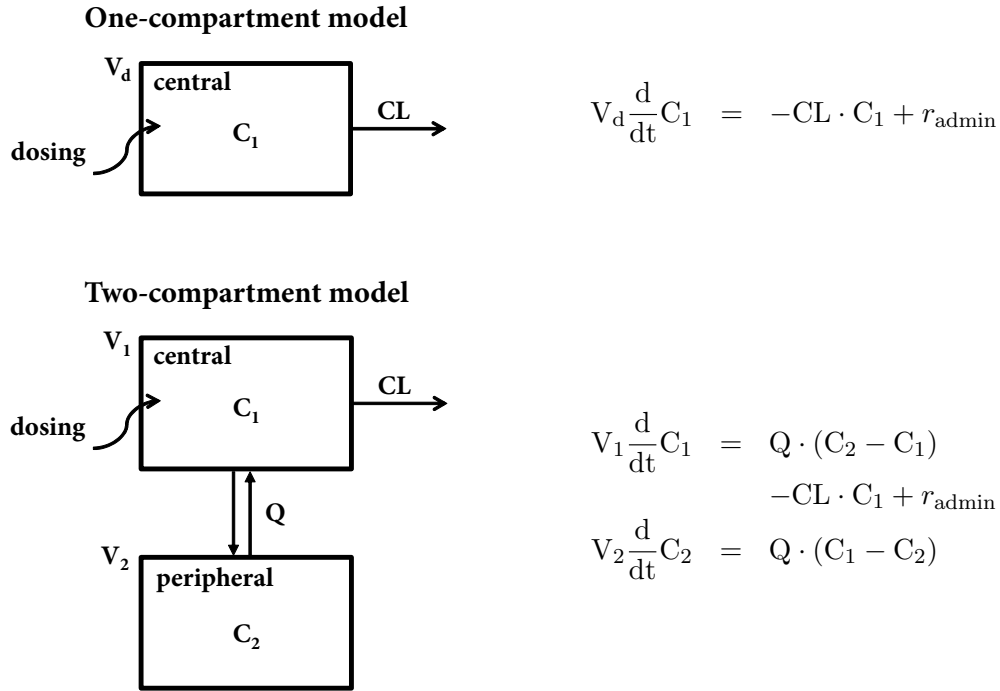
$$
\begin{aligned}
\text{with } C_1(t=0) &= \frac{\text{dose}}{V_d} \text{ for i.v. bolus administration,}\\
C_1(t=0) &= 0, \text{otherwise.,}\\
r_{\text{admin}} &= r_{\text{iv,bolus}} = 0,\\
r_{\text{admin}} &= r_{\text{iv,infusion}} =
\begin{cases}
\text{dose}/\Delta T; & t \in [T0, T0 + \Delta T],\\
0; & \text{otherwise.}
\end{cases}\\
r_{\text{admin}} &= r_{\text{abs}} = \text{dose} \cdot F \cdot ka \cdot e^{-ka \cdot t}.
\end{aligned}
$$

Figure 1.5: *Most frequently used empirical compartmental models to describe drug disposition. In both models, the concentration in the central compartment, C_1, represents for the concentration at the site of measurement (plasma, blood, etc.). All kinetic processes are rate-limited of first-order. The inter-compartmental clearance, Q, accounts for inflow and outflow. The elimination occurs from the central compartment with a clearance CL. The volumes of the compartments, V_d, V_1 and V_2, are apparent volumes. r_{admin} represents the mass inflow per unit time: for an i.v. bolus, it is $r_{iv,bolus}$; for an infusion of duration ΔT, starting at $T0$, it is $r_{iv,infusion}$; for oral, intramuscular or subcutaneous administration, r_{abs}, with ka, the absorption first-order rate constant and F, the bioavailabilty.*
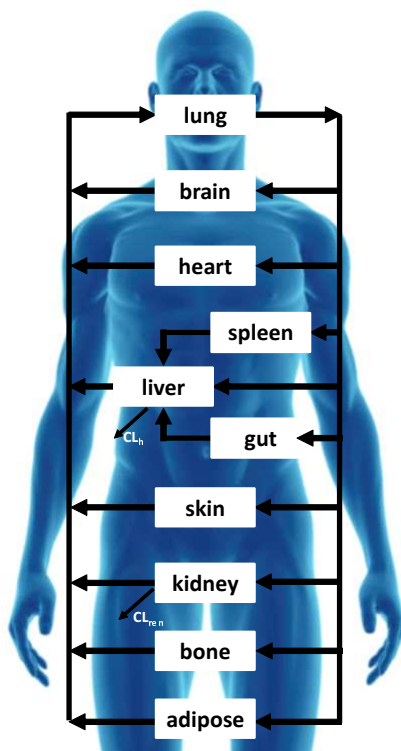
Figure 1.6: *Topology of a theoretical 10-compartment whole-body PBPK model with hepatic CL_h and renal CL_{ren} elimination.*

first develop and used for SMDs, include parameters that are drug-dependent, e.g. lipophilicity, protein binding, ionization, permeability, receptor affinity, hepatocyte and microsomal clearances and species-dependent, e.g. cardiac output, blood, plasma and lymph flows, tissue composition, organ volumes, etc. [41, 49, 53]. The mechanistic nature of PBPK models allows for (i) integration of *in vitro*, and *in vivo* data, (ii) mechanistic understanding of underlying processes, (iii) prediction of the pharmacokinetics of different drugs before any *in vivo* testing, (iv) extrapolation to different species and populations, (v) analysis of drug-drug interaction and (vi) analysis of the impact of inter-individual variability on the PK [54]. Beyond the complexity of PBPK models along with availability and accuracy of their parameterization that can represent an obstacle to their use to support drug development, they represent the most advanced modeling approach to mechanistically describe the disposition of therapeutics at the cellular and/or organ and/or whole body levels. The real advantages of PBPK modeling are its integrative and translational features which are a real asset to optimize the transition from pre-clinical to clinical development.

NCA, empirical compartmental modeling and PBPK modeling approaches are used during drug development to better understand, describe and predict the concentration-time profiles of monoclonal antibodies. In the sequel, we highlight each of the method-

ology and set the grounds for the need of a PBPK model for mAbs consistent with available experimental data.

Pharmacokinetic modeling of monoclonal antibodies disposition

Descriptive classical approaches   The underlying assumptions of NCA, i.e. linear drug disposition, mono-exponential decline of the concentrations at the terminal phase, elimination from the sampling pool, PK parameters constant over time [45], may not be valid for monoclonal antibodies. Several authors [2, 3, 19, 55], whom Dirks and Keizer, report a low Vss for mAbs in human close to the plasma volume (i.e. 5L [56]), at therapeutic dose levels. Specific properties of mAbs, i.e. extravasation into the tissue via convective transport & transcytosis, saturable binding to their target and intra-cellular internalization suggest otherwise [19]. In [18], Shah and Betts report tissue-to-plasma partition coefficients (also named antibody biodistribution coefficients ABCs). ABCs are directly derived from experimental plasma and tissue concentrations of several mAbs and range from 3.97 % for muscle to 67.5 % for thyroid suggesting clear tissue distribution (even if limited) which is not reflected in NCA.

Empirical modeling is typically applied in the context of population pharmacokinetic analysis of clinical data [37, 57]. In their respective reviews of population analysis of clinical mAbs data, Dirks and Keizer report that a two-compartment model most commonly describes the disposition of mAbs, showing that different mAbs present similar PK despite their different target and disease population of analysis. While the clearance is mainly characterized by a linear process from the central compartment, some models include a non-linear clearance or parallel linear and non-linear clearances [2]. The non-linear clearance reflects the elimination of mAbs via target-mediated mechanisms (at doses below the saturation threshold of the target) and is usually described by the Michaelis-Menten equation [58, 59]. Due to its empirical nature, mechanistic interpretation of the parameters in the Michaelis-Menten equation (Km, the Michaelis-Menten constant representing the concentration of mAb at which the elimination is at half maximum and Vmax, the maximum elimination rate) and extrapolation to different species are limited.

Semi-mechanistic models have been developed to accommodate the specificities of mAbs PK. They remain empirical in their structure but integrate aspects of mechanistic processes. In [60], the two-compartment model describes the PK of the mAb, 7E3, in mice non expressing the target. The peripheral compartment refers to the endosomal space where the saturable binding to FcRn occurs. Unbound species are cleared from the endosomal space following a linear process and FcRn-bound mAbs flow back into the central compartment. The explicit consideration of FcRn binding allows to derive FcRn saturation level. The model predicts that FcRn is

saturated at baseline level, i.e. by steady-state of endogenous IgG. Incorporating FcRn-binding into PK models for mAbs is highly valuable specially to investigate the PK of mAbs with engineered Fc-region, with increased/decreased affinity to FcRn [61–63]. However, the lack of *in vitro* data on FcRn binding capacity, trafficking rates of endosomes and *in vivo* endosomal concentration of mAbs does not support the underlying model assumption made by Hansen [60] that the volume of distribution in the endosomal space is equal to the volume of the central compartment [64]. It also does not allow to reliably estimate the parameters associated with the peripheral compartment and link them to physiological meaning. In [64], Xiao proposes a 2-compartment model which also accounts for the non-linear binding to FcRn in the peripheral compartment, where the resulting fraction unbound of total IgG is derived from a cutoff value 'MAX' (that is identical to total FcRn concentration, fitted to plasma data) and from total IgG concentration which presents the typical biphasic behavior. Unless the model from Hansen [60], the cutoff model from Xiao predicts a constant non-specific linear clearance for endogenous IgG baseline levels with low saturation level of FcRn. The contradictory status of the two models on the saturation level of FcRn at baseline brings out the difficulty of describing the interaction of IgG with FcRn without supporting experimental data. The cutoff model also differs from the previous in the definition of the peripheral compartment which is a lumped form of the endosomal space with any other space accounting for peripheral distribution. It, however, still remains empirical in the sense that the estimated parameters, including the total concentration of FcRn, are apparent parameters. Therefore, they do not inform on the *'real'* physiological biodistribution of mAbs which complicates the extrapolation to other species. Lammerts van Bueren et al. [6] developed a 3-compartment pharmacokinetic model, in cynomolgus monkeys, which accounts for distribution of zalutumumab, targeting EGFR, in plasma and interstitial pools. The distribution kinetics is described by first-order processes while the interaction with EGFR is modeled in terms of Michaelis-Menten parameters, Bmax and Km, accounting for the non-linear interaction of the mAb with the receptor system and known as receptor mediated endocytosis (RME). The model accurately describes experimental plasma data for high and low doses. However, as pointed out in [65], the parameters Bmax and KM are specific to zalutumumab administered to cynomolgus monkeys. An analysis of the impact of changes in the drug-receptor interaction is not feasible with this model which limits its use and interpretation in other species.

Predictive PBPK approaches for mAbs   Over the 20 year-experience of development of mAbs as therapeutic agents, knowledge of physiological and pharmacological processes involved in their biodistribution has considerably expanded (for details, see above paragraph *Pharmacokinetic properties of mAbs*) and are integrated in PBPK

models for mAbs [66–74]. We review the different PBPK models for mAbs presently reported in the literature. The term PBPK model refers to whole-body PBPK model.

The first PBPK model for mAbs was developed in 1986 by Covell and co-workers for a mAb, non cross-reactive with the mouse [66]. The PBPK model accounts for (i) distribution to the organs via plasma flows; (ii) trafficking across the capillary wall described with a single pore model (simplified version of the two-pore model published by Rippe and Haraldsson [6]); (iii) return from the interstitial space to the bloodstream via the lymph; (iv) unspecific distribution and elimination in a 'cell-associated' space described by first order processes. The model includes six organs/tissues (liver, gut, lung, spleen, kidney and carcass) and plasma. Each tissue is divided into 3 sub-compartments accounting for vascular, interstitial and cellular spaces. While some parameters are estimated for each tissue by fitting to plasma and tissue data, i.e. the permeability surface area product PS of the pore model, the apparent volume of distribution in the cellular space V_c and the cellular space associated first order elimination k_{elim} with no guarantee of identifiability, others were arbitrarily fixed, i.e. the exchange rate between interstitial and cellular spaces R to 0.02/min, the value of the reflection coefficient σ to 0.95 for all organs and the lymph flows for visceral and non-visceral organs to 2 and 4 % of plasma flows, respectively. It is important to mention that these parameter values still serve as references for development of subsequent PBPK models development.

Later, Baxter and co-workers presented an extension of the previous PBPK model introducing an additional tumor compartment to describe the PK of mAbs in xenograft mice also expressing the target in bone [67]. The organ model is simplified to two sub-compartments, i.e. vascular space and interstitial space. The transcapillary exchange is described by both convective and diffusive transports according to the two-pore formalism [6] (where large molecules are 'filtrated' through large pores of $\sim$ 250 Åwhile small molecules are 'filtrated' through small pores of $\sim$ 45 Å. Tissue parameters including large-pore volume flows ($J_{L,iso}$, eq. 18-32 in [6]), lymph flows and target-binding association rate constants are fitted to plasma and tissue concentrations. Tissue plasma flows and total tissue volumes, reported in Table 1 in [67], origin from literature [75] which validity is questioned in a following commentary [76] and from experimental data. They are still used as reference values in PBPK models for mice.

The first PBPK model to incorporate FcRn-IgG interaction was developed by Ferl and co-workers to describe the biodistribution of an anti-CEA mAb in mice previously injected with human colorectal cancer cells [68]. The model includes 11 compartments with 9 tissues/organs (heart, kidney, GI tract, spleen, lungs, bone, muscle, skin and liver), a plasma compartment for vein and artery plasma and a tumor compartment. In comparison to Baxter's model, (i) most of organ compartments are divided into 2 sub-compartments, i.e. vascular space and interstitial space, except for muscle and skin accounting for the endosomal space and for the tumor accounting for the

tumor tissue space; (ii) a first-order elimination occurs from the liver where significant degradation of proteins takes place as suggested in [77]; (iii) the saturable binding to FcRn occurs solely in the endosomal space of muscle and skin based on experimental data suggesting that FcRn is mainly expressed in those two tissues [78, Fig. 2(left)]. As it remains unknown, the unbound FcRn concentration, along with elimination rate constants, was estimated with the experimental data. One can question the physiological value of FcRn concentration and how to scale it to other species.

In a subsequent attempt to gain quantitative insights on FcRn-mediated salvage mechanism, Garg and Balthasar published a FcRn-based PBPK model for endogenous IgG and non-antigen specific mAbs [69]. The model allows to replicate plasma and tissue concentration-time profiles of the mAb, 7E3, in wild-type and FcRn-knockout mice. Each organ/tissue (except for plasma) is sub-divided into 3 compartments, i.e. vascular, interstitial spaces and an endosomal compartment where endogenous IgG and therapeutic mAb compete for binding to FcRn. Tissue distribution is described by fluid-phase endocytosis (also named pinocytosis) [79–81] and convective transport from the vascular space in the interstitium and back to the central circulation via the lymphatic system. Pinocytosis into endosomes and transcytosis to the cell surface is represented by first-order rate constants. The convective transport through the vasculature is described with a single pore model. While most of physiological parameter are obtained from previous PBPK models [66, 67] (cited above), others were empirically derived, i.e. endosomal volumes, vascular reflection coefficients, tissue FcRn capacities, tissue intrinsic clearances from various references [60, 66, 81, 82] and others were fitted to plasma data solely, i.e. first-order rate constants in relation to trafficking in the endosomes.

The PBPK model proposed par Davda and colleagues offers an alternative tissue model composed of a vascular and an interstitial space. The model accounts for a tumor compartment to describe the biodistribution data of mAb CC49, an anti-antigen TAG-72, expressed by mucinous adenocarcinomas and cross-reactive in xenograft mice. The linear component of the clearance is described by a catabolic clearance solely occurring in the endosomal space of carcass and liver where FcRn-binding is not explicitly considered [70]. The two-pore model from Rippe and Haraldsson [6] is used to describe the transport of mAbs across the capillary wall. Unknown parameters related to the two-pore model, linear clearance, and lymph flows were iteratively fitted to biodistribution data. The model is sensitive to changes in most of the fitted parameters, i.e. tumor volume, fluid recirculation rate, lymph flow rate, small pore vascular permeability, and partition coefficients. Identifiability of parameters in PBPK models are frequently encountered problems when they are over-parameterized compared to the data available.

Following published PBPK models based on the work from Garg and Balthasar [69], increase the level of details of the tissue model.

Urva and co-workers [71] introduced a lymph node compartment playing the role of transit compartment which physiological volume is arbitrarily fixed to the volume of spleen. Missing parameters related to the endosomal space and lymph node were fitted to plasma data solely.

Chen and Balthasar [72] represent the endosomal space with a catenary model allowing representation of the time-dependent acidification during endosomal trafficking (from pH=7.4 at the initiation of pinocytosis to pH=6 in the late endosome). The number of transit compartments is set to 4 in which FcRn binding is not considered at equilibrium. The catenary PBPK model differs from previous models as it (i) incorporates tissue-specific FcRn expression based on *unpublished* FcRn-mRNA data; (ii) modulates the bioavailabilty from the lymph; (iii) considers uptake rates in the tissue that are derived from published pinocytosis rates for mono-layers endothelial cells [83–85]; (iv) does not consider FcRn-binding at equilibrium but accounts for association, kon, and dissociation, koff, rate constants at different pH. The catenary model allows to address the impact of FcRn-binding affinity variations which is valuable for better understanding of the impact on the biodistribution of mAbs with Fc-engineered variants. Interestingly, it predicts 1.5-fold increase in plasma half-life while equilibrium models predict up to 7-fold increase, for a 100-fold increase in FcRn affinity. The missing parameters, i.e. constant endogenous IgG production rate, coefficients accounting for non-FcRn-dependent tissue uptake (therapeutic mAb-specific) and the transit time in the lymph node compartment, are fitted to plasma data solely and the authors report that different sets of those parameters could be estimated which is typically related to a problem of identifiability for over-parameterized models.

Shah and Betts [73] present a platform PBPK model which intends to characterize the biodistribution of mAbs in mice, rats, monkeys and human, given a set of only four unknown parameters, i.e. FcRn concentration, the rate of pinocytosis, CL_{up}, the endosomal degradation rate constant, k_{deg} and the scaling factor to derive the lymph flow of lymph node from plasma flow, C_{LNLF}. Values of vascular and lymphatic reflection coefficients, σ_{vas} and σ_{lymph} respectively, were set based on literature review of physiologic upper limits of pore size of blood capillaries [86]. The underlying assumptions for this platform PBPK model are that: These parameters are conserved between different species and that binding to FcRn is described by kon and koff rates and is not impacted by endogenous IgG that is not considered in this model. While the model provides reasonable predictions of plasma and tissue concentration-time profiles of several mAbs, the authors report that the model is *highly* sensitive to k_{deg}, k_{off} and *notably* sensitive to FcRn, k_{on}, σ_{vas} and CL_{up} which might be linked to the above-mentioned assumptions.

Cao, Bathasar and Jusko [74] provide an alternative minimalistic PBPK model which aims at describing general attributes of the biodistribution of mAbs, i.e (i) overall plasma kinetics; (ii) extra-vascular distribution represented by two interstitial spaces accounting for two groups of tissues classified as *leaky* and *tight*; (iii) non-specific clearance from plasma and/or from interstitial compartments. The structure of the model is based on general considerations and does not allow to describe experimental concentration-time profiles in the tissues.

Reduction of PBPK model dimensionality has been previously mathematically derived for SMDs [87–91]. Such derivation still need to be applied to full PBPK model for mAbs in order to derive minimal PBPK models fully consistent with the underlying complex mechanisms involved in mAbs biodistribution.

From their intrinsic mechanistic nature, there is a lot of interest in developing PBPK models for mAbs to answer an array of questions related to the disposition and efficacy of therapeutic mAbs. Mechanistically, most of the recent models take into account the uptake of the mAb into the endosomal space by fluid phase endocytosis and also the recycling/protection of catabolism of IgGs by FcRn within the endosomal space, under some, more or less legitimate, assumptions. Multiplicity of assumptions and potential error prorogation may lead to liabilities to model misspecification and result in misinterpretation. More work is needed to reduce to its minimum the number of assumptions made in whole-body PBPK models for mAbs.

Objectives

Despite growing understanding of molecular processes involved in mAbs disposition [3, 55], there is still no clear consensus on the structure and parameterization of physiologically-based pharmacokinetic models [41] nor on the interpretation of classical compartment models [64].

Published PBPK models for mAbs are quite heterogeneous with respect to their representation of the physiology and the parameterization of the mechanisms involved in mAbs disposition [66–74], e.g., regarding (i) the definition of the relevant tissue spaces (vascular and interstitial tissue spaces or additionally an endosomal compartment); (ii) how to model extravasation (by diffusive and convective transport or only by convective transport); (iii) the relevance of FcRn (whether to explicitly account for the interaction with FcRn and whether to use an equilibrium model or a detailed binding kinetics, whether to account for pH-dependent binding); (iv) the importance to explicitly account for the endogenous IgGs; (v) the relevance to include a lymph node compartment; or (vi) how to describe the clearance of mAbs.

A clearer understanding of the physiological processes to be explicitly considered and the necessary assumptions to make within PBPK models for mAbs are required to increase their use in drug development, to better understand the mechanisms governing the disposition of monoclonal antibodies from the cellular level to the whole-body level and to translate the knowledge accumulated in discovery and early development into relevant animal species and ultimately in human.

The PK of mAbs is commonly described by a classical 2-compartment disposition model [3], with central and peripheral compartments typically associated with plasma and interstitial space, respectively. Description of mAb elimination processes in empirical models is quite diverse (i.e. either linear [92] or non-linear [93, 94] or parallel linear and non-linear clearances [95, 96]). Non-linearity in the PK is mainly attributed to the saturable binding to the target [65, 97–101]. Much less is known about the physiological mechanisms involved in the linear elimination. Monoclonal antibodies similar to IgGs present common structural properties and molecular mechanisms, independent of target-binding. Elimination in lysosomes and protection from elimination by binding to FcRn is known to be a major process influencing the PK of mAbs. However, it is not obvious, how to link the non-linear FcRn-mediated protection from elimination in the endosomes to commonly used linear clearance terms

in classical compartment models. The derivation of low-dimensional compartment and covariate models consistent with PBPK models for mAbs would greatly benefit the mechanistic interpretation of classical compartment models typically developed in the the population context during late stage drug development.

The focus of the thesis is to derive mechanistic modeling approaches to support the development of monoclonal antibodies. The thesis is formulated around three thematics:

- the development of a whole-body PBPK model, consistent with the current knowledge of processes governing the disposition of mAbs;

- the extension of the lumping approach previously published for SMDs [91] to mAbs to carry the mechanistic knowledge into classical compartment models;

- the analysis of the predictable impact of variations in *anatomical* and *physiological* parameters of PBPK models typically used as covariates for PK parameters derived from classical compartment models.

We first develop whole-body PBPK models and highlight the need of model simplification to allow for stable parameter estimation, given currently available plasma and tissue data. A *detailed* PBPK model accounts for FcRn binding and endogenous IgG while an *intermediate* PBPK model implicitly considers binding to FcRn.

Based on time scale considerations, we propose a *simplified* PBPK model for mAbs while retaining the mechanistic knowledge embedded in the current experimental data. We also illustrate that the simplified PBPK model can easily be extended to account for a target and therefore describe the non-linear clearance due to mAb-target interaction.

We define the link between empirical PK and PBPK models for mAbs to carry the mechanistic knowledge into low-dimensional compartment models allowing for mechanistic interpretation of the PK parameters of classical compartmental models.

We finally make use of the mechanistic knowledge present in whole-body PBPK models in order to analyze the influence of variability of anatomical and physiological parameters on covariate models typically used in the context of population pharmacokinetic analysis.

Full PBPK Models for mAbs

To better understand the physiological processes to be explicitly considered and the necessary assumptions to make within PBPK models for mAbs, we describe, in this chapter, full PBPK models which integrate detailed tissue models to characterize the disposition of endogenous IgG *and* therapeutic mAb similar to IgG1. We further study the importance and the impact of the model parameterization to explicitly account for FcRn-IgG interaction.

3.1 *Detailed* PBPK model

The whole-body detailed PBPK model intending to describe the disposition of endogenous IgG *and* mAb in mice is based on the extension of the PBPK model published by Garg in [69]. The PBPK model (Fig. 3.1(left)) comprises 32 compartments representing the most relevant anatomical spaces involved in the disposition of IgGs: venous and arterial plasma as well as plasma, endosomal and interstitial spaces of lung, adipose, bone, heart, kidney, muscle, skin, gut, spleen and liver. Furthermore, the presence of endogenous IgG in addition to the therapeutic mAb is considered.

3.1.1 Modeling endogenous IgG and mAb disposition

The tissue model comprises the vascular, endosomal and interstitial sub-compartments with the corresponding volumes V_p, V_e and V_i. The following processes relevant for endogenous *and* therapeutic antibodies distribution and elimination are considered: (i) body distribution via the plasma flow; (ii) transport into the interstitial space of tissues via convective transport through the para-cellular pores in the vascular endothelium (simplified two-pore model, i.e. one-pore formalism); (iii) convective transport via the lymph from the interstitial space in the plasma circulation; (iv) uptake from the plasma and interstitial spaces into the endosomal compartment via fluid phase endocytosis; (v) saturable binding to FcRn in the endosome, (vi) salvage of FcRn-bound complexes to the plasma and interstitial spaces; (vii) lysosomal degradation of the unbound species in the endothelium. A detailed overview of all considered processes and the corresponding parameters can be found in Fig. 3.1(right).
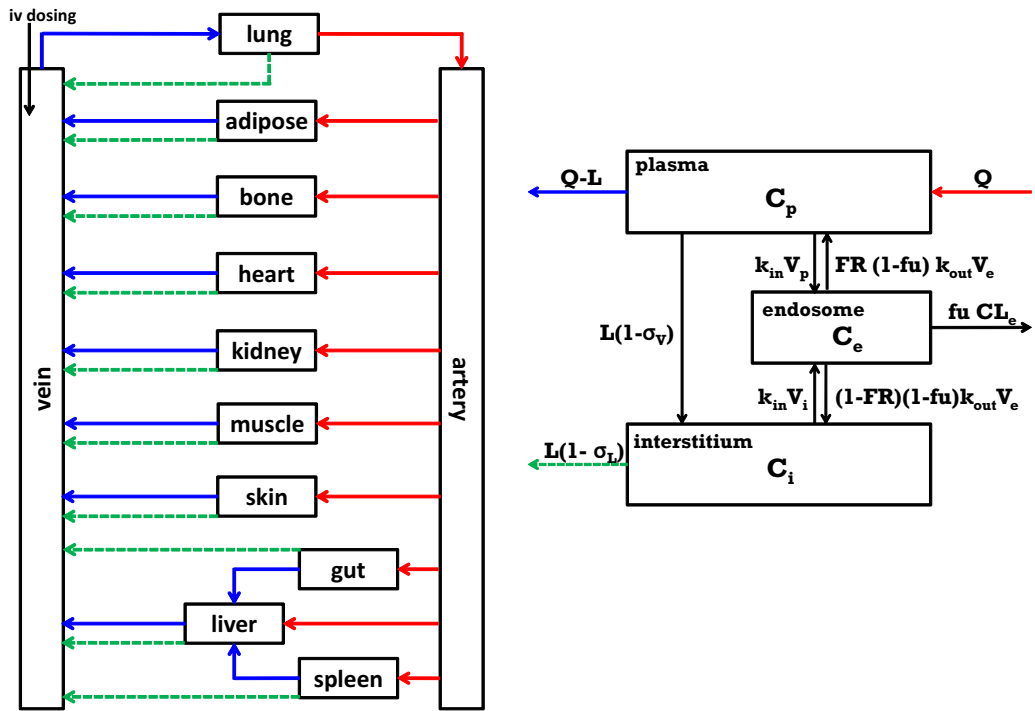
Figure 3.1: *Topology of the detailed PBPK model for mAbs. Left: Structure of the detailed PBPK model for mAbs. Organs, tissues and plasma spaces are interconnected by the plasma flows (red and blue solid arrows) and the lymphatic system (green dashed arrows). Right: Detailed organ model comprising a plasma compartment, the endosomal and interstitial spaces.* Q *and* L *represent plasma and lymph flows,* σ_{vas} *and* σ_{lymph} *denote the vascular and lymphatic reflection coefficients,* k_{in} *is the rate constant of uptake of IgGs from the plasma or interstitial space into the endosomal space.* k_{out} *is the recycling rate constant of IgGs from the endosomal space (with a fraction* FR *recycled into the vascular space), while* $fu \cdot CL_e$ *denotes the linear clearance from the endosomal space.*

Based on previously developed whole-body detailed PBPK models for mAbs [67, 69, 70], the rates of change of endogenous IgG *and* mAb concentrations are given by the following system of ordinary differential equations with C = IgG or C = mAb (the abbreviations of names for organs/tissues are given in Table 3.2):

$$
\begin{aligned}
V_{ven}\frac{d}{dt}C_{ven} = \ & + q_{prod} \\
& + Q_{ven} \cdot (C_{in,ven} - C_{ven}) + \sum_{tis} L_{tis} \cdot (1 - \sigma_{lymph}) \cdot C_{i,tis} \quad (3.1)
\end{aligned}
$$

$$
tis = lun, adi, bon, gut, hea, kid, liv, mus, ski, spl
$$

$$
V_{art}\frac{d}{dt}C_{art} = (Q_{lun} - L_{lun}) \cdot C_{p,lun} - Q_{art} \cdot C_{art} \quad (3.2)
$$

$$
\begin{aligned}
V_{p,tis}\frac{d}{dt}C_{p,tis} = \ & Q_{tis} \cdot C_{in,tis} - (Q_{tis} - L_{tis}) \cdot C_{p,tis} \\
& - L_{tis} \cdot (1 - \sigma_{vas}) \cdot C_{p,tis} - k_{in} \cdot V_{p,tis} \cdot C_{p,tis} \quad (3.3) \\
& + FR \cdot k_{out} \cdot (1 - fu_{tis}) \cdot V_{e,tis} \cdot C_{e,tis}
\end{aligned}
$$

$$
\begin{aligned}
V_{e,tis}\frac{d}{dt}C_{e,tis} = \ & + k_{in} \cdot V_{p,tis} \cdot C_{p,tis} + k_{in} \cdot V_{i,tis} \cdot C_{i,tis} \\
& - k_{out} \cdot (1 - fu_{tis}) \cdot V_{e,tis} \cdot C_{e,tis} - CL_{e,tis} \cdot fu_{tis} \cdot C_{e,tis} \quad (3.4)
\end{aligned}
$$

$$
\begin{aligned}
V_{i,tis}\frac{d}{dt}C_{i,tis} = \ & + L_{tis} \cdot (1 - \sigma_{vas}) \cdot C_{p,tis} \\
& - L_{tis} \cdot (1 - \sigma_{lymph}) \cdot C_{i,tis} - k_{in} \cdot V_{i,tis} \cdot C_{i,tis} \quad (3.5) \\
& + (1 - FR) \cdot k_{out} \cdot (1 - fu_{tis}) \cdot V_{e,tis} \cdot C_{e,tis}.
\end{aligned}
$$

In the above equations, the subscripted concentrations C_{ven} and C_{art} refer to the total plasma concentration in vein and artery, while C_p, C_e and C_i refer to the total concentration in the tissue vascular, endosomal, and interstitial spaces. The corresponding compartment volumes are V_{ven}, V_{art}, V_p, V_e and V_i. The plasma and lymph flows are denoted by Q and L. The parameters σ_{vas} and σ_{lymph} refer to the vascular and lymphatic reflection coefficients; k_{in} and k_{out} to the endosomal uptake and the recirculation rate constants; FR to the recirculation fraction of FcRn-bound antibody from the endosomal space into the vascular space. The unbound antibody in the endosomal space is subject to elimination following a linear clearance CL_e. The fraction unbound in endosome is denoted by fu and defined as in eq. (3.8). For endogenous IgG, there is an additional constant rate of production q_{prod}, which is set to zero for therapeutic mAbs.

For all tissues except vein, artery, liver and lung, the inflowing concentration C_{in} is given by

$$
C_{in,tis} = C_{art}.
$$

For lung, vein and liver, it is

$$
\begin{aligned}
\mathrm{C_{in,lun}} &= \mathrm{C_{ven}}, \\
\mathrm{C_{in,ven}} &= \frac{1}{Q_{ven}} \sum_{tis} (\mathrm{Q_{tis}} - \mathrm{L_{tis}}) \cdot \mathrm{C_{p,tis}}, \\
&\quad \mathrm{tis = adi, bon, hea, kid, liv, mus, ski} \\
\mathrm{C_{in,liv}} &= \frac{1}{\mathrm{Q_{liv}}} \left(\sum_{tis}(\mathrm{Q_{tis}} - \mathrm{L_{tis}}) \cdot \mathrm{C_{p,tis}} + \left(\mathrm{Q_{liv}} - \sum_{tis}(\mathrm{Q_{tis}} - \mathrm{L_{tis}}) \right) \cdot \mathrm{C_{art}} \right). \\
&\quad \mathrm{tis = spl, gut}
\end{aligned}
$$

The mAb is administered via IV bolus. For the vein, the initial condition of the above system of ODEs is set to

$$
\mathrm{C_{ven}}(0) = \frac{\mathrm{dose}}{\mathrm{V_{ven}}},
$$

while we set $\mathrm{C_{cmt}}(0) = 0$ for all other compartments 'cmt'.

3.1.2 Model parameterization

A description of the parameters entering the detailed PBPK model is given in Table 3.1. Physiological and anatomical data were taken from [67, 69, 75, 102, 103] and are summarized in Table 3.2. Note that in [67, 69], the plasma space of each organ/tissue is simplistically noted 'vascular space'. However, in the original work [67, p. 1518, 4th paragraph], the cited values are reported as 'vascular (plasma) space'. Hence, the plasma space in the present PBPK model is equivalent to the values of the 'vascular space' in [67, 69].

Unless PBPK models for small molecule drugs, PBPK models for monoclonal antibodies are parameterized with parameters which values remain unknown due to the lack of experimental data, e.g. in-vitro, in-vivo or imaging data. In the detailed PBPK model for mAbs, these parameters are the total FcRn capacity $\mathrm{FcRn_{tot}}$, the rate constant of uptake into the endosomal compartment k_{in}, the outflow rate constant from the endosomal compartment k_{out}, the endosomal degradation rate constant k_{deg}, the fraction of recirculated bound antibody FR, and the zero-order production rate of endogenous IgG q_{prod} (see Fig. 3.1(right) for an overview of all model parameters). Considering the unknown tissue-dependent parameters would result in estimating 61 parameters. Commonly in PBPK models for mAbs, $\mathrm{FcRn_{tot}}$, k_{in}, k_{out} k_{deg} are assumed tissue-independent and FR is fixed to its reported value in [69] . Appendices A.2 and A.3.1 provide the source of experimental data used for model evaluation and an overview of the methodology for parameter estimation.

Table 3.1: *Detailed PBPK model for mAbs in mice: Summary of parameters*

Parameter			Ref.	Description
V_x	ml	Tab. 3.2		$x = \mathrm{p, i, e}$; plasma, interstitial, endosomal volume (tissue-specific)
Q	ml/min	Tab. 3.2		plasma flow (tissue-specific)
L	ml/min	Tab. 3.2		lymph flow (tissue-specific)
σ_{vas}		0.95	[66, 69]	vascular reflection coefficient
σ_{lymph}		0.20	[69]	lymphatic reflection coefficient
k_{in}	1/day	-	estimated	rate constant of endosomal uptake
k_{out}	1/day	-	estimated	recirculation rate constant of FcRn-bound antibody
FR		0.72	[69]	fraction of recirculated bound antibody
k_{deg}	1/day	-	estimated	degradation rate constant of free antibody from endosomal space (tissue-specific)
FcRn	nM	-	estimated	FcRn capacity
K_D	nM	4.80	[21]	dissociation constant of the antibody-FcRn binding
q_{prod}	nmol/day	-	estimated	zero-order rate constant of endogenous IgG production

In the sequel, we present the founding principles of the simplification of PBPK models for mAbs for the development of a simplified PBPK model to characterize the disposition of mAbs while integrating pharmacologically relevant processes but parameterized by a lesser number of parameters.

3.2 FcRn - IgG interaction

Binding to FcRn plays an important role in the homeostasis of endogenous IgG and the observed long half-life of mAbs in plasma (for details, see paragraph *Pharmacokinetic properties of mAbs*). Understanding FcRn-IgG interaction sheds light on the mechanisms of IgG transport. IgGs bind via their Fc portion with high affinity to FcRn at an acidic pH (< 6.5) but not at a physiological pH. In the latter, we focus on FcRn-mediated salvage which occurs primarily via formation of circulating endosomes in endothelial cells.

Most of published detailed PBPK models [68, 69, 71–73] explicitly consider the binding to FcRn and describe the elimination of FcRn-unbound mAbs from the

Table 3.2: *Detailed PBPK model for mAbs in mice: Tissue-dependent parameters*

		V_{tot}	V_p	V_i	$V_e{}^g$	Q^h	L^i
		mL	mL	mL	10^{-2}mL	mL/min	10^{-2}mL/min
Lung	(lun)	0.191^a	0.019^a	0.057^a	0.096	4.380^a	1.752
Adipose	(adi)	1.750^b	0.001^c	0.236^d	0.875	0.307^e	0.124
Bone	(bon)	1.500^a	0.080^a	0.280^a	0.750	0.170^a	0.068
Gut	(gut)	3.450^a	0.100^a	0.600^a	1.725	0.900^a	0.180
Heart	(hea)	0.133^a	0.007^a	0.019^a	0.067	0.280^a	0.112
Kidney	(kid)	0.298^a	0.030^a	0.101^a	0.149	0.800^a	0.320
Liver	(liv)	0.951^a	0.095^a	0.190^a	0.476	1.100^a	0.220
Muscle	(mus)	7.924^a	0.150^a	1.032^a	3.962	0.800^a	0.320
Skin	(ski)	2.940^a	0.200^a	0.999^a	1.470	1.210^a	0.484
Spleen	(spl)	0.100^a	0.010^a	0.020^a	0.050	0.050^a	0.010
Artery	(art)	0.219^f	0.219^f	-	-	4.380^a	-
Vein	(ven)	0.536^f	0.536^f	-	-	4.380^a	-

[a] from [67, 69]. Note that in [67, 69], the plasma space of each organ/tissue is simplistically denoted as 'vascular space'. See text for more details

[b] 7% of total body weight [102] assuming a body weight of 25 g and a tissue density of 1 g/ml

[c] total vascular volume (V_{vas}) in adipose is 1.00 % of total volume (measured in rats but assumed to be species-independent for mammals) [103]; $V_p = (1 - \text{hct})V_{vas}$ with hct = 0.45 [75]

[d] adipose: 1.35 % of total volume [103]

[e] plasma flow in adipose tissue accounts for 7.0% of total plasma flow [102]

[f] total plasma volume $V_{plasma} = 1.25$ mL (assuming a body weight of 25 g) [75],
$V_{art} = 0.29 \cdot (V_{plasma} - \sum V_{p,tis})$, $V_{ven} = 0.71 \cdot (V_{plasma} - \sum V_{p,tis})$ [102]

[g] assumed to be 0.5 % of tissue volume [69]

[h] the sum of individual organ plasma flows [67, 69, 102] exceeds the observed total plasma flow of vein, lung, and artery [75, for hct = 0.45]. For consistency, we set the total plasma flow to the sum of all plasma flows entering the vein.

[i] assumed to be 2 % and 4 % of plasma flow for visceral and non-visceral organs, respectively [69]
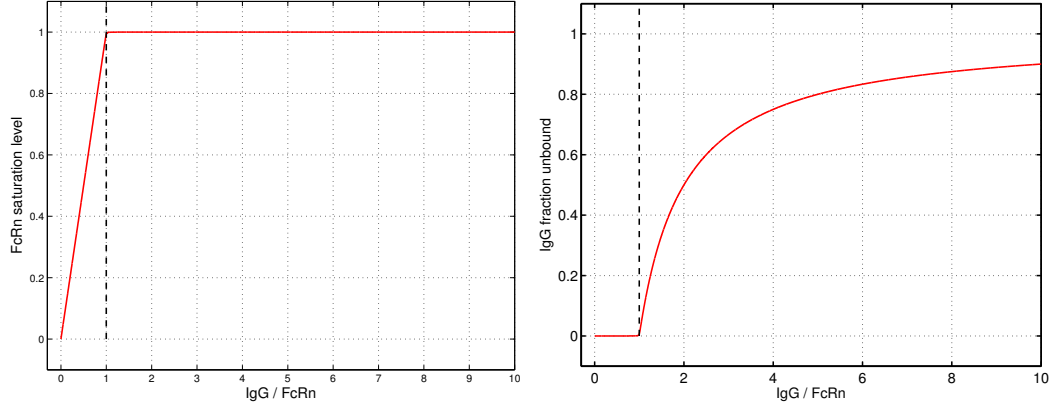
Figure 3.2: *FcRn saturation level (left) and fraction unbound of IgG (right) as a function of the total IgG concentration (stated in units of total FcRn). Due to the high binding affinity of IgG to FcRn, the FcRn saturation level increases practically linearly with IgG concentration, until FcRn is fully saturated. As a consequence, the fraction unbound $\mathrm{fu}_{\mathrm{IgG}}$ of IgG is practically zero until IgG concentration exceeds total FcRn concentration, when it follows the form $\mathrm{fu}_{\mathrm{IgG}} = 1 - \mathrm{FcRn}/\mathrm{IgG}$. We choose $\mathrm{FcRn} = 1e + 5$ nM and $\mathrm{K}_{\mathrm{D}} = 4.8nM$, in line with values reported in Table 4.4.*

endosomal space with a first-order rate constant. Here, we illustrate that under commonly encountered (dosing) conditions, the clearance of mAbs in the endosomal space can be expected to be linear, regardless the level of saturation of FcRn that protects IgGs from degradation.

3.2.1 Role of FcRn and endogenous IgG in modeling mAbs disposition: From saturable IgG-FcRn interaction to linear mAb clearance

Denoting by $\mathrm{IgG}_{\mathrm{mAb}}$ and $\mathrm{IgG}_{\mathrm{endo}}$ the therapeutic and endogenous IgG concentrations in the endosomal space of endothelial cells, the resulting total IgG concentration is given by

$$\mathrm{IgG} = \mathrm{IgG}_{\mathrm{endo}} + \mathrm{IgG}_{\mathrm{mAb}}.$$

In the endosomal space, free IgG binds to free FcRn with a dissociation constant K_{D} forming a IgG - FcRn complex. While the complex is recycled to the interstitial and/or plasma space, free IgG is eventually catabolized in the lysosomes:

$$\mathrm{IgG}_{\mathrm{u}} + \mathrm{FcRn}_{\mathrm{u}} \quad \overset{\mathrm{K}_{\mathrm{D}}}{\longleftrightarrow} \quad \mathrm{IgG}_{\mathrm{b}} \longrightarrow \text{recycling}$$
$$\mathrm{IgG}_{\mathrm{u}} \quad \overset{\mathrm{k}_{\mathrm{deg}}}{\longrightarrow} \quad \text{catabolism}$$
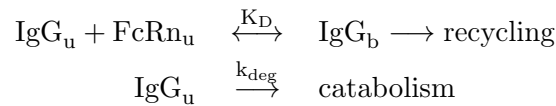
To study the IgG - mAb interaction in more details, free FcRn is denoted by $\mathrm{FcRn}_{\mathrm{u}}$, free and FcRn-bound IgG by $\mathrm{IgG}_{\mathrm{u}}$ and $\mathrm{IgG}_{\mathrm{b}}$, respectively. Consequently, $\mathrm{IgG}_{\mathrm{u}}$ is the sum of the free endogenous and free therapeutic mAb. The two conservation relations

$\text{IgG} = \text{IgG}_\text{u} + \text{IgG}_\text{b}$ and $\text{FcRn} = \text{FcRn}_\text{u} + \text{IgG}_\text{b}$ hold.

In the sequel, we make the assumption that K_D values of IgG_endo and IgG_mAb are comparable. This is a reasonable assumption for most mAbs—however, it does not hold for mAbs with their Fc part engineered for high binding affinity to FcRn.

Binding processes are typically fast compared to the time-scale of other pharmacokinetic processes. Assuming a quasi-steady state for FcRn binding yields $\text{IgG}_\text{u} \cdot \text{FcRn}_\text{u} = \text{K}_\text{D} \cdot \text{IgG}_\text{b}$.

Solving for the bound concentration and exploiting the conservation relations yields

$$\text{IgG}_\text{b} = \frac{\text{FcRn}_\text{u}}{\text{K}_\text{D} + \text{FcRn}_\text{u}} \cdot \text{IgG}. \tag{3.6}$$

Exploiting again the second conservation relation, it results

$$\text{FcRn} = \text{FcRn}_\text{u} + \frac{\text{FcRn}_\text{u}}{\text{K}_\text{D} + \text{FcRn}_\text{u}} \cdot \text{IgG}$$

and finally

$$\text{FcRn}_\text{u} = \frac{1}{2}\Big(\text{FcRn}_\text{eff} + \sqrt{(\text{FcRn}_\text{eff})^2 + 4\text{K}_\text{D} \cdot \text{FcRn}}\Big) \tag{3.7}$$

with $\text{FcRn}_\text{eff} = (\text{FcRn} - \text{IgG} - \text{K}_\text{D})$. This allows to determine the fraction unbound fu_IgG based on eq. (3.6) as

$$\text{fu}_\text{IgG} = \frac{\text{IgG}_\text{u}}{\text{IgG}} = 1 - \frac{\text{IgG}_\text{b}}{\text{IgG}} = \frac{\text{K}_\text{D}}{\text{K}_\text{D} + \text{FcRn}_\text{u}} \tag{3.8}$$

with FcRn_u defined in eq. (3.7).

The level of saturation of FcRn is defined as

$$\text{FcRn saturation level} = \frac{\text{FcRn} - \text{FcRn}_\text{u}}{\text{FcRn}}.$$

Figure 3.2 (left) shows the FcRn-saturation level as a function of the total IgG concentration, expressed in terms of units of total FcRn. One clearly identifies two regimes: (i) for IgG lower than FcRn, the saturation level of FcRn is linearly increasing with increasing IgG concentration; (ii) for IgG larger than total FcRn, the FcRn-saturation level appears to be 1. As shown below in section 3.2.2, this behavior is theoretically justified based on the reasonable assumption that $\text{K}_\text{D} \ll \text{FcRn}$, i.e., that IgG has a very high affinity to FcRn. This assumption is in line with the physiological function of FcRn. For the mAb 7E3 in mice, the estimated total FcRn concentration, from a semi-mechanistic 2-compartment model, is $2.2 \cdot 10^5$ nM, while the reported K_D is 4.8

nM (see Table 4.4), thereby supporting the assumption $K_D \ll FcRn$.

As shown in Figure 3.2 (right), the fraction unbound fu_{IgG} also exhibits two regimes: (i) a phase of IgG concentration below FcRn, where fu_{IgG} is almost zero, and (ii) a phase of hyperbolic increase for IgG above FcRn. This behavior is again justified theoretically, as shown in section 3.2.2 and summarizes as

$$fu_{IgG} = \begin{cases} 0; & IgG \leq FcRn \\ 1 - \frac{FcRn}{IgG}; & IgG > FcRn \end{cases}.$$

Without the underlying theoretical justification, such a model is proposed in [64], termed the cutoff model, based on some cutoff value 'MAX' (that is identified to total FcRn capacity).

The above derivations have direct impact on modeling the endosomal clearance and the FcRn-mediated salvage mechanism for a large number of mAbs. If the total IgG concentration is dominated by endogenous IgG and hardly perturbed by the administration of therapeutic IgG, i.e, $IgG_{mAb} \ll IgG_{endo}$, which implies $IgG \approx IgG_{endo}$, then the fraction unbound of mAb is constant, i.e.,

$$fu_{mAb} = fu_{IgG} \approx fu_{IgG_{endo}} = const. \tag{3.9}$$

Such a situation is quite common for many mAbs. In mice, the baseline concentration of endogenous plasma IgG is reported to be 1.47e+4 nM in [60] and [104]. In [64], Xiao shows that the administration of an i.v. bolus of 8 mg/kg mAb (7E3) does not affect the overall endogenous plasma level of IgG. Under such conditions, the extent of saturation of FcRn and consequently the fraction unbound fu_{mAb} only depend on the endogenous IgG concentration; in other words, it is set by the endogenous IgG levels.

3.2.2 Theoretical derivation of FcRn saturation level and fraction unbound of mAb

The special form of the dependence of the FcRn saturation level, i.e.

$$FcRn \text{ saturation level} = 1 - \frac{FcRn_u}{FcRn} \tag{3.10}$$

on the total IgG concentration is justified from eq. (3.7). To this end, we introduce the parameters

$$\epsilon = \sqrt{\frac{K_D}{FcRn}} \quad \text{and} \quad x = 1 - \epsilon^2 - \frac{IgG}{FcRn}.$$

Due to the tight binding of endogenous IgG and mAb to FcRn, i.e. $K_D \ll FcRn$, one can make the reasonable assumption that ϵ is very small, i.e., $\epsilon \ll 1$. For 7E3 in

mice, we estimate $\epsilon < 5 \cdot 10^{-3}$ from Table 4.4. Dividing in eq. (3.7) both sides by FcRn yields the fraction unbound of FcRn:

$$\frac{\text{FcRn}_{\text{u}}}{\text{FcRn}} = \frac{1}{2}\left(1 - \epsilon^2 - \frac{\text{IgG}}{\text{FcRn}} + \sqrt{\left(1 - \epsilon^2 - \frac{\text{IgG}}{\text{FcRn}}\right)^2 + 4\epsilon^2}\right), \qquad (3.11)$$

or $\text{FcRn}_{\text{u}}/\text{FcRn} = 1/2 \cdot (x + \sqrt{x^2 + 4\epsilon^2})$. When $\text{IgG}/\text{FcRn} = (1 - \epsilon^2)$, i.e., when the (total) IgG concentration is approximately equal to the (total) FcRn concentration, it is $x = 0$ and therefore $\text{FcRn}_{\text{u}}/\text{FcRn} = \epsilon$. The larger the IgG concentration, the larger the bound fraction of FcRn and the smaller the unbound fraction of FcRn. Thus, $\text{IgG}/\text{FcRn} \geq (1 - \epsilon)$ implies

$$\frac{\text{FcRn}_{\text{u}}}{\text{FcRn}} \leq \epsilon. \qquad (3.12)$$

This finally results in the lower bound of FcRn saturation level, such that

$$\text{FcRn saturation level} = 1 - \frac{\text{FcRn}_{\text{u}}}{\text{FcRn}} \geq 1 - \epsilon \qquad (3.13)$$

for $\text{IgG}/\text{FcRn} \geq (1 - \epsilon)$. For small IgG concentrations with $\epsilon < x$ in the upper bound, we use a simple estimate of the square-root term $\sqrt{x^2 + 4\epsilon^2} < \sqrt{x^2 + 4x\epsilon}$ and apply the Taylor expansion to the first order

$$\sqrt{x^2 + 4\epsilon x} \quad \doteq \quad x + 2\epsilon$$

for $x \gg \epsilon$. This results in

$$\frac{\text{FcRn}_{\text{u}}}{\text{FcRn}} \quad \leq \quad 1 - \epsilon^2 - \frac{\text{IgG}}{\text{FcRn}} + \epsilon.$$

Also, neglecting the $4\epsilon^2$ term in the square root in eq. (3.11) yields

$$1 - \epsilon^2 - \frac{\text{IgG}}{\text{FcRn}} \leq \frac{\text{FcRn}_{\text{u}}}{\text{FcRn}}.$$

From these two inequalities and eq. (3.10) we finally obtain

$$\frac{\text{IgG}}{\text{FcRn}} - \epsilon \cdot (1 - \epsilon) \leq \text{FcRn saturation level} < \frac{\text{IgG}}{\text{FcRn}} + \epsilon^2 \qquad (3.16)$$

for $x \gg \epsilon$, i.e., $\text{IgG}/\text{FcRn} \ll 1 - \epsilon - \epsilon^2$. Taken together, eqs. (3.13) and (3.16) theoretically justify the peculiar form of the FcRn-saturation level depicted in Fig. 3.2 (left).

The above derivation also permits to theoretically justify the dependence of the fraction unbound fu_{IgG} on IgG, as shown in Fig. 3.2 (right). For $\text{IgG}/\text{FcRn} = (1 - \epsilon^2)$ it is $\text{FcRn}_{\text{u}}/\text{FcRn} = \epsilon$ as before, and

$$\begin{aligned}
\text{fu}_{\text{IgG}} &= \frac{\text{K}_{\text{D}}}{\text{K}_{\text{D}} + \text{FcRn}_{\text{u}}} = \frac{\epsilon^2}{\epsilon^2 + \text{FcRn}_{\text{u}}/\text{FcRn}} \\
&= \frac{\epsilon^2}{\epsilon^2 + \epsilon} = \frac{\epsilon}{1 + \epsilon} < \epsilon.
\end{aligned}$$

Since fu_{IgG} decreases monotonically with decreasing IgG concentration, the bound $fu_{IgG} < \epsilon$ continues to hold for all $IgG < (1 - \epsilon) \cdot FcRn$.

For larger IgG concentrations, we consider the relation

$$
\begin{aligned}
fu_{IgG} &= \frac{IgG_u}{IgG} = \frac{IgG - (FcRn - FcRn_u)}{IgG} \\
&= 1 - \frac{FcRn}{IgG} + \frac{FcRn_u}{FcRn} \cdot \frac{FcRn}{IgG},
\end{aligned}
$$

where $IgG_b = FcRn_b = FcRn - FcRn_u$.

For $IgG/FcRn \geq (1 - \epsilon^2)$ together with (3.12), it yields the inequality

$$
1 - \frac{FcRn}{IgG} \leq fu_{IgG} < 1 - \frac{FcRn}{IgG} + \epsilon \cdot (1 - \epsilon), \tag{3.19}
$$

where the first inequality trivially follows from eq. (3.18). Taken together, eqs. (3.17) and (3.19) theoretically justify the peculiar form of the fraction unbound of IgG depicted in Fig. 3.2 (right).

3.3 *Intermediate* PBPK model

Herein, we provide the rational to simplify the tissue model with *implicit* consideration of FcRn-binding in the endosomal space.
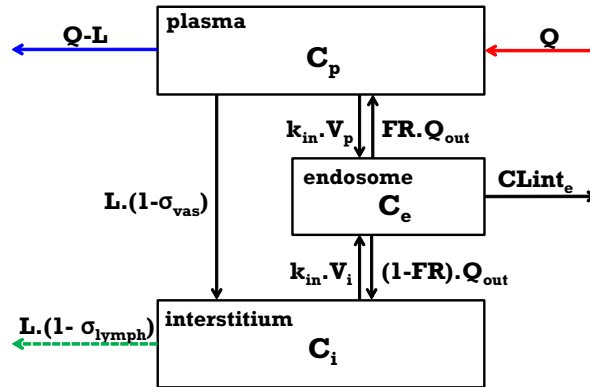
Figure 3.3: *Intermediate tissue model comprising a plasma compartment, endosomal and interstitial spaces. Q and L represent plasma and lymph flows, σ_{vas} and σ_{lymph} denote the vascular and lymphatic reflection coefficients, k_{in} is the rate constant of uptake of endogenous IgG and mAb from the plasma or interstitial space into the endosomal space. Q_{out} is the total FcRn-mediated outflow from the endosomal space (with a fraction FR recycled into the vascular space), while $CLint_e$ denotes the linear endosomal intrinsic clearance.*

3.3.1 Intermediate complexity of the PBPK model

The authors in [69] *explicitly* consider endogenous IgG in their model—in addition to therapeutic mAb to account for the competition for binding to FcRn. Based on the observation preceding eq. (3.9) and thereon based derivations, the detailed tissue model is greatly simplified by *implicitly* considering endogenous IgG. It is indeed assumed that the fraction unbound of mAb in the endosome is constant. Therefore, we define the total FcRn-mediated outflow and the endosomal intrinsic clearance as

$$
\begin{aligned}
\mathrm{Q_{out}} &= \mathrm{k_{out}} \cdot (1 - \mathrm{fu}) \cdot \mathrm{V_e} \\
\mathrm{CLint_e} &= \mathrm{CL_e} \cdot \mathrm{fu}.
\end{aligned}
$$

This is the basis for an intermediate complexity of a PBPK model describing mAbs disposition.

The intermediate PBPK model comprises 32 compartments representing the most relevant anatomical spaces involved in mAb disposition (see Fig. 3.1, left): venous (ven) and arterial (art) plasma as well as the vascular plasma (p), endosomal (e) and interstitial (i) spaces of ten tissues, i.e. lung, adipose, bone, heart, kidney, muscle, skin, gut, spleen and liver (see Fig. 3.3 for the intermediate tissue model). In addition to the processes at the tissue level, the model incorporates the distribution of mAb via the plasma flow and the convective transport via lymph flow from the interstitial spaces to the plasma circulation. The rates of change of all concentrations are given by

$$
\begin{aligned}
\mathrm{V_{ven}} \frac{\mathrm{d}}{\mathrm{dt}} \mathrm{C_{ven}} &= + \mathrm{Q_{ven}} \cdot (\mathrm{C_{in,ven}} - \mathrm{C_{ven}}) \\
&\quad + \sum_{\mathrm{tis}} \mathrm{L_{tis}} \cdot (1 - \sigma_{\mathrm{lymph}}) \cdot \mathrm{C_{i,tis}}
\end{aligned}
\tag{3.20}
$$

$$
\mathrm{tis} = \mathrm{lun, adi, bon, gut, hea, kid, liv, mus, ski, spl}
$$

$$
\mathrm{V_{art}} \frac{\mathrm{d}}{\mathrm{dt}} \mathrm{C_{art}} = (\mathrm{Q_{lun}} - \mathrm{L_{lun}}) \cdot \mathrm{C_{p,lun}} - \mathrm{Q_{art}} \cdot \mathrm{C_{art}}
\tag{3.21}
$$

$$
\begin{aligned}
\mathrm{V_{p,tis}} \frac{\mathrm{d}}{\mathrm{dt}} \mathrm{C_{p,tis}} &= \mathrm{Q_{tis}} \cdot \mathrm{C_{in,tis}} - (\mathrm{Q_{tis}} - \mathrm{L_{tis}}) \cdot \mathrm{C_{p,tis}} \\
&\quad - \mathrm{L_{tis}} \cdot (1 - \sigma_{\mathrm{vas}}) \cdot \mathrm{C_{p,tis}} - \mathrm{k_{in}} \cdot \mathrm{V_{p,tis}} \cdot \mathrm{C_{p,tis}} \\
&\quad + \mathrm{FR} \cdot \mathit{Q}_{\mathrm{out,tis}} \cdot \mathrm{C_{e,tis}}
\end{aligned}
\tag{3.22}
$$

$$
\begin{aligned}
\mathrm{V_{e,tis}} \frac{\mathrm{d}}{\mathrm{dt}} \mathrm{C_{e,tis}} &= + \mathrm{k_{in}} \cdot \mathrm{V_{p,tis}} \cdot \mathrm{C_{p,tis}} + \mathrm{k_{in}} \cdot \mathrm{V_{i,tis}} \cdot \mathrm{C_{i,tis}} \\
&\quad - \mathit{Q}_{\mathrm{out,tis}} \cdot \mathrm{C_{e,tis}} - \mathrm{CLint_e} \cdot \mathrm{C_{e,tis}}
\end{aligned}
\tag{3.23}
$$

$$
\begin{aligned}
\mathrm{V_{i,tis}} \frac{\mathrm{d}}{\mathrm{dt}} \mathrm{C_{i,tis}} &= + \mathrm{L_{tis}} \cdot (1 - \sigma_{\mathrm{vas}}) \cdot \mathrm{C_{p,tis}} \\
&\quad - \mathrm{L_{tis}} \cdot (1 - \sigma_{\mathrm{lymph}}) \cdot \mathrm{C_{i,tis}} - \mathrm{k_{in}} \cdot \mathrm{V_{i,tis}} \cdot \mathrm{C_{i,tis}} \\
&\quad + (1 - \mathrm{FR}) \cdot \mathit{Q}_{\mathrm{out,tis}} \cdot \mathrm{C_{e,tis}}.
\end{aligned}
\tag{3.24}
$$

For all tissues except vein, artery, liver and lung, the inflowing concentration C_{in} is given by $C_{in,tis} = C_{art}$. For lung, it is $C_{in,lun} = C_{ven}$.
For vein, it is

$$Q_{ven}C_{in,ven} = \sum_{tis} (Q_{tis} - L_{tis}) \cdot C_{p,tis}$$

with $tis = adi, bon, hea, kid, liv, mus, ski$.
For liver, it is

$$
\begin{aligned}
Q_{liv}C_{in,liv} &= \sum_{tis}(Q_{tis} - L_{tis}) \cdot C_{p,tis} \\
&+ \left(Q_{liv} - \sum_{tis} Q_{tis}\right) \cdot C_{art}
\end{aligned}
$$

with $tis = gut, spl$. As previously described, the mAb 7E3 is administered via i.v. bolus. For vein, the initial condition of the above system of differential equations is set to

$$C_{ven}(0) = \frac{dose}{V_{ven}},$$

while $C_{cmt}(0) = 0$ is set for all other compartments 'cmt'.

3.3.2 Model parameterization

A description of all parameters of the intermediate PBPK model is given in Table 3.3. Physiological and anatomical data are reported in Table 3.2.

Given the new parameterization of the tissue model, the intermediate PBPK model is 'decoupled' to describe data in FcRn-KO and WT mice. For FcRn-KO mice, the endosomal rate constant of uptake k_{in} and the tissue-specific endosomal intrinsic clearance, $CLint_{e,ko}$ are estimated by fitting the PBPK model to FcRn-KO data only. For WT mice, the unknown parameters are (i) the rate constant of uptake in the endosomal space, k_{in}; (ii) the tissue-specific endosomal intrinsic clearance, $CLint_{e,wt}$; (iii) the tissue-specific total FcRn-mediated outflow from the endosomal space, Q_{out}. All parameters are estimated simultaneously by fitting the intermediate PBPK model stated in eqs. (3.20)-(3.24) to experimental plasma and tissue data in mice for the mAb, 7E3. The experimental data are treated as described in appendix A.2. We further assume that k_{in} is tissue-independent. The fraction of recirculated bound antibody is set to FR = 0.715, as published in [69]. The number of remaining unknown parameters is 11 for FcRn-KO mice and 21 for WT mice.

Table 3.3: *Intermediate PBPK model for mAbs in mice: Summary of parameters*

Parameter			Ref.	Description
V_x	ml	Tab. 3.2		$x = $ p, i, e; plasma, interstitial, endo-somal volume (tissue-specific)
Q	ml/min	Tab. 3.2		plasma flow (tissue-specific)
L	ml/min	Tab. 3.2		lymph flow (tissue-specific)
σ_{vas}		0.95	[66, 69]	vascular reflection coefficient
σ_{lymph}		0.20	[69]	lymphatic reflection coefficient
k_{in}	1/day	-	estimated	endosomal uptake rate
Q_{out}	ml/min	-	estimated	total FcRn-mediated outflow (tissue-specific)
FR		0.72	[69]	fraction of recirculated bound antibody (see also Discussion section for comment on identifiability)
$CLint_{\text{e}}$	ml/min	-	estimated	endosomal intrinsic clearance (tissue-specific)

3.3.3 Parameter identifiability

Estimation of the unknown parameters is highly sensitive to initial values and several sets of parameters could accurately characterize the venous plasma data and the tissue data. A more detailed description of the methodology for parameter estimation and model performance is presented in Appendices A.4.1 and A.4.2. When sensitive to initial values, the estimated parameters have to be read and interpreted with caution. One might argue against the validity of such a PBPK model. For monoclonal antibodies, given common experimental data (only plasma, or plasma and tissue data), it appears that it is not possible to reliably identify the unknown parameters and infer which tissues are eliminating. Therefore, it is very unlikely that the level of detailedness of the tissue model can be supported by commonly available data.

3.4 Discussion

In this chapter, we assess the relevance to explicitly integrate the binding of endogenous IgG and the therapeutic mAb to FcRn in detailed PBPK models, in absence of target. The detailed PBPK model published in [69] is extended and explicitly accounts for the non-linear and competitive binding of endogenous IgG and mAb to FcRn. It enables to analyze the relation between FcRn saturation level and steady-state endogenous

IgG level and its impact on mAb disposition. While the analysis is based on the mAb 7E3 in mice, the conclusions drawn hold under more general conditions.

Binding to FcRn is a potentially saturable process, giving rise to the question whether FcRn binding has to be, if at all, included as a non-linear or a linear process in pharmacokinetic models. Based on the detailed PBPK model of therapeutic mAb and endogenous IgG disposition in mice, we demonstrate that mAb binding to FcRn can be considered linear if (i) both mAb and endogenous IgG have comparable affinities to FcRn; and (ii) $IgG_{mAb} \ll IgG_{endo}$. In mice, the baseline concentration of endogenous IgG in plasma is reported to be 1.47e+4 nM in [60, 104]. In [64], Xiao shows that the administration of an i.v. bolus of 8 mg/kg therapeutic IgG (7E3) does not affect the plasma and endosomal levels of endogenous IgG. This implies that $mAb_{tot} \ll$ endogenous IgG_{tot} in the plasma and in the endosomal space such that the level of saturation of FcRn is 'dictated' solely by the concentration of endogenous IgG. From the point of view of the therapeutic mAb, binding to FcRn is therefore linear. The assumption holds for other relevant situations. For example, in healthy men, the mean concentration of total endogenous IgG is 65 μM [105]. For an exemplary set of 7 mAbs registered at the European Medicines Agency (EMA) in human (cetuximab [106], infliximab [107], rituximab [108], trastuzumab [109], golimumab [110] and tocilizumab [111]), the mean maximum concentrations C_{max} following single or multiple administration of the therapeutic dose vary from 20.6 nM to 3.2 μM, thus being 1-3 orders of magnitude lower than the concentration of IgG_{endo}.

The results on the fraction unbound fu_{IgG} in the different endosomal spaces presented in Fig. 3.2(right) show a very distinct behavior: The fraction unbound of IgG is either almost zero or close to one. This behavior is due to the low dissociation constant in comparison to the much larger total FcRn concentration. As a result, effectively all endogenous IgG is bound to FcRn whenever its concentration is below $FcRn_{tot}$. The free endogenous IgG concentration only effectively rises, if endogenous $IgG_{tot} > FcRn_{tot}$, in which case free IgG_{endo} is approximately identical to $FcRn_{tot} - IgG_{tot}$. This result is general in nature and applies to any protein binding situation where the dissociation constant is much smaller then the total binding protein concentration. Consequently, even for varying total FcRn concentration in the endosomal spaces of the different tissues and organs, the results continue to hold as long as $K_D \ll FcRn_{tot}$. In addition, the results also extend to the situation in which FcRn is not present at all or present at very low concentration in some endosomal spaces. In this case, it is $fu_{IgG} = 1$, as for compartments, where endogenous $IgG_{tot} \gg FcRn_{tot}$. These findings are in line with the recent results reported by Xiao [64]. The proposed cutoff model accounts for the non linear binding to FcRn in the peripheral compartment. The resulting fraction unbound of IgG_{tot} is derived from

a hypothetical FcRn-capacity and the total IgG concentrations which presents the same biphasic behavior.

These results provide further evidence that the therapeutic mAb can exhibit time-independent linear i.e. FcRn-mediated clearance, even if the FcRn system is not fully saturated. This is in line with more recent experimental findings reported in [3] and can explain the explicit linear component of the clearance in the cutoff model in [64].

In the PBPK model, fu is derived from the total capacity of FcRn and the total concentration of IgG_{endo} in the endosome. The current lack of data and understanding of the processes governing (i) FcRn expression level, (ii) FcRn turnover, (iii) IgG_{endo} production and (iv) IgG_{endo} concentrations in the endosomal space does not allow the estimation of physiological meaningful and accurate endosomal FcRn total concentration as well as endogenous IgG production rate. The present findings on the linear fu_{IgG} based on the assumptions that $FcRn_{tot}$ and IgG_{endo} concentrations in the endosomal space are not influenced upon the mAb administration and therefore remain constant over time allow to simplify the detailed PBPK model at the organ level. $FcRn_{tot}$ and IgG_{endo} are implicitly considered in the *intermediate* PBPK model and are no longer estimated parameters. The parameters to be determined are (i) the rate constant of uptake in the endosomal space, k_{in}; (ii) the tissue-specific endosomal intrinsic clearance, $CLint_{e,wt}$; (iii) the tissue-specific total FcRn-mediated outflow from the endosomal space, Q_{out}. As in [73], the estimation process is unstable and unknown parameters are not identifiable. This clearly indicates that the intermediate PBPK model is still over parameterized given the solely plasma and total tissue concentrations currently available. This observation is the grounds for further simplification, derived thereafter.

Simplified PBPK Model for mAbs

The novel PBPK model to characterize the disposition of mAbs is obtained from the intermediate PBPK model (detailed in Chapter 3, section 3.3) by simplification of the tissue model. The resulting simplified tissue model is characterized by a single ODE for all tissues and integrates the linear component of the clearance of mAbs such that it provides insight on the characterization of the tissues involved in mAbs elimination.

The resulting simplified PBPK model for mAb disposition is a whole-body model with extravasation rate-limited tissue distribution and elimination potentially occurring from various tissues and plasma.

4.1 Simplification of the tissue model

The reduction of the tissue model is justified based on time-scale arguments. To this end, we consider the generic ODE for the rate of change of the concentration C_{cmt} of some compartment 'cmt' with inflow Q_{inflow} and outflow $Q_{outflow}$:

$$V_{cmt}\frac{d}{dt}C_{cmt} = Q_{inflow} \cdot C_{in} - Q_{outflow} \cdot C_{cmt}.$$

The response time τ_{cmt}—i.e., the time scale which the compartment concentration responses to changes in the inflowing concentration C_{in}—is given by

$$\tau_{cmt} = \frac{\ln(2)}{Q_{outflow}/V_{cmt}}.$$

Hence, small compartments or compartments with large *outflow* respond quickly to changes of inflow. Of note, the inflow Q_{inflow} influences only the concentration levels C_{cmt} and its steady state concentration, but has no impact on the response time.

4.1.1 Lumping all vascular spaces and tissue sub-compartments

In view of the system of ODEs eq. (3.20)-(3.24), three groups of compartments presenting different response times are identified and supported by parameters values published in [69–71, 73] and physiological insight:

- *Fast:* Arterial and venous plasma and peripheral plasma of all tissues with response times

$$\tau_{\mathrm{art}} = \frac{\ln(2)}{Q_{\mathrm{art}}/V_{\mathrm{art}}}; \quad \tau_{\mathrm{ven}} = \frac{\ln(2)}{Q_{\mathrm{ven}}/V_{\mathrm{ven}}},$$

  and

$$\tau_{\mathrm{p,tis}} = \frac{\ln(2)}{(Q_{\mathrm{tis}} - L_{\mathrm{tis}})/V_{\mathrm{p,tis}}},$$

  with τ_{pla} the average of the above response times.

- *Intermediate:* The interstitial space of all tissues, with response times

$$\tau_{\mathrm{i}} < \frac{\ln(2)}{(1 - \sigma_{\mathrm{lymph}})L_{\mathrm{tis}}/V_{\mathrm{i,tis}}},$$

  with τ_{int} the average of the above response times.

  Comparison to plasma response time: V_{pla} and V_{i} are of the same order of magnitude (e.g. [67]), while L_{tis} is about two-orders of magnitude smaller than Q_{tis}, and $(1 - \sigma_{\mathrm{lymph}}) = 0.8$ [69]. Consequently, the response time of plasma & vascular compartments is approximately two-orders of magnitude faster than of the interstitial compartments, i.e., $\tau_{\mathrm{pla}} \ll \tau_{\mathrm{int}}$. Of note, the much slower inflow corresponding to $(1 - \sigma_{\mathrm{vas}}) \cdot L_{\mathrm{tis}}$ does not influence the response time, it only influences the interstitial concentration levels.

- *Slow:* The endosomal space of all tissues, with response times

$$\tau_{\mathrm{e}} < \frac{\ln(2)}{(Q_{\mathrm{out,tis}} + \mathrm{CLint}_{\mathrm{e}})/V_{\mathrm{e}}} \leq \frac{\ln(2)}{Q_{\mathrm{out,tis}}/V_{\mathrm{e}}},$$

  with τ_{end} the average of the above response times.

  According to [69], V_{e} is approximately two-orders of magnitude smaller than V_{i}, while $Q_{\mathrm{out,tis}}$ is five orders of magnitude smaller than Q_{tis} and therefore three orders of magnitude smaller than L_{tis}. Consequently, the response time of the interstitial compartment is approximately one order of magnitude faster than for the endosomal compartment, i.e., $\tau_{\mathrm{int}} < \tau_{\mathrm{end}}$.

The above time-scale considerations suggest to lump arterial and venous plasma and all peripheral plasma spaces, resulting in a lumped plasma compartment with total plasma volume V_{pla} and plasma concentration defined by

$$V_{\mathrm{pla}} \cdot C_{\mathrm{pla}} = V_{\mathrm{art}} \cdot C_{\mathrm{art}} + V_{\mathrm{ven}} \cdot C_{\mathrm{ven}} + \sum_{\mathrm{tis}} V_{\mathrm{p,tis}} \cdot C_{\mathrm{p,tis}}.$$

Due to the large uncertainty of parameters related to the endosomal space, the choice is made to lump the interstitial and endosomal spaces of each tissue. For easier

comparison to experimental data, the intracellular space with volume V_c is also included. The tissue volume becomes $V_{tis} = V_i + V_e + V_c$ and the tissue concentration

$$V_{tis} \cdot C_{tis} = V_i \cdot C_i + V_e \cdot C_e + V_c \cdot C_c.$$

Since the mAb—in the absence of target—does not distribute in the intracellular space, it is $C_c = 0$.

4.1.2 Derivation of the ODEs for the *simplified* PBPK model

From the above time-scale considerations and the resulting lumping, it follows the ODEs describing the rate of change of C_{pla} and C_{tis} in the different tissues. For plasma, it is

$$
\begin{aligned}
V_{pla}\frac{d}{dt}C_{pla} &= V_{art}\frac{d}{dt}C_{art} + V_{ven}\frac{d}{dt}C_{ven} + \sum_{tis} V_{p,tis}\frac{d}{dt}C_{p,tis} \\
&= \sum_{tis} L_{tis} \cdot (1 - \sigma_{lymph}) \cdot C_{i,tis} + FR \cdot Q_{out,tis} \cdot C_{e,tis} \\
&\quad - (L_{tis} \cdot (1 - \sigma_{vas}) + V_{p,tis} \cdot k_{in}) \cdot C_{p,tis}.
\end{aligned}
$$

The equation for plasma is derived from $C_{pla} = C_{ven} = C_{art} = C_{p,tis}$ and the following assumptions: (i) Since it is difficult to distinguish between the two-pore-related and the fluid-phase endocytosis component of the vascular extravasation, i.e., $L_{tis} \cdot (1 - \sigma_{vas})$ versus $V_{p,tis} \cdot k_{in}$, the single term $(L_{tis} \cdot (1 - \sigma_{tis}))$ similar to the one-pore formalism is derived and allows to introduce an effective lumped reflection coefficient σ_{tis} such that

$$L_{tis} \cdot (1 - \sigma_{tis}) = L_{tis} \cdot (1 - \sigma_{vas}) + V_{p,tis} \cdot k_{in};$$

Further, (ii) since all tissue sub-compartments are lumped, C_e and C_i are considered as multiples of the lumped concentration C_{tis}, i.e. $C_e = \alpha \cdot C_{tis}$ and $C_i = \beta \cdot C_{tis}$. Writing $Q_{out,tis}$ as a fraction δ of the lymph flow L_{tis} yields

$$
\begin{aligned}
& L_{tis} \cdot (1 - \sigma_{lymph}) \cdot C_{i,tis} + FR \cdot Q_{out,tis} \cdot C_{e,tis} \\
&= L_{tis} \cdot \big((1 - \sigma_{lymph}) \cdot \beta + FR \cdot \delta \cdot \alpha\big) \cdot C_{tis}
\end{aligned}
$$

and allows to define the tissue partition coefficient, K_{tis}, as

$$\frac{1}{K_{tis}} = (1 - \sigma_{lymph}) \cdot \beta + FR \cdot \alpha \cdot \delta \tag{4.2}$$

As a consequence, the ODE for the rate of change of the plasma concentration is

$$V_{pla}\frac{d}{dt}C_{pla} = \sum_{tis} L_{tis} \cdot \frac{C_{tis}}{K_{tis}} - L_{tis} \cdot (1 - \sigma_{tis}) \cdot C_{pla},$$

For the tissue concentration C_{tis}, it is

$$
\begin{aligned}
V_{tis}\frac{d}{dt}C_{tis} &= V_i\frac{d}{dt}C_i + V_e\frac{d}{dt}C_e + V_c\frac{d}{dt}C_c \\
&= (L_{tis}\cdot(1-\sigma_{vas}) + V_{p,tis}\cdot k_{in})\cdot C_{p,tis} \\
&\quad -L_{tis}\cdot(1-\sigma_{lymph})\cdot C_{i,tis} - FR\cdot Q_{out,tis}\cdot C_{e,tis} \\
&\quad -CLint_e\cdot C_{e,tis}.
\end{aligned}
$$

Defining the intrinsic tissue clearance $CLint_{tis} = CLint_e\cdot\alpha$ and using the same assumptions and arguments as above yields

$$
V_{tis}\frac{d}{dt}C_{tis} = L_{tis}\cdot(1-\sigma_{tis})\cdot C_{pla} - L_{tis}\cdot\frac{C_{tis}}{K_{tis}} - CLint_{tis}\cdot C_{tis}.
$$

The simplified PBPK model is derived from the more detailed intermediate PBPK model by considering time-scale separation and additional well-grounded assumptions. The resulting number of equations is reduced by a factor of approximately 6 and 3 in comparison to [69] and [73], respectively.

4.2 *Simplified* PBPK model

The model accounts for the anatomical compartments plasma, lung, adipose, bone, gut, heart, kidney, liver, muscle, skin and spleen. The tissue topology and model structure is shown in Fig. 4.1.

The plasma compartment with volume V_{pla} comprises total arterial and venous plasma, including the vascular space associated with the tissues. The tissue compartments with volume V_{tis} account for interstitial, endosomal and intracellular spaces, as described for the detailed tissue model in Fig. 3.3. Exchange between plasma and tissue is described in terms of the tissue lymph flow L_{tis}, a tissue partition coefficient K_{tis} and a reflection coefficient σ_{tis}. Each tissue is potentially involved in elimination with intrinsic tissue clearance $CLint_{tis}$ in addition to a plasma clearance $CLpla$.

4.2.1 Equations of the *simplified* PBPK model

The simplified PBPK model accounts for the rate of change of the concentrations C_{pla} in plasma and C_{tis} in the different tissues. It is described by the system of ODEs:

$$
\begin{aligned}
V_{tis}\frac{d}{dt}C_{tis} &= L_{tis}\cdot\left((1-\sigma_{tis})\cdot C_{pla} - \frac{C_{tis}}{K_{tis}}\right) \\
&\quad - CLint_{tis}\cdot C_{tis}
\end{aligned}
\tag{4.8}
$$

$$
\begin{aligned}
V_{pla}\frac{d}{dt}C_{pla} &= L_{pla}\cdot\left(C_{in} - (1-\sigma_{pla})\cdot C_{pla}\right) \\
&\quad - CLpla\cdot C_{pla},
\end{aligned}
\tag{4.9}
$$
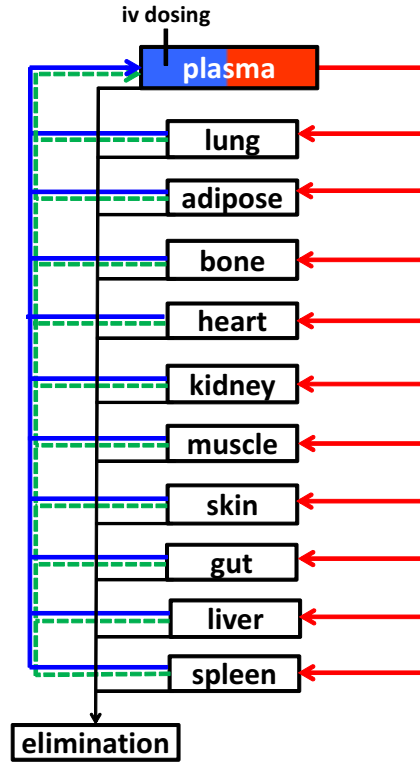
Figure 4.1: *Topology of the simplified PBPK model for mAbs. Tissues are interconnected by plasma (red and blue arrows) and lymph (green dashed arrows) flows. The plasma compartment comprises total arterial and venous plasma, including the vascular plasma space associated with the tissues. The tissue compartments account for interstitial, endosomal and intracellular spaces. Each tissue (except for plasma) has the potential to play a role in the elimination of IgGs, represented with black arrows.*

where the first equation (eq. 4.8) applies to all tissues.

The inflowing concentration C_{in} into plasma is defined by

$$L_{pla} \cdot C_{in} = \sum_{tis} L_{tis} \cdot \frac{C_{tis}}{K_{tis}},$$

where the sum is taken over all considered tissues. For the plasma compartment, the total lymph flow L_{pla} and the apparent total reflection coefficient σ_{pla} are defined as

$$L_{pla} = \sum_{tis} L_{tis} \quad \text{and} \quad L_{pla} \cdot (1 - \sigma_{pla}) = \sum_{tis} L_{tis} \cdot (1 - \sigma_{tis}).$$

For an i.v. bolus administration, the initial conditions at time $t = 0$ were set to $C_{pla}(0) = \text{dose}/V_{pla}$ and $C_{tis}(0) = 0$ otherwise. A full set of parameter values for mice is given in Tables 4.2-4.6.

The above system of ODEs include several physiological processes known to be relevant for mAb disposition: (i) tissue uptake by convection through large pores

and transcytosis, the parameter σ_{tis} is an effective parameter accounting for the fact that only a fraction $(1 - \sigma_{\text{tis}})$ of the plasma concentration is accessible for these processes; (ii) back-flow into the plasma space via the lymph flow or via transcytosis. In the simplified PBPK model, the tissue partition coefficient K_{tis} accounts for processes influencing tissue distribution and can be interpreted as the tissue-to-accessible plasma concentration partition coefficient; (iii) elimination of therapeutic antibodies via several processes, like e.g., degradation into the endosomes, Fcγ receptor-mediated clearance, nonspecific endocytosis. These different elimination processes are described as a whole by $CLint_{\text{tis}}$ and $CLpla$.

The most important assumptions underlying the derivation of the ODEs are (i) the dissociation constants of therapeutic mAb and endogenous IgG to FcRn are similar; (ii) the mAb concentration in plasma is lower than the plasma concentration of endogenous IgG. This is generally expected to be the case with the notable exception of intra-venous immunoglobulin (IVIG) therapy; (iii) there is no target present (the theoretical derivation to include a membrane-bound target is presented in Chapter 6). Under the conditions (i) and (ii), considered in section 3.2.1, there is no need to explicitly account for endogenous IgG and the competitive binding to FcRn in the endosomal space, since the clearance term resulting from catabolism in the endosomes is shown to be linear, regardless the saturation level of FcRn.

In summary, the simplified PBPK model describes the disposition of mAbs assuming an extravasation rate-limited tissue distribution and linear elimination occurring from several sites.

4.2.2 Model parameterization

A description of the parameters of the simplified PBPK model is given in Table 4.1. Physiological and anatomical data are taken from [67, 69, 75, 102, 103, 113]. The original parameters are summarized in Table 4.2 and the derived parameters in Table 4.3. Note that in [67, 69], the plasma space of each tissue is simplistically denoted as 'vascular space'. Hence, the plasma volume of each tissue in the simplified PBPK model is equivalent to the values of the 'vascular volume' in [67, 69]. There are reports about differences in vasculature pore size between tissues [86] and are implemented in PBPK models in [73] and in [113, Chapter III, p. 74 and Table V, p. 107]. Based on simulations, we identify three groups of tissues with different reflection coefficients: $\sigma_{\text{tis}} = 0.98$ for adipose, bone, muscle and skin; $\sigma_{\text{tis}} = 0.95$ for gut, liver and spleen; $\sigma_{\text{tis}} = 0.90$ for heart, kidney and lung.

Table 4.1: *Simplified PBPK model for mAbs in mice: Summary of parameters*

Parameter			Ref.	Description
V_{tis}	mL	Tab. 4.3	[67, 69, 102]	tissue (excluding vascular space) volume
L_{tis}	mL/min	Tab. 4.3	[66, 69]	tissue-specific lymph flow (see discussion for identifiability)
σ_{tis}		Tab. 4.3	[69, 71, 86]	tissue-specific reflection coefficient (see discussion for identifiability)
$\widehat{K}_{tis}$		Tab. 4.5	estimated	tissue-specific elimination-corrected partition coefficient
$CLint_{tis}$	mL/min	Tab. 4.6	estimated	tissue-specific intrinsic clearance derived from estimated extraction ratio E_{tis} (according to eq. (4.15))
$CLpla$	mL/min	Tab. 4.6	estimated	plasma clearance

4.2.3 The *simplified* PBPK model predicts plasma and tissue data in mice

Based on the estimated parameters, the simulated concentration-time profiles agree very well with the experimental data of the mAb 7E3 after an i.v. bolus administration of 8mg/kg to wild type mice, see Fig. 4.2 for tissue data and Fig. 5.1 for plasma data. The simplified PBPK model reproduces the main features of experimental plasma and tissue data profiles. i.e. the characteristic slower distribution in muscle and skin.

To evaluate the impact of residual blood on experimental tissue measurements, tissue concentrations including and excluding residual blood contribution are simulated and are shown in Fig. 4.2. For most tissues, the impact is minimal. Only little perturbations are observed. For lung, the contribution of residual blood is more pronounced. For spleen, the perturbation is substantial; almost all of the drug in spleen results from the drug in the residual blood.

For model evaluation, we used the simplified PBPK model to predict the plasma concentration of T84.66 [71], a murine IgG1 mAb targeting the carcinoembryonic antigen (CEA). T84.66 is administered to 20g control mice at 3 dose levels: 5, 10 and 25 mg/kg. To this end, tissue weights are scaled linearly with body weight to account for the difference in body weight (25g vs. 20g). As shown in Fig. 4.3, the model predicts accurately the distribution and elimination phase at all 3 dose levels—except for the last time point at 35days. This last time point, however, is most likely not reliable: a simple linear regression based on the last three time points (12, 21 and 35 days) was performed to determine the resulting half-life. We obtained half-life of 40 days (for the low dose of 5mg/kg) and 24 days (for the high dose of 25 mg/kg),

Table 4.2: *Reference tissue-dependent parameters in mice*

	V_{exp}^a	V_p	$V_{res,blo},^f$	Q
Units	mL	mL	mL / 100g tissue	mL/min
Lung	0.217^a	0.022^a	13.13	4.380^a
Adipose	1.910^b	0.011^c	-	0.307^d
Bone	1.967^a	0.091^a	-	0.170^a
Gut	3.920^a	0.114^a	1.27	0.900^a
Heart	0.151^a	0.008^a	4.81	0.280^a
Kidney	0.339^a	0.034^a	6.23	0.800^a
Liver	1.081^a	0.108^a	5.27	1.100^a
Muscle	9.005^a	0.170^a	0.63	0.800^a
Skin	3.341^a	0.227^a	0.77	1.210^a
Spleen	0.114^a	0.011^a	21.51	0.050^a
Plasma^e	0.880^a	0.880^a	-	4.380^a

[a] from [67, 69] and scaled for a mouse of 25 g body weight. Note that in [67, 69], the plasma space of each tissue is simplistically denoted as 'vascular space'. See text for more details

[b] 7% of total body weight [102] assuming a body weight of 25 g and a tissue density of 0.916 g/mL [112]

[c] total blood volume (V_{blo}) in adipose: 1 % of total volume (measured in rats but assumed to be species-independent for mammals) [103]

[d] plasma flow in adipose tissue assumed to be 7% of total plasma flow [102]

[e] plasma space not associated with any tissue (as in [67])

[f] from [113] (Table III, p. 105)

Table 4.3: *Tissue-dependent parameters for the simplified PBPK model in mice*

	$V_{res,pla}$,[a]	V_{tis},[b]	L_{tis},[c]	σ_{tis},[d]
Units	10^{-2}mL	mL	mL/min	-
Lung	1.567	0.189	0.175	0.95
Adipose	-	1.909	0.012	0.98
Bone	-	1.950	0.007	0.98
Gut	2.738	3.871	0.018	0.90
Heart	0.400	0.144	0.011	0.95
Kidney	1.160	0.318	0.032	0.95
Liver	3.132	1.024	0.022	0.90
Muscle	3.120	8.948	0.032	0.98
Skin	1.415	3.315	0.048	0.98
Spleen	1.344	0.089	0.001	0.90
Plasma	-	1.675^{e}	-	-

[a] $V_{res,pla} = (1 - hct) \cdot V_{res,blo}$ with hct = 0.45 [75]

[b] $V_{tis} = V_{exp} - V_{res,blo}$

[c] assumed to be 2 % and 4 % of plasma flow, Q, for visceral and non-visceral organs, respectively [66, 69]

[d] values assigned based on a simulation study (data not shown) [18, 69, 86]

[e] $V_p = \sum V_{p,tis}$, total plasma volume including the vascular plasma space of tissues
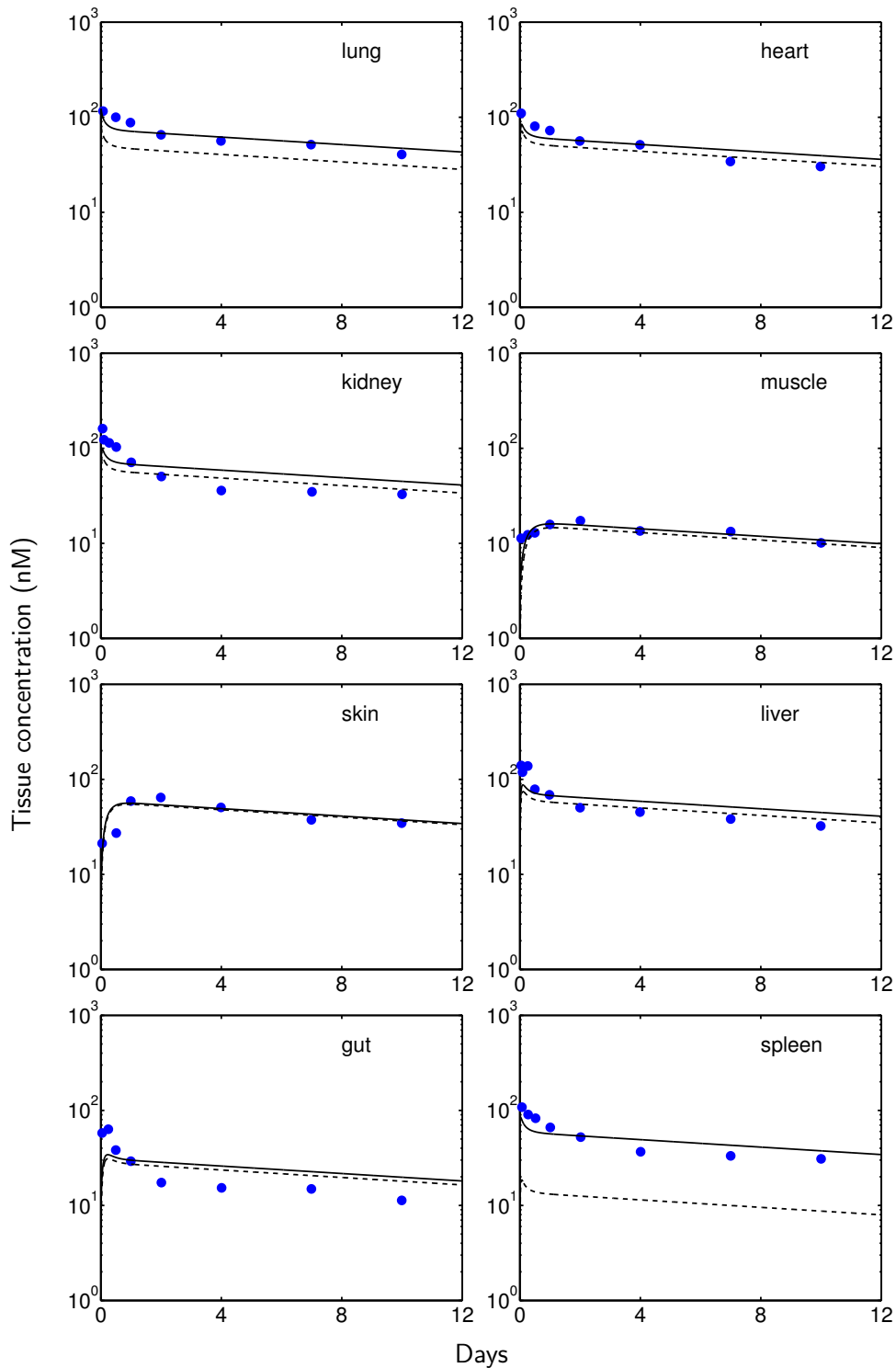
Figure 4.2: *Prediction of tissue concentration-time profiles of scenario 2 (Table 4.6) based on the simplified PBPK model (with '—' and without '- -' residual blood contamination) compared to experimentally measured concentrations in wild-type mice (blue dots) after i.v. bolus administration of 8 mg/kg 7E3 to wild-type mice. Experimental data was extracted from [69] and represent mean data. For plasma see Fig. 5.1. The predictions was indistinguishable for scenarios 3-7.*
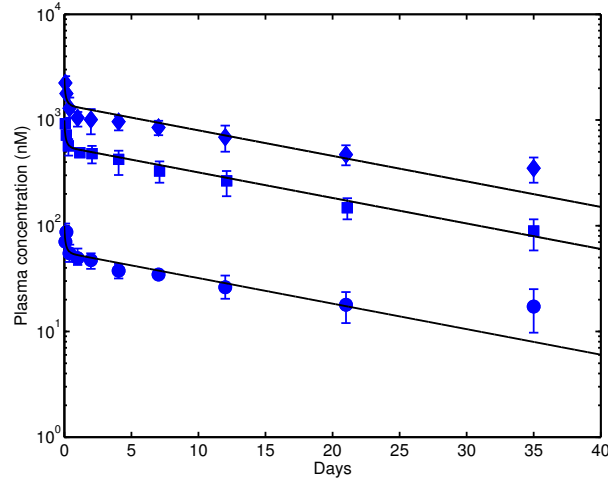
Figure 4.3: *Predictions of plasma concentration-time profiles in mice predicted by the simplified PBPK model (solid line) compared to experimental plasma concentrations in 20g nude mice for different doses of the mAb T84.66, an anti-CEA mAb: 25mg/kg (diamond), 10mg/kg (square) and 1mg/kg (circle). Experimental data was extracted from [71].*

which are in contrast to reported half-lives of 4-8 days in mice [22].

4.3 Insight into parameter estimation and identifiability

4.3.1 Tissue extraction and elimination-corrected partition coefficients

The following derivation gives key insight on the impact of distribution and elimination on tissue concentration and is important for the two-step parameter estimation process (detailed in the next section). Introducing the tissue-specific ratio

$$R_{tis} = \frac{CLint_{tis} \cdot K_{tis}}{L_{tis}}, \tag{4.10}$$

the tissue extraction ratio E_{tis} is defined via the relation

$$(1 + R_{tis}) = \frac{1}{1 - E_{tis}}. \tag{4.11}$$

Using eq. (4.10), this results in

$$E_{tis} = \frac{CLint_{tis} \cdot K_{tis}}{CLint_{tis} \cdot K_{tis} + L_{tis}}, \tag{4.12}$$

which is the common form of an extraction ratio—as it is, e.g, analogously defined for the hepatic extraction for small molecules. Based on R_{tis}, the right hand side of eq. (4.8) can also be read as

$$L_{tis} \cdot \left((1 - \sigma_{tis})C_{pla} - (1 + R_{tis})\frac{C_{tis}}{K_{tis}} \right),$$

and using eq. (4.11) this yields

$$V_{tis}\frac{d}{dt}C_{tis} = L_{tis} \cdot \left((1 - \sigma_{tis})C_{pla} - \frac{C_{tis}}{\widehat{K}_{tis}} \right), \tag{4.13}$$

which is parametrized in terms of the elimination-corrected partition coefficient

$$\widehat{K}_{tis} = (1 - E_{tis}) \cdot K_{tis}. \tag{4.14}$$

Eq. (4.14) is used in the 1st step of the parameter estimation process. We give another representation here that is equivalent to eqs. (4.8) and (4.13) and that is used in the 2nd step of the parameter estimation process. Noting that $R_{tis} = E_{tis}/(1 - E_{tis})$ and with eq. (4.10), we obtain

$$CLint_{tis} = \frac{L_{tis} \cdot R_{tis}}{K_{tis}} = \frac{L_{tis} \cdot E_{tis}}{(1 - E_{tis}) \cdot K_{tis}} = \frac{L_{tis} \cdot E_{tis}}{\widehat{K}_{tis}}. \tag{4.15}$$

From eqs. (4.13) and eq. (4.15), it results the ODE

$$\begin{aligned}
V_{tis}\frac{d}{dt}C_{tis} &= L_{tis} \cdot \left((1 - \sigma_{tis})C_{pla} - (1 - E_{tis})\frac{C_{tis}}{\widehat{K}_{tis}} \right) \\
&\quad - L_{tis}E_{tis}\frac{C_{tis}}{\widehat{K}_{tis}},
\end{aligned} \tag{4.16}$$

which is parameterized in terms of $\widehat{K}_{tis}$ and E_{tis}. Note that the second term $L_{tis} \cdot E_{tis} \cdot C_{tis}/\widehat{K}_{tis}$ equals $CLint_{tis} \cdot C_{tis}$ according to eq. (4.15).

Comparing the three *equivalent* equations (4.8), (4.13) and (4.16), we conclude that it is *not* possible to infer from typically available experimental tissue data whether some tissue is eliminating or not. All three equations predict identical tissue concentration-time profiles (for identical input C_{pla}), with eq. (4.8) being interpreted as an eliminating tissue and eq. (4.13) allowing the interpretation of a non-eliminating tissue with partition coefficient $\widehat{K}_{tis}$. This is of relevance to the present study, since the extent of elimination of mAbs in the different tissue is still under discussion.

4.3.2 Two-step parameter estimation process

Based on the venous plasma and tissue experimental data, the simplified PBPK model is used to estimate the tissue partition coefficients $\widehat{K}_{tis}$, the extraction ratios E_{tis} (used to determine $CLint_{tis}$) and CLpla following a two-step approach:

In the first step, only the elimination-corrected tissue partition coefficients $\widehat{K}_{tis}$ are estimated. This is done based on tissue data and eqs. (4.13) and (A.1), where the plasma concentration in eq. (4.13) is identical to the plasma concentration mAb$_1$ predicted by the semi-mechanistic 2-compartment model in eq. (4.17) as described below. This way, reliable plasma-concentration time profiles are enforced for the

estimation of tissue disposition. Note that the plasma concentration profile can be seen as a marker for tissue elimination. Since tissue elimination is embedded in the plasma data, it is generally not possible to estimate tissue elimination just from simple tissue data (see above section 4.3.1).

In the second step, we use the simplified PBPK model defined by eqs. (4.16) and (4.9) with $\widehat{K}_{tis}$ fixed to the values estimated in the first step. The corresponding tissue extraction ratios E_{tis} and CLpla values are estimated using plasma data and assumptions on the sites of elimination. The above procedure can be seen as an extension of the approach described in [103].

Semi-mechanistic 2-compartment model for the disposition of endogenous IgG and the mAb 7E3 in mice

A corrected version of the models published in [60] and [64] is used in the parameter estimation process. The disposition of endogenous IgG and mAb is described by a 2-compartment model with volumes V_{cen} and V_{endo}, respectively. The flow Q_{in} from the central compartment into the peripheral compartment accounts for the fluid phase endocytosis. The reverse flow Q_{out} describes the FcRn-mediated salvage mechanism of the bound species. Catabolism of the unbound species occurs in the peripheral compartment and is described by the linear clearance CL. The competitive binding of IgG_{endo} and mAb to FcRn is assumed to occur in the peripheral compartment and defines the fraction unbound fu. The rate of change of the central and peripheral concentrations of endogenous IgG and therapeutic mAb is given by the system of ODEs:

$$
\begin{aligned}
V_{cen}\frac{d}{dt}IgG_{endo,1} &= Q_{out}(1-fu)\,IgG_{endo,2} + k_{synth} \\
&\quad - Q_{in} \cdot IgG_{endo,1} \\
V_{endo}\frac{d}{dt}IgG_{endo,2} &= Q_{in} \cdot IgG_{endo,1} - CL \cdot fu \cdot IgG_{endo,2} \\
&\quad - Q_{out}(1-fu) \cdot IgG_{endo,2} \\
V_{cen}\frac{d}{dt}mAb_1 &= Q_{out}(1-fu)\,mAb_2 \\
&\quad - Q_{in} \cdot mAb_1 \\
V_{endo}\frac{d}{dt}mAb_2 &= Q_{in} \cdot mAb_1 - CL \cdot fu \cdot mAb_2 \\
&\quad - Q_{out}(1-fu) \cdot mAb_2
\end{aligned}
\tag{4.17}
$$

with fu defined in eq. (3.8); $FcRn_u$ defined in eq. (3.7); and $FcRn_{eff} = FcRn - [IgG_{endo,2}+mAb_2]-K_D$. This corrected version of the 2-compartment model proposed in [60] is simultaneously fitted to plasma data of 7E3 in WT and FcRn-KO mice after an i.v. bolus administration of 0.2mg (i.e., 8mg/kg for a 25g mouse) and to the plasma steady-state concentration of endogenous IgG in WT mice. The parameter

Table 4.4: *Parameter estimates of the semi-mechanistic 2-compartment model, describing the plasma concentrations of 7E3 and the steady state plasma concentrations of IgGendo*

	V_{cen}	V_{endo}	Q_{in}	Q_{out}	CL	k_{synth}	$FcRn_{\text{tot}}$	K_{D}
	mL	mL	mL/d	mL/d	mL/d	nmol/d	nM	nM
cen	1.600		1.597			1.849		
endo		0.088		0.102	0.043		2.22e+5	4.8

values of the model are summarized in Table 4.4. The initial conditions (in mg/ml) are $\text{IgG}_{\text{endo,1}} = 2.29$, $\text{IgG}_{\text{endo,2}} = 39.7$, $\text{mAb}_1 = \text{dose}/V_{\text{cen}} = 0.125$ and $\text{mAb}_2 = 0$.

4.3.3 Parameter identifiability

Link elimination-corrected tissue partition coefficients $\widehat{\text{K}}_{\text{tis}}$ ***to reported antibody biodistribution coefficients*** ABC_{exp}

In [18], antibody biodistribution coefficients (ABCs) relating tissue to plasma concentrations were analyzed for a variety of non-binding mAbs and species (i.e., the species do not express a target for the mAb). The authors found a linear relationship between 'tissue' and plasma concentrations. Their analysis is based on a variety of different studies so that estimated ABC values can be expected to be perturbed by residual blood (in line with their comment [18, p.302]). Thus, we denote by ABC_{exp} the residual blood-contaminated antibody biodistribution coefficients, i.e.,

$$\text{ABC}_{\text{exp}} = \frac{\text{C}_{\text{exp}}}{\text{C}_{\text{pla}}}.$$

ABC_{exp} are corrected for residual blood to determine the 'pure' steady-state antibody biodistribution coefficients ABC_{tis}. Dividing eq. (A.1) by C_{pla} yields

$$\text{ABC}_{\text{exp}} = \frac{\text{V}_{\text{tis}}}{\text{V}_{\text{exp}}} \frac{\text{C}_{\text{tis}}}{\text{C}_{\text{pla}}} + \frac{\text{V}_{\text{res,pla}}}{\text{V}_{\text{exp}}}. \tag{4.18}$$

Solving for $\text{C}_{\text{tis}}/\text{C}_{\text{pla}}$ and using the definition of res_{blo}, it follows the relation between estimated ABC_{exp} in [18] and ABC_{tis} as

$$\text{ABC}_{\text{tis}} = \frac{\text{ABC}_{\text{exp}} - (1 - \text{hct})\text{res}_{\text{blo}}}{1 - \text{res}_{\text{blo}}}. \tag{4.19}$$

At steady-state, it is $d\text{C}_{\text{tis,ss}}/dt = 0$ so that from eq. (4.13) it follows $\text{L}_{\text{tis}}((1 - \sigma_{\text{tis}})\text{C}_{\text{pla,ss}} - \text{C}_{\text{tis,ss}}/\widehat{\text{K}}_{\text{tis}}) = 0$. Thus, ABC_{tis} is also defined as

$$\text{ABC}_{\text{tis}} = \frac{\text{C}_{\text{tis,ss}}}{\text{C}_{\text{pla,ss}}} = (1 - \sigma_{\text{tis}}) \cdot \widehat{\text{K}}_{\text{tis}}. \tag{4.20}$$

Table 4.5: *Estimated elimination-corrected tissue partition coefficients $\widehat{K}_{tis}$ and resulting antibody biodistribution coefficients ABC_{tis} according to eq. (4.20) (excluding residual blood) and ABC_{exp} values according to eq. (4.18) (including residual blood contribution). The difference between ABC_{tis} and ABC_{exp} is largest for spleen and lung*

	$\widehat{K}_{tis}$	ABC_{tis}	ABC_{exp}
Adipose	1.695	0.034	0.034
Bone	1.695	0.034	0.038
Gut	0.623	0.062	0.068
Heart	2.322	0.116	0.137
Kidney	2.576	0.129	0.155
Liver	1.324	0.132	0.154
Lung	2.152	0.108	0.166
Muscle	1.695	0.034	0.037
Skin	6.270	0.125	0.129
Spleen	0.303	0.030	0.142

Exploiting eq. (4.20), thus, the elimination-corrected tissue-to-plasma partition coefficients are directly derived from experimentally determined ABC_{exp} values:

$$\widehat{K}_{tis} = \frac{ABC_{exp} - (1 - hct)res_{blo}}{(1 - \sigma_{tis})(1 - res_{blo})}. \tag{4.21}$$

Estimating tissue partition coefficients

As described in section 4.3.2, unknown parameters of the simplified PBPK model are estimated with a two-step approach based on plasma and tissue data of the mAb 7E3. The estimated parameters for $\widehat{K}_{tis}$ together with the resulting antibody biodistribution coefficients ABC_{tis} derived from eqs. (4.19) and (4.21) are reported in Table 4.5. Our resulting ABC_{tis} values are consistent with the values reported in [18]—with differences being due to residual blood contamination (described in appendix A.5) and the fact that the values in [18] have been estimated across various species. Since in [18], ABC_{exp} values are shown to be approximately constant for different pre-clinical species and human, we may use relation (4.21) to also determine $\widehat{K}_{tis}$ values for these species, i.e., rat, monkey and human.

Estimating total plasma clearance

There are no consistent reports to discriminate the tissues involved in mAbs elimination. Several authors report that adipose, kidney, liver, muscle, skin and spleen are involved in IgGs catabolism [78, 114, 115]. As a consequence, herein different scenarios of tissue elimination are considered and studied.

Table 4.6: *Estimated tissue extraction ratios and plasma clearance for scenarios (sc.) 2-7 (see text for details). Compartments, where no elimination was assumed are indicated by '-'. Of note, the resulting total clearance defined in eq. (4.22) (in mL/min) is constant across the different scenarios.*

Scenario	sc. 2	sc. 3	sc. 4	sc. 5	sc. 6	sc. 7
E_{adi}	0.029	-	-	-	-	-
E_{bon}	-	-	-	-	-	-
E_{gut}	-	-	-	-	-	-
E_{hea}	-	-	-	-	-	-
E_{kid}	<1e-8	-	-	-	-	-
E_{liv}	0.029	-	-	-	0.042	-
E_{lun}	-	-	-	-	-	-
E_{mus}	0.029	-	-	0.14	-	-
E_{ski}	<1e-8	-	0.095	-	-	-
E_{spl}	0.029	0.92	-	-	-	-
CLpla	-	-	-	-	-	9e-5
CL_{tot}	9e-5	9e-5	9e-5	9e-5	9e-5	9e-5

In a first scenario, all tissues are eliminating. The estimated E_{tis} are sensitive to the initial values (therefore, their estimated values are not reported). Interestingly, even though the E_{tis} values are differing from one fit to another, the total clearance CL_{tot} remains practically constant. Here, the total clearance is defined as

$$CL_{tot} = \sum_{tis \neq pla} E_{tis} \cdot L_{tis}(1 - \sigma_{tis}) + CLpla. \qquad (4.22)$$

The second scenario assumes that the tissue elimination is linked to FcRn expression levels, which were studied in different tissues of C57BL/6 control mice in [78, Fig. 4, p. 1295]. Notable FcRn expression levels are only identified in adipose, muscle, liver, kidney, skin, and spleen. It appears that FcRn expression levels are similar and high in kidney and skin, while being similar and low in adipose, liver, muscle and spleen. Two groups of tissues are therefore defined: {kidney, skin} and {adipose, liver, muscle, spleen}. An identical extraction ratio is assigned to each group and estimated, while the extraction of the remaining tissues and the plasma clearance is set to 0. The estimated E_{tis} for kidney and skin is close to 0 suggesting that no extraction in these two tissues occurred (consistent with the high expression of protecting FcRn). This result is surprising and is not in accordance with [78, 114, 115].

In the scenarios 3-6, only one eliminating tissue is considered, exemplified for skin, muscle, liver and spleen. Scenario 7 assumes that all elimination processes take place in the plasma compartment. The estimated extracting ratios and the plasma clearance for all scenarios as well as the corresponding total clearance CL_{tot}

are reported in Table 4.6. Surprisingly, for all scenarios, CL_{tot} remains unchanged. These results suggest that, given the mice plasma and tissue data, the individual E_{tis} cannot be estimated and that it is not possible to determine which tissues are involved in the elimination of mAbs.

These findings apply analogously to the more complex models (see Chapter 3 (secs. 3.1 and 3.3) and Appendix A (apps A.3 and A.4)), from which the simplified PBPK model is derived.

4.4 Discussion

The simplified PBPK model (i) includes explicitly or implicitly the physiological processes relevant to describe mAbs disposition; (ii) is parameterized by a minimum number of parameters to allow stable parameter estimation; and (iii) allows reproducing typically observed characteristics of concentration-time profiles in plasma and tissues. A key step to substantially reduce the complexity in comparison to published PBPK models [69–71, 73] is to implicitly consider the endosomal space and the FcRn-mediated salvage mechanism. Analogous model reduction approaches have been successfully used for small molecule drugs, e.g., when considering the interaction of moderate to strong bases with intra-cellular acidic phospholipids without modeling explicitly diffusion across the cell membrane and binding kinetics to the acidic phospholipids [116].

The simplified PBPK model for mAb disposition is a whole-body model with extravasation rate-limited tissue distribution and elimination potentially occurring from various tissues and plasma. The tissue model for mAbs presents analogies with the permeability rate-limited tissue model for small molecule drugs, with one marked difference: In the permeability rate-limited tissue model, the inflow is typically limited by the low permeability across the cellular membrane which also limits the outflow, respectively defined as $Q_{inflow} = P \cdot SA$ and $Q_{outflow} = Q_{inflow}/K_{tis}$, where P denotes the drug permeability, SA the surface area of the tissue and K_{tis} some tissue partition coefficient. The (intra-cellular) tissue response time for permeability rate-limited tissues, given by $\tau = \log(2) \cdot V_{tis} \cdot K_{tis}/Q_{inflow}$, is usually long. In the extravasation rate-limited tissue model, it is $Q_{inflow} = (1 - \sigma) \cdot L$ and $Q_{outflow} = Q_{in}/ABC_{tis}$, with ABC_{tis} the antibody biodistribution coefficient. The inflow is slow due to the small size of pores in the vascular wall which restricts the extravasation. The outflow, however, is almost one order of magnitude faster due to the larger pore size of lymphatic vessels. Consequently, it results in moderate tissue response time $\tau = \log(2) \cdot V_{tis} \cdot ABC_{tis}/Q_{inflow}$. We notice that even if the inflows in both tissue models would be identical, i.e, $P \cdot SA = (1 - \sigma) \cdot L$, it would take much longer for

the SMD to reach its (quasi) steady state than for the mAb, since usually $K_{tis} \gg 1$, while $ABC_{tis} < 1/5$ (Table 4.5, [18]).

From common experimental data (only plasma, or plasma and tissue data) it is not possible to infer, which tissues are involved into the unspecific elimination. This also holds true for small molecule drugs, where, however, assumptions on which tissues are eliminating (typically liver and/or kidney) are commonly supported by *in vitro* assay (hepatocytes, microsomes) or additional experimental data (urine). Without such additional information, the location and extent of mAb elimination remains to be elucidated. For monoclonal antibodies, this ambiguity is reflected in the different assumptions made in published PBPK models about where and how to account for elimination [67–70] and is here further illustrated by the different elimination scenarios (sc. 1-7) in section 4.3.3, Table 4.6. The ambiguity is also reflected at the level of the ODEs describing the rate of change of tissue concentrations: compare eqs. (4.8) and (4.13). The argument is not restricted to the simplified PBPK model but holds also true for the more complex PBPK models.

Since tissue-to-plasma partition coefficients are small, contamination of tissue samples by residual blood/plasma content can have a large impact on reported tissue concentrations. In [113], residual blood volumes of the harvested organs in mice are reported. As can be inferred from Fig. 4.2, residual plasma contamination has an impact for spleen and lung, unless the other tissues, where the impact is only minor. These findings have to be read in the light of the methodology used in [113] to measure the residual blood volume which is base on 51Cr-labeled red blood cell uptake method [117]. As spleen is the organ of production and storage of red blood cells, the assessment of residual blood volume might be biased. Measurement of residual blood has been proven of importance to determine the extent of tissue partitioning for small molecule drugs [118, 119]. In [120], the authors conclude that correction for the residual blood is necessary when tissue-to-blood partition coefficients are very small and when the volume fraction of the blood in tissue is substantial as for lung.

In [41], PBPK models for mAb disposition are reviewed. A surprising 200-fold range of lymph flow values used in published PBPK models for the same tissue was observed. With the parameterization of the simplified PBPK model, this observation can be understood. Given some positive parameter α, the rate of change of the tissue concentration in eq. (4.8) can be *equivalently* expressed as

$$V_{tis} \frac{d}{dt} C_{tis} = \widetilde{L}_{tis} \cdot \left((1 - \widetilde{\sigma}_{tis}) C_{pla} - \frac{C_{tis}}{\widetilde{K}_{tis}} \right) - CLint_{tis} \cdot C_{tis}$$

with $\widetilde{L}_{tis} = \alpha L_{tis}$; $(1 - \widetilde{\sigma}_{tis}) = (1 - \sigma_{tis})/\alpha$ and $\widetilde{K}_{tis} = \alpha K_{tis}$. Varying α between 1-200 would explain the observed range of values for lymph flows in [41]. It also highlights the fact that reported values of σ_{tis} and K_{tis} are relative to the lymph flow values, which are commonly assumed to be 2% or 4% of plasma flow (see Table 4.3). As expected, steady-state partitioning is not influenced, since α cancels out in eq. (4.20).

The simplest way to parameterize the simplified PBPK model is based on eqs. (4.8)-(4.9) with species-dependent parameters given in Table 4.3, plasma clearance CLpla given in Table 4.6 (sc. 7) and $E_{tis} = CLint_{tis} = 0$ for all tissues. Due to eq. (4.14), the partition coefficients fulfill $K_{tis} = \widehat{K}_{tis}$ and can therefore be taken from Table 4.5. For extrapolation of the simplified PBPK model to other species/strains, one can make use of the ABC_{tis} values (see Table 4.5, assumed to be species-independent in [18]) by exploiting the relationship in eq. (4.20). Then, only the physiological data (often readily available from literature) and the plasma clearance CLpla are missing. In addition, the simplified PBPK can be used to "extrapolate" to FcRn knockout mice by simply increasing the plasma clearance (by a factor of 23), thereby accounting for the loss in protection from degradation. The partition coefficients, as was already remarked in [18], are comparable for wild type and FcRn-knockout mice.

Lumping Approach and derivation of Classical Compartment Models for mAbs

In their review, Keizer et al. [3] report on clinical pharmacokinetic studies of 27 commercialized mAbs. In most of the cases, the PK of mAbs is described by a classical 2-compartment disposition model. The central and peripheral compartments are typically associated with the plasma and the interstitial space, respectively. Modeling the processes involved in the elimination of mAbs is quite diverse: it includes linear [92] and/or non-linear [93, 94] clearance(s) from the central compartment, or parallel linear and non-linear clearances from the central and/or peripheral compartment(s) [95, 96]. The non-linearity in the PK is mainly attributed to the saturable binding to the target which is not integrated at this stage in the simplified PBPK model (see Chapter 6 for extension to a membrane-bound target).

In this chapter, the aim is to determine which low-dimensional compartment model structures are consistent with the simplified PBPK model accounting for the linear non-specific clearance. To this end, the lumping approach presented in [91] is extended to account for peripheral elimination.

5.1 Extended lumping approach: Mechanistic derivation of simple compartment models

We first define the lumping criterion specific to the parameterization of the simplified PBPK model and derive lumped parameters based on the extension of the lumping approach previously developed for PBPK models for SMDs [91] to eliminating tissues for mAbs. We secondly theoretically draw the general ODEs of lumped models, representing the foundations for later link and interpretation of classical compartment models.

5.1.1 Lumped parameters

The steady-state antibody biodistribution coefficient, $\mathrm{ABC_{tis}}$, is determined from steady state conditions for tissue concentrations (eq. (4.20), in section 4.3.3). It is

$$\mathrm{ABC_{tis}} = \frac{\mathrm{C_{tis,ss}}}{\mathrm{C_{pla,ss}}} = (1 - \sigma_{\mathrm{tis}}) \cdot \widehat{\mathrm{K}}_{\mathrm{tis}}.$$
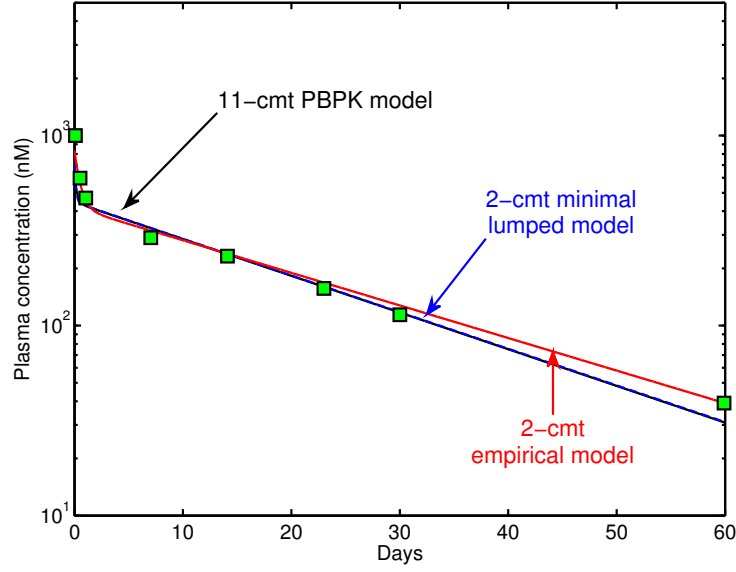
Figure 5.1: *Predictions in comparison to the in vivo plasma data for an i.v. bolus administration of 8 mg/kg 7E3 in wild-type mice (exp. data extracted from [69, Fig. 3, p.699]). Plasma concentration-time profiles of scenario 2 (Table 4.6) are based on the simplified PBPK model ('11-cmt PBPK model'), the minimal lumped 2-compartment model ('2-cmt minimal lumped model') and the semi-mechanistic 2-compartment model ('2-cmt empirical model'). The predictions of the simplified PBPK model based on clearance scenario 2 are indistinguishable from scenarios 3-7.*

In accordance with the above equation, for plasma, we formally set $\widehat{K}_{pla} = 1/(1 - \sigma_{pla})$ and $ABC_{pla} = 1$. Rearranging eq. (4.20) to

$$\widehat{K}_{tis} = \frac{C_{tis,ss}}{(1 - \sigma_{tis})C_{pla,ss}},$$

$\widehat{K}_{tis}$ can be interpreted as the elimination corrected tissue-to-accessible plasma partition coefficient and, based on eq. (4.14), K_{tis} as the tissue-to-accessible plasma partition coefficient (comparable to tissue-to-unbound plasma partition coefficients for small molecule drugs).

According to the lumping criterion [91, eq.(20)], tissues $tis_1, \ldots, tis_k$ are grouped together to form a lumped compartment $L = \{tis_1, \ldots, tis_k\}$, if the normalized tissue concentration-time profiles coincide, i.e, if

$$\frac{C_{tis_1}(t)}{(1 - \sigma_{tis_1}) \cdot \widehat{K}_{tis_1}} = \ldots = \frac{C_{tis_k}(t)}{(1 - \sigma_{tis_k}) \cdot \widehat{K}_{tis_k}} \tag{5.1}$$

for $t \geq 0$. For later reference, the central compartment is defined as the lumped compartment containing plasma. Below, the lumped model parameters are determined as in [91]. The lumped tissue volume V_L is defined as

$$V_L = \sum_{tis \in L} V_{tis},$$

where here and below, tis $\in$ L means that the sum is taken over all tissues that are lumped together into L. For all non-central compartments, the lumped lymph flow L_L and the lumped reflection coefficient σ_L are defined by

$$L_L = \sum_{tis \in L} L_{tis}; \quad L_L \cdot (1 - \sigma_L) = \sum_{tis \in L} L_{tis} \cdot (1 - \sigma_{tis}),$$

while for the central compartment, the central lymph flow and reflection coefficient are

$$L_{cen} = \sum_L L_L; \quad L_{cen} \cdot (1 - \sigma_{cen}) = \sum_L L_L \cdot (1 - \sigma_L), \tag{5.2}$$

where in the above equations, the sum is taken over all non-central lumped compartments (in case there are any; otherwise L_{cen} and σ_{cen} are neither defined nor needed). The concentration C_L of the lumped compartment is defined by

$$V_L \cdot C_L = \sum_{tis \in L} V_{tis} \cdot C_{tis}, \tag{5.3}$$

resulting in the definition of the lumped tissue partition coefficient $\widehat{K}_L$ according to

$$V_L \cdot (1 - \sigma_L) \cdot \widehat{K}_L = \sum_{tis \in L} V_{tis} \cdot (1 - \sigma_{tis}) \cdot \widehat{K}_{tis}. \tag{5.4}$$

We remark that the above equation can also be formulated in terms of ABC values, with $V_L \cdot ABC_L = \sum_{tis \in L} V_{tis} \cdot ABC_{tis}$. To extend the lumping approach to eliminating tissues, the lumped extraction ratio E_L is defined by

$$E_L \cdot L_L \cdot (1 - \sigma_L) = \sum E_{tis} \cdot L_{tis} \cdot (1 - \sigma_{tis}),$$

where the sum is taken over all tis $\in$ L for non-central compartments L, while it is taken over all tis $\in$ cen, tis $\neq$ pla for the central compartment. Using E_L, the lumped partition coefficient K_L is determined from the elimination corrected partition coefficient $\widehat{K}_L$ analogously to eq. (4.14) by

$$\widehat{K}_L = (1 - E_L) \cdot K_L.$$

For all non-central compartments, the lumped intrinsic clearance $CLint_L$ is defined analogously to eq. (4.15) as

$$CLint_L = \frac{E_L \cdot L_L}{(1 - E_L) \cdot K_L} = \frac{E_L \cdot L_L}{\widehat{K}_L}.$$

Finally, for the central compartment, the lumped central clearance CL_{cen} is defined by

$$CL_{cen} = E_{cen} \cdot L_{cen} \cdot (1 - \sigma_{cen}) + CLpla. \tag{5.5}$$

5.1.2 Equations of lumped models

The ODE describing the rate of change of the lumped concentrations C_L is characterized based on eq. (5.3) with $L = \{tis_1, \ldots, tis_k\}$. To this end, the relation is first established between the lumped concentration C_L and some tissue concentrations C_{tis} with $tis \in L$. Starting from eq. (5.3), it is

$$
\begin{aligned}
V_L \cdot C_L &= \sum_{i=1}^{k} V_{tis_i} \cdot C_{tis_i} \\
&= \sum_{i=1}^{k} \left(V_{tis_i}(1 - \sigma_{tis_i})\widehat{K}_{tis_i} \cdot \frac{C_{tis_i}}{(1 - \sigma_{tis_i})\widehat{K}_{tis_i}} \right) \\
&= \left(\sum_{i=1}^{k} V_{tis_i}(1 - \sigma_{tis_i})\widehat{K}_{tis_i} \right) \cdot \frac{C_{tis}}{(1 - \sigma_{tis})\widehat{K}_{tis}} \\
&= V_L(1 - \sigma_L)\widehat{K}_L \cdot \frac{C_{tis}}{(1 - \sigma_{tis})\widehat{K}_{tis}},
\end{aligned}
$$

where the third line is derived from the lumping criterion $C_{tis}/((1 - \sigma_{tis}) \cdot \widehat{K}_{tis}) = C_{tis_i}/((1 - \sigma_{tis_i}) \cdot \widehat{K}_{tis_i})$ for $tis \in L$ and $i = 1, \ldots, k$, while the last line is based on eq. (7.16). Rearranging the last equation yields

$$
C_{tis} = (1 - \sigma_{tis})\widehat{K}_{tis} \cdot \frac{C_L}{(1 - \sigma_L)\widehat{K}_L}. \tag{5.6}
$$

For the plasma compartment, this specifically reads

$$
C_{pla} = \frac{C_{cen}}{(1 - \sigma_{cen})\widehat{K}_{cen}}. \tag{5.7}
$$

For all compartments except for the central compartment, we obtain

$$
\begin{aligned}
V_L \frac{d}{dt} C_L &= \sum_{tis \in L} L_{tis} \cdot \left((1 - \sigma_{tis})C_{pla} - \frac{C_{tis}}{\widehat{K}_{tis}} \right) \\
&= \sum_{tis \in L} L_{tis}(1 - \sigma_{tis}) \cdot \left(C_{pla} - \frac{C_{tis}}{(1 - \sigma_{tis})\widehat{K}_{tis}} \right) \\
&= \sum_{tis \in L} L_{tis}(1 - \sigma_{tis}) \cdot \left(C_{pla} - \frac{C_L}{(1 - \sigma_L)\widehat{K}_L} \right) \\
&= L_L(1 - \sigma_L) \cdot \left(C_{pla} - \frac{C_L}{(1 - \sigma_L)\widehat{K}_L} \right),
\end{aligned}
$$

where we exploit eq. (5.6) in the third line. Thus

$$
\begin{aligned}
V_L \frac{d}{dt} C_L &= L_L \cdot \left((1 - \sigma_L)C_{pla} - \frac{C_L}{\widehat{K}_L} \right) \\
&= L_L \cdot \left((1 - \sigma_L)C_{pla} - \frac{C_L}{K_L} \right) - CLint_L \cdot C_L.
\end{aligned}
$$

For the central compartment, based on eqs. (5.2) and (5.5), it results

$$
\begin{aligned}
V_{cen}\frac{d}{dt}C_{cen} &= \sum_{tis} L_{tis} \cdot \left(\frac{C_{tis}}{K_{tis}} - (1 - \sigma_{tis})C_{pla} \right) + \ldots \\
&\quad \sum_{tis \in cen} L_{tis} \cdot \left((1 - \sigma_{tis})C_{pla} - \frac{C_{tis}}{\widehat{K}_{tis}} \right) \\
&= \sum_{tis \notin cen} L_{tis}(1 - \sigma_{tis}) \cdot \left(\frac{C_{tis}}{(1 - \sigma_{tis})K_{tis}} - C_{pla} \right) + \ldots \\
&\quad \sum_{tis \in cen} L_{tis} \cdot \left(\frac{C_{tis}}{\widehat{K}_{tis}} - (1 - \sigma_{tis})C_{pla} \right) - \ldots \\
&\quad E_{tis}L_{tis}\frac{C_{tis}}{\widehat{K}_{tis}} - \sum_{tis \in cen} L_{tis} \cdot \left(\frac{C_{tis}}{\widehat{K}_{tis}} - (1 - \sigma_{tis})C_{pla} \right) \\
&= \sum_{L} L_{L}(1 - \sigma_{L}) \cdot \left(\frac{C_{L}}{(1 - \sigma_{L})\widehat{K}_{L}} - C_{pla} \right) \ldots \\
&\quad E_{cen}L_{cen}(1 - \sigma_{cen})C_{pla} \\
&= \sum_{L} L_{L} \cdot \left(\frac{C_{L}}{\widehat{K}_{L}} - (1 - \sigma_{L})C_{pla} \right) - CLpla_{cen} \cdot C_{pla} \\
&= L_{cen} \cdot \left(C_{in,L} - (1 - \sigma_{cen})C_{pla} \right) - CLpla_{cen} \cdot C_{pla}.
\end{aligned}
$$

The inflowing concentration into the central compartment is defined as

$$
L_{cen} \cdot C_{in} = \sum_{L} L_{L} \cdot \frac{C_{L}}{K_{L}}.
$$

These equations and relationships are the foundation for the derivation of lumped compartment models developed below.

5.2 Lumped models and their link to classical compartment models

Here we focus on establishing the link between 2-compartment lumped models, directly derived from the simplified PBPK model, and the most commonly used classical 2-compartment models. The equations for 1- or 3-compartment models can be derived analogously.

5.2.1 Derivation of classical compartment models

With the lumped peripheral compartment denoted by 'per', the rate of change of the central and peripheral lumped compartment concentrations C_{cen} and C_{per} are given by

$$
\begin{aligned}
V_{cen}\frac{d}{dt}C_{cen} &= L \cdot \left(\frac{C_{per}}{K_{per}} - (1-\sigma_{per})C_{pla}\right) \\
&\quad -CL_{cen} \cdot C_{pla} \\
V_{per}\frac{d}{dt}C_{per} &= L \cdot \left((1-\sigma_{per})C_{pla} - \frac{C_{per}}{K_{per}}\right) \\
&\quad -CLint_{per} \cdot C_{per}
\end{aligned}
$$

with initial conditions $C_{cen}(0) = dose/V_{cen}$ and $C_{per}(0) = 0$. The plasma concentration C_{pla} is linked to the central concentration as defined in eq. (5.7). This lumped model is parameterized in terms of *physiological* parameters: volume of central and peripheral compartments V_{cen} and V_{per}; lumped peripheral lymph flow $L = L_{per}$; peripheral reflection coefficient σ_{per}; central plasma clearance CL_{cen} and peripheral intrinsic clearance $CLint_{per}$.

To establish the link to classical two compartment models, the above lumped model is alternatively parameterized in terms of *apparent* parameters: central and peripheral volumes of distribution V_1 and V_2; central plasma clearance CL_1 and peripheral intrinsic clearance CL_2; and inter-compartment clearance Q. For this parameterization, the rates of change of the plasma and peripheral concentrations C_1 and C_2 are defined by the ODEs

$$
\begin{aligned}
V_1\frac{d}{dt}C_1 &= Q(C_2 - C_1) - CL_1 \cdot C_1 \\
V_2\frac{d}{dt}C_2 &= Q(C_1 - C_2) - CL_2 \cdot C_2
\end{aligned}
$$

with $C_1(0) = dose/V_1$ and $C_2(0) = 0$ for an i.v. bolus administration. This results in the following relationships between the apparent and physiological parameters:

$$
\begin{aligned}
V_1 &= V_{cen} \cdot ABC_{cen} \\
V_2 &= V_{per} \cdot ABC_{per}/(1 - E_{per}) \\
Q &= L \cdot (1 - \sigma_{per}) \\
CL_1 &= CL_{cen} \\
CL_2 &= CLint_{per} \cdot ABC_{per}/(1 - E_{per}) \\
C_1 &= \frac{C_{cen}}{ABC_{cen}} \\
C_2 &= \frac{C_{per}}{ABC_{per}/(1 - E_{per})}
\end{aligned}
$$

Table 5.1: *Comparison of parameter values corresponding to three minimal lumped 2-compartment models (MLMs).*

Parameter	$\mathrm{MLM_{cen,per}}$	$\mathrm{MLM_{cen}}$	$\mathrm{MLM_{per}}$
$\mathrm{V_{cen}}$ (mL)	3.4	3.4	3.4
$\mathrm{V_{per}}$(mL)	20.0	20.0	20.0
L(mL/d)	5.5	5.5	5.5
$\mathrm{CL_{cen}}$(mL/d)	0.10	0.13	-
$\mathrm{CLint_{per}}$(mL/d)	0.67	-	2.4
$\mathrm{K_{cen}}$	1.2	1.2	1.1
$\mathrm{K_{per}}$	1.7	1.7	1.7

with $\mathrm{ABC_{cen}} = (1 - \sigma_{cen})\widehat{\mathrm{K}}_{cen}$ and $\mathrm{ABC_{per}} = (1 - \sigma_{per})\widehat{\mathrm{K}}_{per}$. The additional factor $(1 - \mathrm{E_{per}})$ in the relationships for the peripheral parameters accounts for peripheral elimination.

If some elimination is assumed to occur only from the central compartment, then $\mathrm{CLint_{per}} = 0$ and the relationships between physiological and apparent parameters of the central and peripheral compartments become comparable: $\mathrm{V_1} = \mathrm{V_{cen}} \cdot \mathrm{ABC_{cen}}$; $\mathrm{V_2} = \mathrm{V_{per}} \cdot \mathrm{ABC_{per}}$; $\mathrm{C_1} = \mathrm{C_{cen}}/\mathrm{ABC_{cen}}$ and $\mathrm{C_2} = \mathrm{C_{per}}/\mathrm{ABC_{per}}$.

5.2.2 Mechanistic and physiological interpretation of classical compartment models

The dimensionality of the simplified PBPK model is reduced based on the extension of the lumping approach detailed in paragraph 5.1. The normalized concentration-time profiles of all plasma and tissue compartments, defined in eq. (5.1) are represented in Fig. 5.2. Four groups of kinetically similar tissues are identified: cen={plasma, lung}, $\mathrm{L_1}$={heart, kidney, liver, spleen}, $\mathrm{L_2}$={gut} and $\mathrm{L_3}$={adipose, bone, muscle, skin}. These would be the basis for mechanistically lumped models that aim at predicting the concentration-time profiles of *all* tissues. Here, however, we are only interested in the minimal lumped model that aims at predicting only the *plasma* concentration-time profile. This is achieved by further reducing the number of tissue groups. Motivated by the biphasic characteristics of the plasma-concentration time profile, we study different options of grouping all tissues into a central (cen) and peripheral (per) compartment.

In the first minimal lumped model, cen = {plasma,lung} and the peripheral compartment contains all remaining tissues. In the second minimal lumped model, per={adipose, bone, gut, muscle, skin} and the central compartment contains all remaining tissues. Depending on which tissues are assumed to be eliminating, there
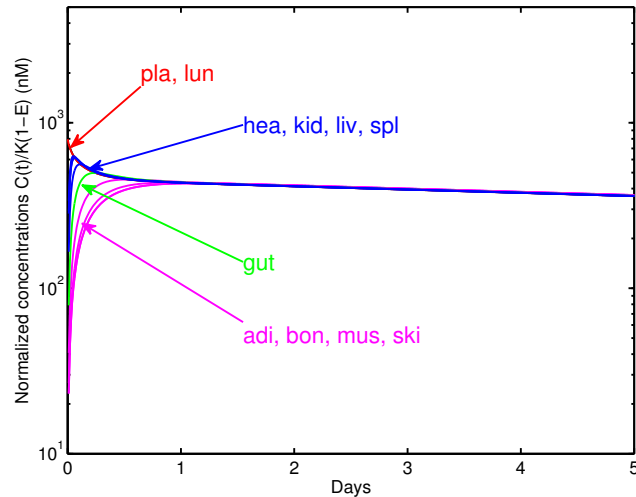
Figure 5.2: *Identification of groups of tissues with similar normalized concentration-time profiles, as predicted by the simplified PBPK model after an i.v. bolus administration of 8 mg/kg 7E3 to wild-type mice. Similar concentration-time profiles are indicated by identical color.*

are three different scenarios regarding where to assign clearance processes (see Fig. 5.3): (i) from the central and peripheral compartments, (ii) from the central compartment only; or (iii) from the peripheral compartment only. Each of these three clearance scenarios could be combined with the different choices of the tissues constituting the central and peripheral compartments.
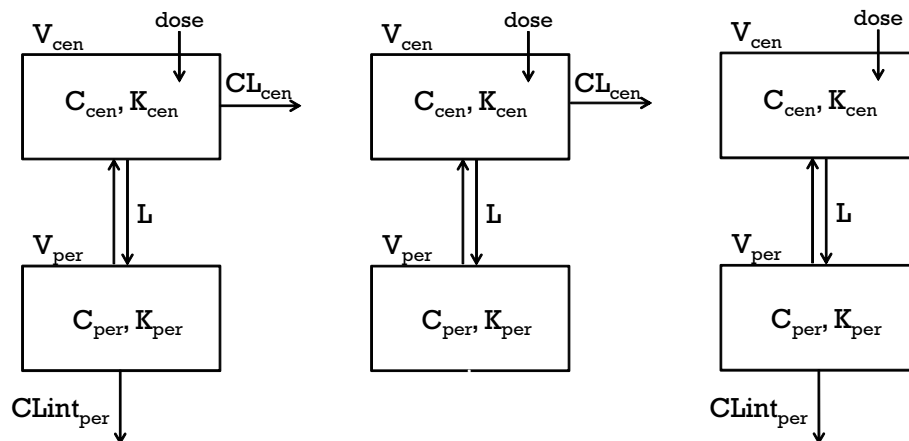
Figure 5.3: *Structure of different minimal lumped models that all describe the experimental plasma concentration-time profiles (7E3, in mice) equally well.*

For the choice of per={adipose, bone, gut, muscle, skin} and the central compartment containing all the remaining tissues, the parameter values of the resulting minimal lumped compartment models are given in Tab. 5.1. Figure 5.1 shows the experimental plasma data in comparison to the predictions of the simplified PBPK

model, the minimal lumped 2-compartment model, and the semi-mechanistic 2-compartment model. Predictions for the simplified PBPK and minimal lumped models are based on the clearance scenario 2. Parameterizations based on other clearance scenarios resulted in indistinguishable predictions. All models were in very good agreement with the experimental data (and differ only slightly, e.g., in the terminal phase).

5.3 Discussion

To inform the development and interpretation of classical compartment models, we identify which simple compartment model structures are consistent with the simplified PBPK model. Such an approach has several advantages: (i) the lumping approach links the mechanistic interpretation of a PBPK model to the classical compartment models and thereby suggests possible interpretations; (ii) the model reduction process links the two levels of description and shows that the two approaches are not so different; (iii) if one is interested in parameter estimation for a PBPK model, lumping might provide a means to stabilize the estimation process; (iv) a mismatch between a minimal lumped model arising from a PBPK model and a classical compartment model suggests that some processes are not appropriately described, either in the PBPK model or in the classical compartment model, or in both; (v) the reduction processes offer a systematic means to derive covariate relationship for classical compartment models based on the integration of the covariate in the PBPK model. This is usually much simpler due to the mechanistic interpretation of parameters in a PBPK model (see [121] for full details).

The derivation of lumped models, based on the experimental data in mice, outlines that several definitions of the central compartment are consistent with the data (see section 5.2.2). The central compartment could comprise only plasma and lung or, e.g., it could comprise all tissues except for adipose, muscle, gut, bone, and skin. Other scenarios are possible.

While it is common knowledge for small molecule drugs that parameters of classical compartment models generally allow only for an *apparent* interpretation, this seems to be much less acknowledged for monoclonal antibodies. Although mAbs generally do not exhibit non specific binding—in contrast to small molecule drugs—, this does not imply that apparent volumes are identical to anatomical volumes. In general, the following relation holds

$$V_{apparent} = K_{tissue} \cdot V_{anatomical},$$

where K_{tissue} denotes the tissue-to-plasma partition coefficient. For the mice data, the estimated tissue-to-plasma partition coefficients are identical to the antibody biodistribution coefficients (see eq. (4.20) and [18]). The values range from $0.03 - 0.17$

(see Table 4.5) and therefore are quite different from 1—a value that would result in $V_{apparent} = V_{anatomical}$. For the mAb 7E3 in mice, the summed physiological volumes are $V_{cen} = 3.4$ mL and $V_{per} = 20.0$ mL, while the apparent volumes are much smaller with $V_1 = 1.9$ mL and $V_2 = 1.1$ mL, see Table 5.1 and eq. (5.10). In particular the central volume V_1 has often been associated with the plasma volume (for mice, it is $V_{pla} = 1.7$ mL according to Table 4.3). Such an interpretation, however, is not supported by classical compartment modeling. It is also not in line with the expectations arising from the simplified PBPK model, neither with the experimental data shown in Fig. 4.2, which clearly show two groups of tissues, (i) lung, heart, kidney, liver, spleen, gut that behave kinetically similarly to plasma; and (ii) muscle and skin, which both are kinetically similar, but not to plasma.

Extension of the *simplified* PBPK model to account for a membrane-bound target

Observed non-linearity in the pharmacokinetics of therapeutic monoclonal antibodies is mainly attributed to the saturable binding to the target. Michaelis-Menten kinetics [58], target mediated drug disposition (TMDD) [97–100, 122–125], and receptor-mediated endocytosis (RME) [65, 101] models have been successfully used to mechanistically justify the non-linear clearance. The simplified PBPK model can easily be extended to account for a target. Herein, we exemplify the extension for a membrane-bound target (e.g., the epidermal-growth-factor receptor, EGFR). The mAb-Target interaction is modeled by the extended Michaelis-Menten model. A detailed justification of the model is found in [65, 101], in particular for a mechanistic derivation of such a model and its link to more detailed cell-level systems biology models of the targeted receptor system.

6.1 Parameterization of the *simplified* PBPK model in terms of interstitial concentration

Physiologically, only free mAb in the interstitial space has access to a cell-membrane target. To account for the mAb-Target interaction at the interface of the interstitial space and the cell surface, the simplified PBPK model is first re-parameterized in terms of the interstitial concentration C_{int} based on the rate of change of the concentrations in plasma C_{pla} and in tissues C_{tis} (defined in Chapter 4, eqs. (4.8) and (4.9)). The tissue partition coefficient K_{tis} and the tissue intrinsic clearance $CLint_{tis}$ are respectively translated into the interstitial partition coefficient K_{int} and the interstitial intrinsic clearance $CLint_{int,tis}$ to derive the new ODE of the rate of change of the concentrations in the interstitial space.

For later use, we define the common scaling factor for the interstitial space, SF_{int}, as the fractional tissue volume of the interstitial space,

$$SF_{int} = \frac{V_{int}}{V_{tis}}.$$

6.1.1 Derivation of interstitial partition coefficients and interstitial intrinsic clearance

The following derivations of partition coefficient and intrinsic clearance for the interstitial space are based on the assumption that, in absence of target, extra-vascular mAb mainly distributes into the interstitium. In [74], the authors report that the endosomal volume accounts for only about 0.4% of plasma and <0.1% of interstitial fluid and stress the little contribution of mAb amount in the endosomal space respective to the total amount of mAb distributed in the extra-vascular space. We therefore neglect the amount of mAb in the endosomal space, i.e. $A_{\text{end}} \ll A_{\text{tis}}$ and we further assume that the amount in the interstitial space is a good approximation of the amount in tissue, i.e. $A_{\text{int}} \simeq A_{\text{tis}}$.

This approximation allows to relate the interstitial concentration C_{int} to the tissue concentration C_{tis} via the common scaling factor for the interstitial space, such as

$$C_{\text{tis}} \;=\; \frac{A_{\text{tis}}}{V_{\text{tis}}} \;\simeq\; \frac{A_{\text{int}}}{V_{\text{tis}}} \;=\; \frac{V_{\text{int}}}{V_{\text{tis}}} \cdot \frac{A_{\text{tis}}}{V_{\text{int}}} \;=\; \text{SF}_{\text{int}} \cdot C_{\text{int}}. \tag{6.1}$$

In eq. (4.20) (see Chapter 4, section 4.3.3), we define the tissue-to-plasma antibody biodistribution coefficient ABC_{tis} as

$$\text{ABC}_{\text{tis}} \;=\; \frac{C_{\text{tis,ss}}}{C_{\text{pla,ss}}} \;=\; (1 - \sigma_{\text{tis}}) \cdot \widehat{K}_{\text{tis}}.$$

Similarly, we define the interstitial-to-plasma antibody biodistribution coefficient, ABC_{int} as

$$\text{ABC}_{\text{int}} \;=\; \frac{C_{\text{int,ss}}}{C_{\text{pla,ss}}} \;=\; (1 - \sigma_{\text{tis}}) \cdot \widehat{K}_{\text{int}}. \tag{6.2}$$

Rearranging eq. (6.2) to

$$\widehat{K}_{\text{int}} = \frac{C_{\text{int,ss}}}{(1 - \sigma_{\text{tis}}) \cdot C_{\text{pla,ss}}},$$

$\widehat{K}_{\text{int}}$ can be interpreted as the elimination corrected interstitial-to-accessible plasma partition coefficient. We further define

$$\widehat{K}_{\text{int}} = (1 - E_{\text{tis}}) \cdot K_{\text{int}}, \tag{6.3}$$

with K_{int} the interstitial-to-accessible plasma partition coefficient. $\widehat{K}_{\text{int}}$ and K_{int} are unknown parameters and are derived from previously estimated parameters for tissue, i.e. $\widehat{K}_{\text{tis}}$, the elimination corrected tissue-to-accessible plasma partition coefficients and E_{tis}, the tissue extraction ratios.

Table 6.1: *Comparison of tissue- & interstitial-to-plasma antibody biodistribution coefficients* ABC_{tis} & ABC_{int}.

	ABC_{tis}	ABC_{int}	$\text{ABC}_{\text{int}}/\text{ABC}_{\text{tis}}$
Adipose	0.034	0.249	7.333
Bone	0.038	0.193	5.071
Gut	0.062	0.345	5.583
Heart	0.116	0.770	6.631
Kidney	0.129	0.342	2.654
Liver	0.132	0.597	4.505
Lung	0.108	0.326	3.017
Muscle	0.034	0.254	7.533
Skin	0.125	0.345	2.743
Spleen	0.030	0.136	4.500

Determining the elimination-corrected partition coefficient for the interstitial space

Solving eq. (4.20) for C_{int} and using the relation from eq. (6.1) allow to determine ABC_{int} from ABC_{tis}

$$\text{ABC}_{\text{int}} = \frac{1}{\text{SF}_{\text{int}}} \cdot \text{ABC}_{\text{tis}},$$

which also reads

$$(1 - \sigma_{\text{tis}}) \cdot \widehat{\text{K}}_{\text{int}} = \frac{1}{\text{SF}_{\text{int}}} \cdot (1 - \sigma_{\text{tis}}) \cdot \widehat{\text{K}}_{\text{tis}}.$$

It follows that $\widehat{\text{K}}_{\text{int}}$ is directly derived from estimated $\widehat{\text{K}}_{\text{tis}}$ (for details on the parameter estimation procedure, see section 4.3.2) yielding

$$\widehat{\text{K}}_{\text{int}} = \frac{1}{\text{SF}_{\text{int}}} \cdot \widehat{\text{K}}_{\text{tis}}. \tag{6.4}$$

Table 6.1 summarizes the tissue- & interstitial-to-plasma antibody biodistribution coefficients, ABC_{tis} & ABC_{int} (eqs. (4.20) and (6.2)). ABC_{int} gives insight into the extent of the distribution of mAbs into the interstitial space. The ratio ABC_{int} / ABC_{tis} defines an interstitial-to-tissue partition coefficient. ABC_{int} is 3 to 7 folds higher than ABC_{tis} which is in agreement with the expected extended distribution of a non-binding mAb in the interstitial fluid. This observation must however be qualified as further investigation is required to associate ABC_{int} to the volume interstitial fluid accessible for mAbs distribution as introduced in [7, 126, 127].

Determining the intrinsic interstitial clearance

In section 4.3.1, we define the intrinsic tissue clearance, $\text{CLint}_{\text{tis}}$ (eq. (4.15)) in terms of tissue extraction ratio, E_{tis} (eq. (4.12)) and elimination corrected tissue-

to-accessible plasma partition coefficient, $\widehat{K}_{tis}$ (eq. (4.14)). Similarly, we define the intrinsic interstitial clearance as

$$CLint_{int,tis} = \frac{L_{tis} \cdot E_{int}}{(1 - E_{int}) \cdot K_{int}} = \frac{L_{tis} \cdot E_{int}}{\widehat{K}_{int}},$$

where E_{int} is the extraction ratio related to the interstitial fluid. Based on time scale considerations (see section 4.1.1) and the small fractional plasma and interstitial volumes of the endosomal space [74], we neglect the contribution of the endosomal volume and amount of mAb in the endosomal space respective to the overall tissue. Since (i) the extraction of mAbs from the tissue mainly occurs in the endothelial cells via lysosomal degradation (for details, see section *Pharmacokinetic properties of mAbs*) and (ii) $A_{int} \simeq A_{tis}$, the interstitial and tissue extraction ratios refer to the same extracted fraction of mAb, yielding

$$E_{int} = E_{tis}. \tag{6.5}$$

Exploiting eqs. (6.3), (6.4) and (6.5), it results the interstitial partition coefficient

$$K_{int} = \frac{1}{SF_{int}} \cdot K_{tis}. \tag{6.6}$$

6.1.2 Equations for the *simplified* PBPK model in terms of interstitial concentration

From the previous derivations of K_{int} and $CLint_{int,tis}$, it results the system of ODEs of the simplified PBPK model respective to the interstitial space:

$$V_{int} \frac{d}{dt} C_{int} = L_{tis} \cdot \left((1 - \sigma_{tis}) \cdot C_{pla} - \frac{C_{int,tis}}{K_{int,tis}} \right)$$
$$- CLint_{int,tis} \cdot C_{int,tis}, \tag{6.7}$$

$$V_{pla} \frac{d}{dt} C_{pla} = L_{pla} \cdot \left(C_{in} - (1 - \sigma_{pla}) \cdot C_{pla} \right)$$
$$- CLpla \cdot C_{pla}. \tag{6.8}$$

where the first equation (eq. 6.7) applies to all tissues. Of note, the form of the rate of change of plasma concentrations remains unchanged. However, the inflowing concentration C_{in} into plasma becomes

$$L_{pla} \cdot C_{in} = \sum_{tis} L_{tis} \cdot \frac{C_{int,tis}}{K_{int,tis}}.$$

6.2 Extension of the *simplified* PBPK model with the extended Michaelis-Menten model

The simplified PBPK model is next extended to account for a target, accessible from the interstitial space in the tissue or present at the surface of circulating cells in plasma.

At the cell level, receptor mediated endocytosis (RME) is an important route for cellular uptake and disposition for many mAbs binding to a membrane receptor. As described in details in [65, 101], RME is the process of binding of a ligand to a receptor followed by internalization of the resulting ligand - receptor complex forming an endosome. Within the cell, the complex is recycled to the cell surface or cleaved leading to the degradation of the ligand into lysosomes as depicted in [101, Fig. 1]. Also in [101], Krippendorff et al. derived a reduced model of RME, namely the extended Michaelis-Menten model, eMM [101, Fig. 2: Model B]. The derivation of the eMM model is based on the consideration of the fast time-scale of the transient redistribution of the different receptor species compared to pharmacokinetics of the ligand, translated into quasi-steady state assumptions of the receptor system. The eMM model captures the effective dynamics of the receptor system on the distribution and elimination of the ligand while still allowing for mechanistic interpretation.

In short, the extended Michaelis-Menten model is parameterized in terms of (i) a receptor system capacity B_{max}, describing the maximal amount of drug (that can distribute into the receptor system) divided by V_{int} and B_{max} represents the target expression level; (ii) the Michaelis-Menten constant K_M referring to the half-maximal receptor system capacity; and (iii) the degradation rate constant k_{deg}, describing the elimination of the drug by receptor-mediated endocytosis. The concentration associated with the receptor system C_{RS} [65, 101], is given by

$$C_{RS} = \frac{B_{max} \cdot C_u}{K_M + C_u}. \tag{6.9}$$

Of note, C_u is equivalent to the extra-cellular tissue concentration C_{ex} in [101].

For a target expressed at the cell-surface of a given tissue, B_{max} corresponds to the maximal amount of mAb in the receptor system divided by V_{int} and $C_u = C_{int,u}$, corresponds to the unbound concentration in the interstitial space. From eq. (6.1), we deduce the (total) tissue concentration, $C_{tis} = SF_{int} \cdot C_{int}$.

For a target expressed at the membrane of circulating cell in the plasma space, B_{max} corresponds to the maximal amount of mAb in the receptor system divided by

V_{pla} and $C_u = C_{pla,u}$, the unbound concentration in plasma.

For sake of illustration K_M and k_{deg} are assumed tissue-independent, while $B_{max} = B_{max,tis}$ can be different for different tissues, depending on the expression levels of the target. For tissues not expressing the target, $B_{max,tis}$ is set to 0.

Then, the rate of change of the total concentrations in the interstitial space and in the plasma are given by the following system of ODEs and algebraic equations:

$$
\begin{aligned}
V_{int,tis} \frac{d}{dt} C_{int,tis} = L_{tis} \cdot \left((1 - \sigma_{tis}) \cdot C_{pla,u} - \frac{C_{int,u,tis}}{K_{int,tis}} \right) \\
- CLint_{int,tis} \cdot C_{int,u,tis} \\
- k_{deg} \cdot V_{int,tis} \cdot \frac{B_{max,tis} \cdot C_{int,u,tis}}{K_M + C_{int,u,tis}}
\end{aligned}
\tag{6.10}
$$

with the unbound interstitial concentration defined by

$$
C_{int,u,tis} = \frac{1}{2} \left(C_{int,eff,tis} + \sqrt{(C_{int,eff,tis})^2 + 4K_M C_{int,tis}} \right)
\tag{6.11}
$$

with $C_{int,eff,tis} = (C_{int,tis} - B_{max,tis} - K_M)$; while for plasma, it is

$$
\begin{aligned}
V_{pla} \frac{d}{dt} C_{pla} = L_{pla} \cdot \left(C_{in} - (1 - \sigma_{pla}) \cdot C_{pla,u} \right) \\
- CLpla \cdot C_{pla,u} \\
- k_{deg} \cdot V_{pla} \cdot \frac{B_{max,pla} \cdot C_{pla,u}}{K_M + C_{pla,u}}
\end{aligned}
\tag{6.12}
$$

with the inflowing concentration into the plasma defined as

$$
L_{pla} \cdot C_{in} = \sum_{tis} L_{tis} \cdot \frac{C_{int,u,tis}}{K_{int}}
$$

with the unbound plasma concentration defined by

$$
C_{pla,u} = \frac{1}{2} \left(C_{pla,eff} + \sqrt{(C_{pla,eff})^2 + 4K_M C_{pla}} \right)
\tag{6.13}
$$

with $C_{pla,eff} = (C_{pla} - B_{max,pla} - K_M)$.
In eqs. (6.10)-(6.13), $C_{int,tis}$ and C_{pla} refer to the total concentrations in the interstitial space and in plasma, respectively.

If $B_{max,tis} = 0$ for some tissue (including plasma) then the corresponding square-root term in eqs. (6.11) and (6.13) gives $C_{int,u,tis} = C_{int}$ and $C_{pla,u} = C_{pla}$, the total concentrations in the interstitial space and in plasma, respectively. In this case, the concentration in the receptor system $C_{RS} = 0$ as expected and eq. (6.10) is identical
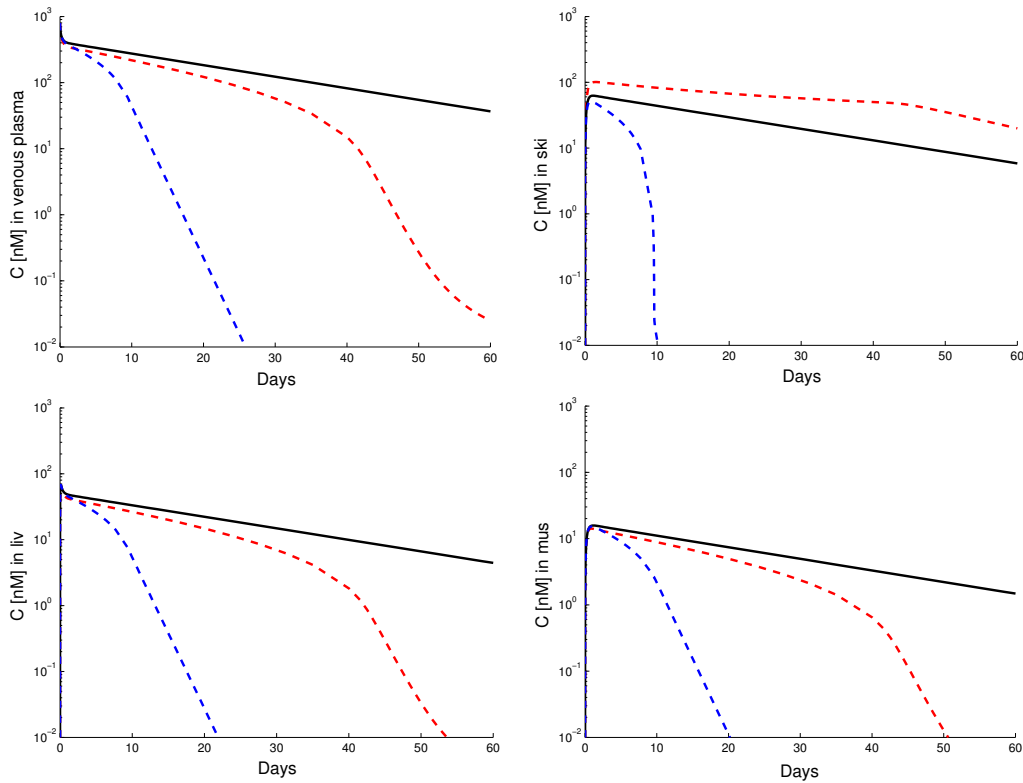
Figure 6.1: *Prediction of plasma and tissue concentration-time profiles based on the simplified PBPK model with a hypothetical target (in skin) for for an i.v. bolus administration of 8 mg/kg 7E3 in mice: the reference prediction without a target (solid black line, as in Fig. 4.2) was compared to a target system with (i) high capacity $B_{max} = 1.33e2$ nM, Michaelis-Menten constant $K_M = 0.013$ nM and slow degradation rate constant $k_{deg} = 4e-5/h$ (middle/top red dashed line); and (ii) with low capacity $B_{max} = 1.33e-2$ nM, Michaelis-Menten constant $K_M = 0.013$ nM and fast degradation rate constant $k_{deg} = 4/h$ (lowest, blue dashed line). The biphasic behavior of the initial phase is present in all three scenarios.*
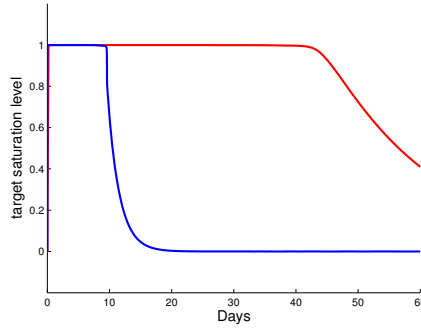
Figure 6.2: *Prediction of target saturation level based on the simplified PBPK model with a hypothetical target (in skin) for an i.v. bolus administration of 8 mg/kg 7E3 in mice with a target system which (i) high capacity* $B_{max} = 1.33e2$ *nM, Michaelis-Menten constant* $K_M = 0.013$ *nM and slow degradation rate constant* $k_{deg} = 4e-5/h$ *(red line); and (ii) with low capacity* $B_{max} = 1.33e-2$ *nM, Michaelis-Menten constant* $K_M = 0.013$ *nM and fast degradation rate constant* $k_{deg} = 4/h$ *(blue line).*

.

to eq. (4.8). The above stated equations can also be used in the case of a tumor tissue (potentially with a time-dependent tumor tissue volume).

Based on the extension of the simplified PBPK model in eqs. (6.10)-(6.12), the impact of a hypothetical target in skin is predicted on plasma and tissue concentration-time profiles. In Fig. 6.1, two different scenarios are depicted and compared to the simplified PBPK model without a target: a targeted system with (i) high receptor system capacity and low elimination rate constant ($B_{max} = 1.33e2$ nM, $k_{deg} = 4e-5/h$); and (ii) low receptor system capacity and high elimination rate constant ($B_{max} = 1.33e-2$ nM, $k_{deg} = 4/h$). The impact of the target on plasma concentrations does not solely depend on the receptor system capacity alone: Although the capacity B_{max} in (ii) is a factor 10000 lower than in (i), the impact on the plasma concentration-time profile is much larger due to faster degradation by receptor-mediated endocytosis, i.e., larger k_{deg}. The plasma and tissue profiles shown in Fig. 6.1 are typical profiles that one would expect in the presence of target-mediated drug disposition. As in the no-target case, the concentration-time profiles of tissues not expressing the target are kinetically similar to the plasma, except for the initial phase (during the first 1-2 days) when the distribution plays the major role. Skin, where the target is expressed, shows a different profile, most notably, when the targeted system has a large receptor system capacity, as in scenario (i).

The level of saturation of the target is defined as

$$\text{Target saturation level} = \frac{C_{RS}}{B_{max}}.$$

From eq. (6.9), it yields

$$\text{Target saturation level} = \frac{C_{int,u}}{K_M + C_{int,u}}.$$

Figure 3.2 shows the saturation level of the target for the two scenarios. For an i.v. bolus of 8mg/kg, even with high maximum receptor capacity, B_{max}, the saturation level of the target is maximum (100 % receptor occupancy) for a prolonged period of time (45 days) mainly attributed to the slow elimination rate constant by RME, k_{deg}. When B_{max} is 10000 times lower, full receptor occupancy is indeed reached rapidly but for a relative short time (10 days) due to the fast elimination of the mAb-target complex.

6.3 Discussion

For compartmental models used to describe the PK of mAbs (see section *Descriptive classical approaches*, [2, 81, 128, 129]), the non-linear clearance is commonly attributed to the interaction with the target. It is described with empirical models, i.e. Michaelis-Menten model, first introduced by Michaelis L and Menten M in 1913 [58] in the context of enzymatic reaction and with semi-mechanistic models, i.e. target mediated disposition models (TMDD) [97, 99, 122–125]. However, these approaches do not allow to represent physiologically the concentration of the drug at the target site, e.g. the interstitial space for a membrane-bound target. More recently Krippendorff et al. derived systems pharmacology models accounting for processes at the cellular level, based on receptor-mediated endocytosis (RME), in order to combine in a unique model the pharmacokinetics of mAbs and the cellular target dynamics [65, 101]. Drug development of therapeutic proteins, especially dose range finding studies in disease animal models and first in human studies, can greatly benefit from these modeling approaches when integrated into the framework of a PBPK model which enables to quantify the concentration of therapeutic mAbs at the target site. Physiologically and mechanistically, a cell-surface target is accessible to the mAb from the interstitial space.

The first step to extend the PBPK model to a target is to consider the interstitial concentration in place of tissue concentrations. The PBPK model is re-parameterized which leads to the derivation from tissue parameters of parameters related to the interstitial space, i.e. partition coefficients, K_{int}, antibody biodistribution coefficients, ABC_{int}, extraction ratios, E_{int} and intrinsic clearances, CL_{int}.

We derive the elimination-corrected partition coefficients for the interstitial space, $\widehat{K}_{int}$, from the elimination-corrected partition coefficients for the tissue $\widehat{K}_{tis}$ which are estimated from typical biodistribution data (see Appendix A.2 and section 4.3.2). One can circumvent the estimation step for to derive $\widehat{K}_{int}$ by making use of the

antibody biodistribution coefficients ABC_{exp} determined from experimental data from different species and genders [18] and detailed in section 4.3.3. From eqs. (4.18) and (6.2), we link the partition coefficient for the interstitial space K_{int} and the interstitial-to-plasma antibody biodistribution coefficient ABC_{int} to ABC_{exp}:

$$K_{int} = \frac{1}{SF_{int}} \cdot \frac{ABC_{exp} - (1 - hct) \cdot res_{blo}}{(1 - \sigma_{tis})(1 - res_{blo})}$$

$$ABC_{int} = \frac{1}{SF_{int}} \cdot \frac{ABC_{exp} - (1 - hct) \cdot res_{blo}}{(1 - res_{blo})} \tag{6.14}$$

with res_{blo} the fraction of residual blood.

In Chapter 4, section 4.3.3, we show that it is not possible to infer which tissue is eliminating and to estimate intrinsic tissue clearances. Only the total clearance, CL_{tot}, can be reliably estimated. Since $E_{int} = E_{tis}$, the same conclusions can be drawn for the intrinsic interstitial clearances. Considering interstitial concentrations, the simplest way to parameterize the simplified PBPK model is based on eqs. (6.7) and (6.8) with species-dependent parameters given in Table 4.3, plasma clearance CLpla given in Table 4.6 (sc. 7) and $E_{int} = CLint_{int} = 0$ for all tissues. It follows from eqs. (6.2)-(6.3) that $K_{int} = \widehat{K}_{int} = ABC_{int} / (1 - \sigma_{tis})$. Therefore K_{int} and $\widehat{K}_{int}$ values can be deduced from ABC_{int} values reported in Table 6.1. For extrapolation of the simplified PBPK model to other species/strains, one can make use of the ABC_{int} values (see Table 6.1, assumed to be species-independent in [18]) by exploiting the relationship in eq. (6.14). However, it becomes critical to identify the peripheral clearances, i.e. the interstitial intrinsic clearances when considering the interaction with the target in order to discriminate between the linear and the non-linear component of the total clearance. More research, experimentally and *in-silico*, needs to be done to address this need.

The interstitial fluid is formed of positively-charged collagen and strongly negatively-charged hyaluronan which, partly due to charges repulsion/attraction and allosteric effect, limit the access of macromolecules to the interstitial fluid space. The resulting phenomenon is referred to the *interstitial exclusion* as described and characterized by Wiig and colleagues for normal tissues [7, 126] and tumor [127]. As a consequence of the exclusion, the concentration of mAb (as any protein) in the accessible interstitial fluid is higher than the concentration derived for the tissue and total interstitial fluid volume. This phenomenon would result in the estimation of higher ABC_{int} than the one reported in Table 6.1. Further extension of the PBPK model will be needed in the future to address this phenomenon.

While the focus of the thesis is to derive mathematical models to describe the disposition of mAbs in absence of target, we show here how to integrate a target into the simplified PBPK model. The first results based on simulation support the statement in [71] that in the presence of a significant target mediated elimination

pathway, the linear component of the total clearance plays a minor role in determining the disposition of monoclonal antibodies.

7

Accounting for Inter-Individual Variability (IIV) in PBPK Models

Mathematical modeling of the pharmacokinetics of drugs has proved its value throughout drug development [48, 130]. The PK models are mainly used as exploratory models to understand the mechanisms involved in the drug disposition and its response (as often the case in pre-clinics) and as predictive models to typically plan future clinical studies (for details, see section *General introduction* and [131–133]). The predictive capabilities are ensured by integrating variability in such models. Analyzing inter-individual variability in pharmacokinetics and understanding its origins is of critical importance in clinical development [38, 134, 135].

Typically, clinical PK data are analyzed in a population analysis framework. One of its application is to investigate the impact of covariates (i.e. independent variables that possibly allow to explain inter-individual variability) on PK parameters to explain observed inter-individual variability [27, 136–140]. Although most covariate models are likely to be motivated by mechanistic or (patho-)physiological considerations, a formal derivation from underlying mechanistic principles is rarely presented.

In drug development, typically PBPK models are used to represent drug PK in a mechanistic manner [31, 48]. Several approaches to model inter-individual variations in physiological parameters in PBPK models for small molecule drugs in human have been proposed in the literature [141–145] and various sources of inter-individual variability are identified, i.e. age, gender, ethnicity, body-weight, creatinine clearance, etc. In the present work, we focus on the predictable impact of variations in *anatomical* and *physiological* parameters typically used as covariates for the PK parameters in empirical models, e.g. clearance and volume of distribution.

We first present a novel scaling approach for anatomical and physiological parameters used in PBPK models. We implement our approach in a generic PBPK model for small molecule drugs, in human, to compare to different approaches and clinical data. We then derive a systematic approach to translate this inter-individual variability into the design of mechanistic covariate models with a direct link to classical compartment models commonly used in clinical drug development. Finally, we present the methodology to include inter-individual variability in the previously developed simplified PBPK models for monoclonal antibodies.

7.1 Whole-body PBPK model for small molecule drugs (SMDs) in human

We adopt the PBPK model for SMDs proposed in [91]. The generic whole-body PBPK model comprises 13 compartments representing important tissues/organs within the human body (see Figure 7.1). In a generic setting for PBPK models for small molecule drugs, it is assumed that the drug distributes within the body via advective transport by the blood flow and via passive diffusion homogeneously into organs/tissues, and that the drug is eliminated predominantly by metabolism in the liver. In the presence of additional or more specific information, the PBPK model can be adapted accordingly, e.g., to account for gut metabolism, renal excretion etc. This also includes patho-physiological alterations in patients.

7.1.1 Parameterization of a generic whole-body PBPK model

Based on the perfusion-limited tissue model, the following system of differential equations describes the rate of change of the total drug concentration C_{tis} in the different tissues (noted tis) (see Table 7.1 for abbreviations):

$$
\begin{aligned}
V_{ven}\frac{d}{dt}C_{ven} &= Q_{co} \cdot (C_{in,ven} - C_{ven}) \\
V_{lun}\frac{d}{dt}C_{lun} &= Q_{co} \cdot \left(C_{ven} - \frac{C_{lun}}{K_{lun}}\right) \\
V_{art}\frac{d}{dt}C_{art} &= Q_{co} \cdot \left(\frac{C_{lun}}{K_{lun}} - C_{art}\right) \\
V_{tis}\frac{d}{dt}C_{tis} &= Q_{tis} \cdot \left(C_{art} - \frac{C_{tis}}{K_{tis}}\right) \\
&\qquad \text{tis = adi; bra; gut; hea; kid; mus; ske; ski; spl} \\
V_{liv}\frac{d}{dt}C_{liv} &= Q_{liv} \cdot \left(C_{in,liv} - \frac{C_{liv}}{K_{liv}}\right) - CLint \cdot C_{liv}.
\end{aligned}
$$

Above, V_{tis} and Q_{tis} denote the tissue volume and blood flow, respectively. K_{tis} denotes the corresponding tissue-to-blood partition coefficient and $C_{in,tis}$ represents the inflowing blood concentration. The term CL_{int} denotes the hepatic intrinsic clearance- Some PBPK models assume that only the unbound concentration in the liver $C_{u,liv}$ can be metabolized, resulting in a term $CLintC_{u,liv}$ instead of $CL_{int}C_{liv}$. Assuming that $C_{u,liv} = fu_{liv}C_{liv}$, this can easily be integrated in our setting by changing CL_{int} to $CL_{int}fu_{liv}$, where fu_{liv} is the fraction unbound of the drug in the liver. For liver and vein, the inflowing concentrations are

$$
C_{in,liv} = \frac{1}{Q_{liv}} \sum_{tis} Q_{tis}\frac{C_{tis}}{K_{tis}}, \quad C_{in,ven} = \frac{1}{Q_{co}} \sum_{tis} Q_{tis}\frac{C_{tis}}{K_{tis}}
$$

where the first sum is taken over spleen, gut and the arterial hepatic vein, while the second sum is taken over adipose, skeleton, brain, heart, kidneys, muscle, skin and the liver. For an i.v. bolus administration, the initial condition $C(t = 0)$ for the system of ODEs is set to $C_{ven}(0) = \text{dose}/V_{ven}$ and $C_{tis}(0) = 0$ otherwise. See [91] for i.v. infusion and p.o. administration.
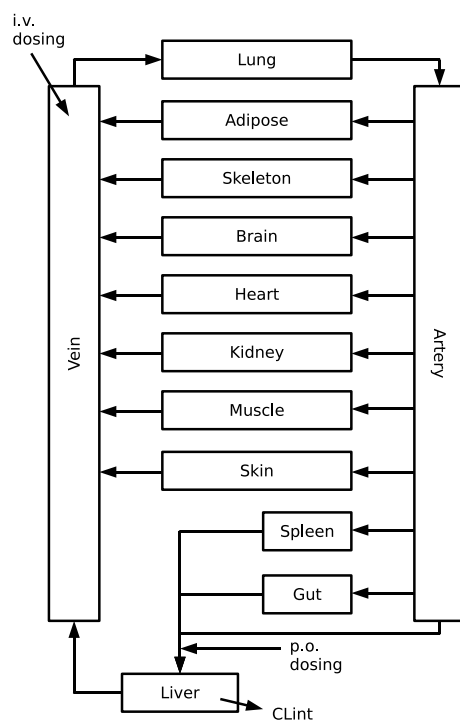
Figure 7.1: *Topology of a generic 13-compartment PBPK model for SMDs. For the purpose of this work, only hepatic elimination is considered.*

7.1.2 Data for reference individuals

Tissue weights are issued from the report of the International Commission of Radiological Protection (ICRP report) [146]. The adipose compartment is identified with the separable adipose tissue while the muscle compartment is identified with the total skeletal muscle. The gut is identified with the sum of the small intestine wall, large intestine wall, left and right colon, and recto-sigmoid wall. The skeleton is identified with total skeleton, including bone and bone marrow. The considered tissues account for 93.4 and 92.1 % of total body weight for male and female adults, respectively.

Blood flows originate from [146]. For consistency, the blood flows of lung, vein and artery are set to the percentage of cardiac output. Alternatively, one could scale all blood flows to match the cardiac output; or include a rest of body compartment. The hematocrit value is determined by dividing the volume of red blood cells by the

Table 7.1: *Reference anatomical and physiological data for adults (20-50y).*

| | | volume[a,b] | | blood flow | |
| | | L | | L/min | |
		male	female	male	female
adipose	(adi)	15.76	20.65	0.325	0.502
brain	(bra)	1.45	1.30	0.780	0.708
gut	(gut)	1.02	0.96	0.910	0.944
heart	(hea)	0.33	0.25	0.260	0.295
kidney	(kid)	0.31	0.28	1.235	1.003
liver[c]	(liv)	1.80	1.40	1.657	1.593
lung	(lun)	0.50	0.42	6.013	5.399
muscle	(mus)	29.00	17.50	1.105	0.708
skeleton	(ske)	8.08	6.00	0.325	0.295
skin	(ski)	3.30	2.30	0.325	0.295
spleen	(spl)	0.15	0.13	0.195	0.177
artery	(art)	1.56	1.15	6.013	5.399
vein	(ven)	3.74	2.75	6.013	5.399
rest of body	(rob)	4.84	4.77	0.487	0.502

[a] without residual blood

[b] tissue density of 1 g/ml for all tissues except adipose (0.92 kg/L) and skeleton (1.3 kg/L) [112, 146]

[c] total hepatic blood flow

The data are referenced for adults (20-50y) for Western Europeans and North Americans. All data are based on [146].

Table 7.2: *Reference anthropometric data for adults (20-50y).*

	male	female
body height (m)	1.76	1.63
body weight (kg)	73.00	60.00
lean body mass (kg)	58.50	41.00
fat mass (kg)	14.50	19.00
body mass index (kg/m^2)	23.57	22.58
body surface area^a (m^2)	1.90	1.66
total blood (L)	5.30	3.90
hematocrit^b (%)	43.40	38.50
cardiac output (L/min)	6.50	5.90

^{a}determined from the relation $\mathrm{BSA(m^2)} = 0.1644 \cdot \mathrm{BH(cm)}^{0.42246} \cdot \mathrm{BW(kg)}^{0.51456}$, see [143].
^{b} from [146].
The data are referenced for adults (20-50y) for Western Europeans and North Americans. All data are based on [146], except for hematocrit values.

total plasma volume as reported in the ICRP report [146]. Table 7.2 summarizes all gender-dependent anthropometric data.

7.1.3 Drug specific parameters

The main physico-chemical properties parameters entering the whole-body PBPK models of SMDs are (i) drug-specific parameters: $\mathrm{pK_a}$ value, n-octanol-buffer partition coefficient $\log P_{\mathrm{ow}}$; and (ii) mixed drug-gender related parameters: fraction unbound in plasma fuP, blood-to-plasma ratio BP, tissue-to-blood partition coefficients $\mathrm{K_{tis}}$, and blood clearance CL.

7.2 Integrating IIV in PBPK models for SMDs

We propose a new approach to scale anatomical & physiological parameters. The novel approach takes into account important anthropometric characteristics like body weight (BW), lean body weight (LBW), body height (BH), body mass index (BMI) and body surface area (BSA). It can be interpreted as a size model approach [147] for anatomical & physiological data, where reference values are scaled with a factor incorporating relevant anthropometric characteristics to obtain the parameter values of the individual of interest.

Individual parameters like tissue volumes V_{tis}, blood flows Q_{tis} and tissue partition coefficients K_{tis} are predicted from parameter values of a reference individual based on scaling factors:

$$V_{\text{tis}} = SV_{\text{tis}} \cdot V_{\text{tis,ref}}, \quad Q_{\text{tis}} = SQ_{\text{tis}} \cdot Q_{\text{tis,ref}}, \quad K_{\text{tis}} = SK_{\text{tis}} \cdot K_{\text{tis,ref}},$$

where SV_{tis}, SQ_{tis} and SK_{tis} denote the scaling factors for tissue weights, blood flows and partition coefficients, respectively, and 'ref' refers to the reference individual. Parameter values for the reference individuals (i.e. adults age 20y-50y) are listed in Table 7.1.

The input of the approach are all parameter values with an index 'ref', including anatomical & physiological data as well as drug specific data. In addition, the covariate values of the reference as well as the individual of interest are required.

All parameters and covariates are based on units [m] for length, [kg] for weight, [L] for volume and [min] for time, unless otherwise stated.

7.2.1 The LBW-scaling approach

Scaling the tissue/organ volumes

For many drugs, the adipose tissue is a key space for distribution [91]. The organ weight (OW) of the adipose tissue is defined as

$$OW_{\text{adi}} = BW - LBW. \tag{7.7}$$

In the absence of knowledge of LBW, it is approximated by the fat free mass FFM [148, 149], i.e.,

$$LBW \approx FFM = \frac{M_{\text{BMI}}}{K_{\text{BMI}} + BMI} \cdot BW, \tag{7.8}$$

with $M_{\text{BMI}} = 9270/216$ and $K_{\text{BMI}} = 6680/216$ (for male) and $M_{\text{BMI}} = 9270/244$ and $K_{\text{BMI}} = 8780/244$ (for female). The body mass index is defined as

$$BMI = BW/BH^2.$$

It yields the following scaling factor for adipose volume

$$SV_{\text{adi}} = \frac{BW - LBW}{BW_{\text{ref}} - LBW_{\text{ref}}}.$$

The brain volume is assumed to remain constant in each age class, i.e.,

$$SV_{\text{bra}} = 1,$$

consistent with [146]. In line with [143], the body surface area is considered as a factor of proportionality for the skin tissue, resulting in

$$SV_{\text{ski}} = \frac{BSA}{BSA_{\text{ref}}}.$$

In the absence of knowledge of BSA, the approximate formula [150] is used:

$$\mathrm{BSA} = \sqrt{\frac{\mathrm{BH} \cdot \mathrm{BW}}{36}}.$$

For the remaining tissues we assume that all tissues scale identically with the scaling factor

$$\mathrm{SV}_{\mathrm{tis}} = \frac{\mathrm{LBW} - \mathrm{OW}_{\mathrm{bra}} - \mathrm{OW}_{\mathrm{ski}}}{\mathrm{LBW}_{\mathrm{ref}} - \mathrm{OW}_{\mathrm{bra,ref}} - \mathrm{OW}_{\mathrm{ski,ref}}}, \tag{7.9}$$

exploiting $\mathrm{BW} - (\mathrm{OW}_{\mathrm{adi}} + \mathrm{OW}_{\mathrm{bra}} + \mathrm{OW}_{\mathrm{ski}}) = \mathrm{LBW} - \mathrm{OW}_{\mathrm{bra}} - \mathrm{OW}_{\mathrm{ski}}$.

Scaling the cardiac output

For the reference individuals, the blood flow for each organ is expressed as a fraction of the cardiac output. In the following, these fractions are assumed to remain constant within each age class. Therefore, for an individual, the blood flow in each organ scales according to the scaling of the cardiac output. In the sequel, we present the derivation of a scaling factor for the cardiac output.

The cardiac output is defined as

$$\mathrm{Q}_{\mathrm{co}} = \mathrm{V}_{\mathrm{S}} \cdot \mathrm{HR}$$

with stroke volume V_{S} and heart rate HR [151]. The stroke volume is related to the end diastolic volume V_{ED} according to Starling's Law of the Heart [152]. It states that for a constant heart rate, the end diastolic volume increases with the volume of blood ejected during the systolic contraction, i.e., the stroke volume, and vice-versa. The ratio of stroke volume to end diastolic volume is defined by the ejection fraction EF [151]:

$$\mathrm{EF} = \frac{\mathrm{V}_{\mathrm{S}}}{\mathrm{V}_{\mathrm{ED}}}.$$

In resting subjects, EF is a constant ratio of approximately 0.6 [153]. Assuming that the end diastolic volume is proportional to the left ventricular volume V_{LV}, it follows the deductive reasoning for the scaling relation of cardiac output: The tissue volume scaling factor $\mathrm{SV}_{\mathrm{tis}}$ is applied to the left ventricular volume yielding

$$\mathrm{V}_{\mathrm{LV}} = \mathrm{SV}_{\mathrm{tis}} \cdot \mathrm{V}_{\mathrm{LV,ref}}$$

and

$$\mathrm{V}_{\mathrm{ED}} = \mathrm{SV}_{\mathrm{tis}} \cdot \mathrm{V}_{\mathrm{ED,ref}}.$$

Exploiting the definition of the ejection fraction and $\mathrm{EF} = \mathrm{EF}_{\mathrm{ref}}$ yields for the stroke volume

$$\mathrm{V}_{\mathrm{S}} = \mathrm{SV}_{\mathrm{tis}} \cdot \mathrm{V}_{\mathrm{S,ref}}.$$

Since amongst healthy, untrained subjects, the heart rates are approximately equal independent of body weight or body height [154], we obtain

$$Q_{co} = SV_{tis} \cdot Q_{co,ref}. \tag{7.10}$$

The above derivation is supported by a number of observations: Combining eq. (7.10) with eq. (7.9), we infer that the cardiac output is approximately scaled with LBW. Under physiological conditions this scaling is reasonable since LBW represents body compartments with high metabolic demands and therefore high oxygen consumption [155, 156]. The larger LBW, the more oxygen needs to be transported into the respective tissues. Therefore a higher blood flow and cardiac output are required. Furthermore, the scaling of the left ventricular volume with the formerly derived SV_{tis} (see eq. (7.9)) is supported by [155, 157, 158] who observed a relation between LBW and left ventricular volume. Finally, for obese individuals it is reported in [154] that an increase in cardiac output is only due to an increase in stroke volume. Herein, we provide supportive evidence for scaling cardiac output according to

$$SQ_{co} = SV_{tis}.$$

Tissue blood flows are then scaled by assuming $SQ_{tis} = SQ_{co}$. It follows the common scaling factor for the peripheral blood flows

$$SQ_{tis} = SV_{tis}. \tag{7.11}$$

Scaling the partition coefficients

Given gender and age dependent changes in binding protein concentrations [159–161], the fraction unbound in plasma fuP is considered as a potential gender dependent parameter. For SMDs, the gender-dependent tissue-to-blood partition coefficients K_{tis} are determined from the relation

$$K_{tis} = \frac{fuP}{BP} Ku_{tis}, \tag{7.12}$$

where the tissue-to-unbound plasma partition coefficients Ku_{tis} are assumed gender independent. Values of Ku_{tis} are predicted based on the *in silico* method proposed by Rodgers et al. [116, 162] (including the proposed correction for residual blood). The derivation of the blood-to-plasma ratio BP highlighted its gender dependency (for details, see Appendix B.3).

Using the fraction unbound in plasma fuP, the blood-to-plasma ratio BP and eq. (7.12) yields

$$K_{tis} = \frac{fuP \cdot BP_{ref}}{BP \cdot fuP_{ref}} \cdot K_{tis,ref},$$

resulting in the scaling factor for tissue-to-blood partition coefficients

$$SK = \frac{fuP}{fuP_{ref}} \cdot \frac{BP_{ref}}{BP}. \tag{7.13}$$

Scaling the intrinsic and blood clearances

The intrinsic hepatic clearance CLint is assumed to scale with the liver volume

$$\mathrm{CLint} = \mathrm{V_{liv}} \cdot \frac{\mathrm{CLint_{ref}}}{\mathrm{V_{liv,ref}}} = \mathrm{SV_{liv}} \cdot \mathrm{CLint_{ref}}.$$

The hepatic extraction ratio is defined as

$$\mathrm{E_{hep}} = \frac{\mathrm{CLint} \cdot \mathrm{K_{liv}}}{\mathrm{CLint} \cdot \mathrm{K_{liv}} + \mathrm{Q_{liv}}}.$$

Exploiting that $\mathrm{SQ_{liv}} = \mathrm{SV_{liv}}$, it yields

$$\mathrm{E_{hep}} = \frac{\mathrm{SK} \cdot \mathrm{CLint_{ref}} \cdot \mathrm{K_{liv,ref}}}{\mathrm{SK} \cdot \mathrm{CLint_{ref}} \cdot \mathrm{K_{liv,ref}} + \mathrm{Q_{liv,ref}}}. \tag{7.14}$$

It follows for the hepatic blood clearance

$$\mathrm{CL} = \mathrm{E_{hep}} \cdot \mathrm{Q_{liv}} = \mathrm{E_{hep}} \cdot \mathrm{SQ_{liv}} \cdot \mathrm{Q_{liv,ref}}.$$

7.2.2 Validation of the the LBW-scaling approach

In the autopsy study by De La Grandmaison et al. [163], organ weights of $n = 355$ male and $n = 329$ female Caucasians are reported. Based on the mean and standard deviation of BH and BMI, a virtual population of $n = 355$ male and $n = 329$ female individuals is generated (for details, see appendix B.2), taking into account known correlations between BW and BH. The distribution of individual BH and BW is shown in Fig. 7.2 for male (top, left) and female (top, right) subpopulations. For each individual of the virtual De La Grandmaison population, the organ weights are assessed using the LBW-scaling approach and compared to the BH-scaling [142] and the regression equation approach [143]. For the experimental data of the autopsy study, a normal distribution is assumed as suggested in [163] by reporting mean and standard deviation. The conclusions, however, do not depend on this distributional assumption. No information on the correlation between different organ weights is provided in [163].

Figures 7.2 and 7.3 show the predicted distribution of organ weights based on the herein proposed LBW-scaling approach in comparison to existing methods (BH-scaling [142] and the regression equation approach [143]) and experimental data from the large autopsy study by De La Grandmaison [163]. For heart, kidneys, liver and lung, the LBW-scaling approach is in close agreement with the experimental data. The BH-scaling approach largely underestimates the variability, while the regression equation approach poorly predicts mean values. For spleen, the LBW-scaling approach largely underestimates the observed variability—in comparison to the other two approaches. However, it still generates more realistic variations. The lack of correlation of spleen
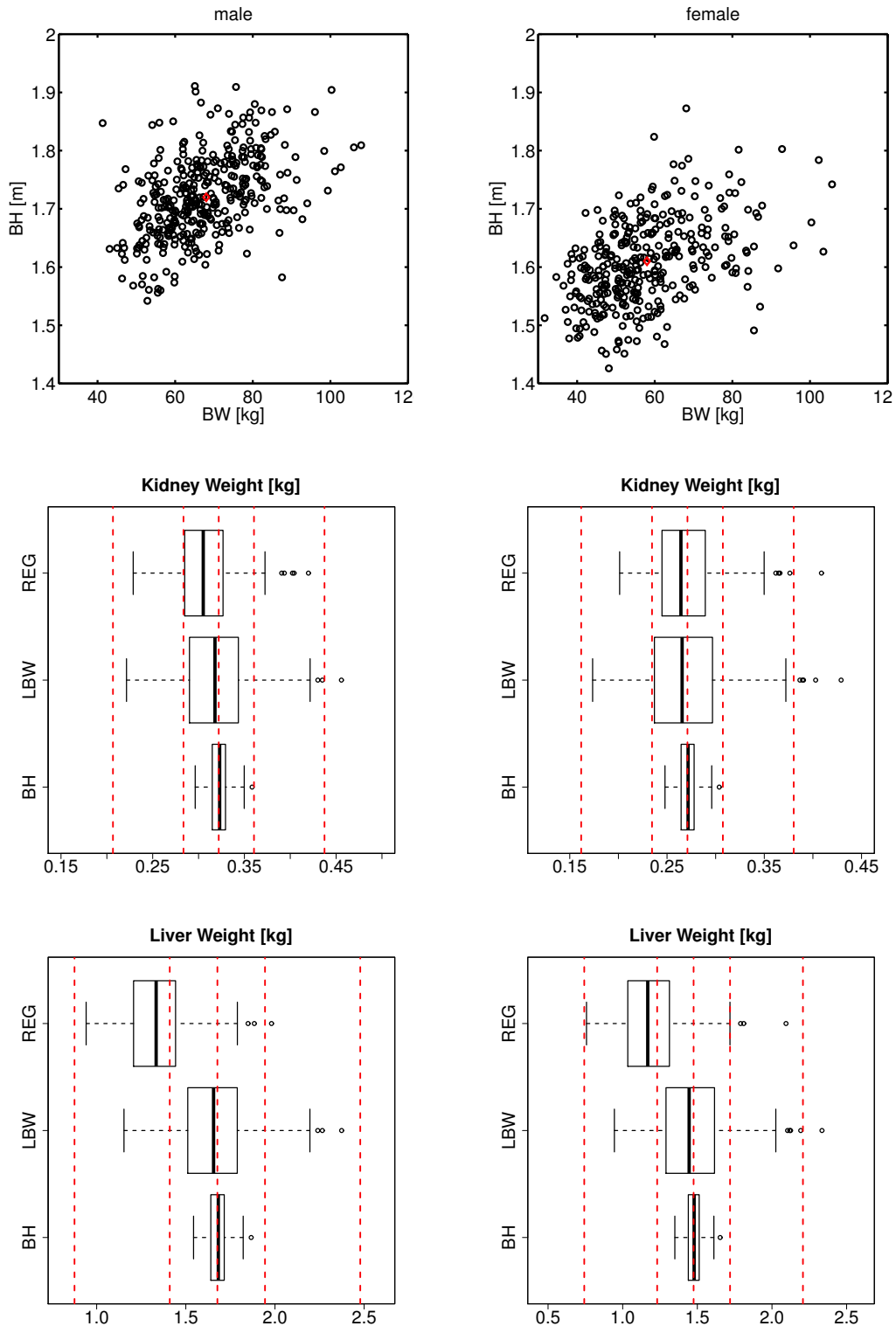
Figure 7.2: *Distribution of body height (BH) and body weight (BW) for a male (left) and female (right) population with characteristics given in Table 7.3 (red diamond = mean value). Comparison of lean-body weight (LBW) scaling approach, regression equation approach (REG) and BH scaling approach (given in terms of box plots) in comparison to experimental data (characterized in terms of red dashed lines) from the autopsy study [163] for male (left) and female (right) population. Box plots & dashes lines from left to the right: the lower whisker, the 0.25 quartiles, the median, the 0.75 quartile and the upper whisker.*
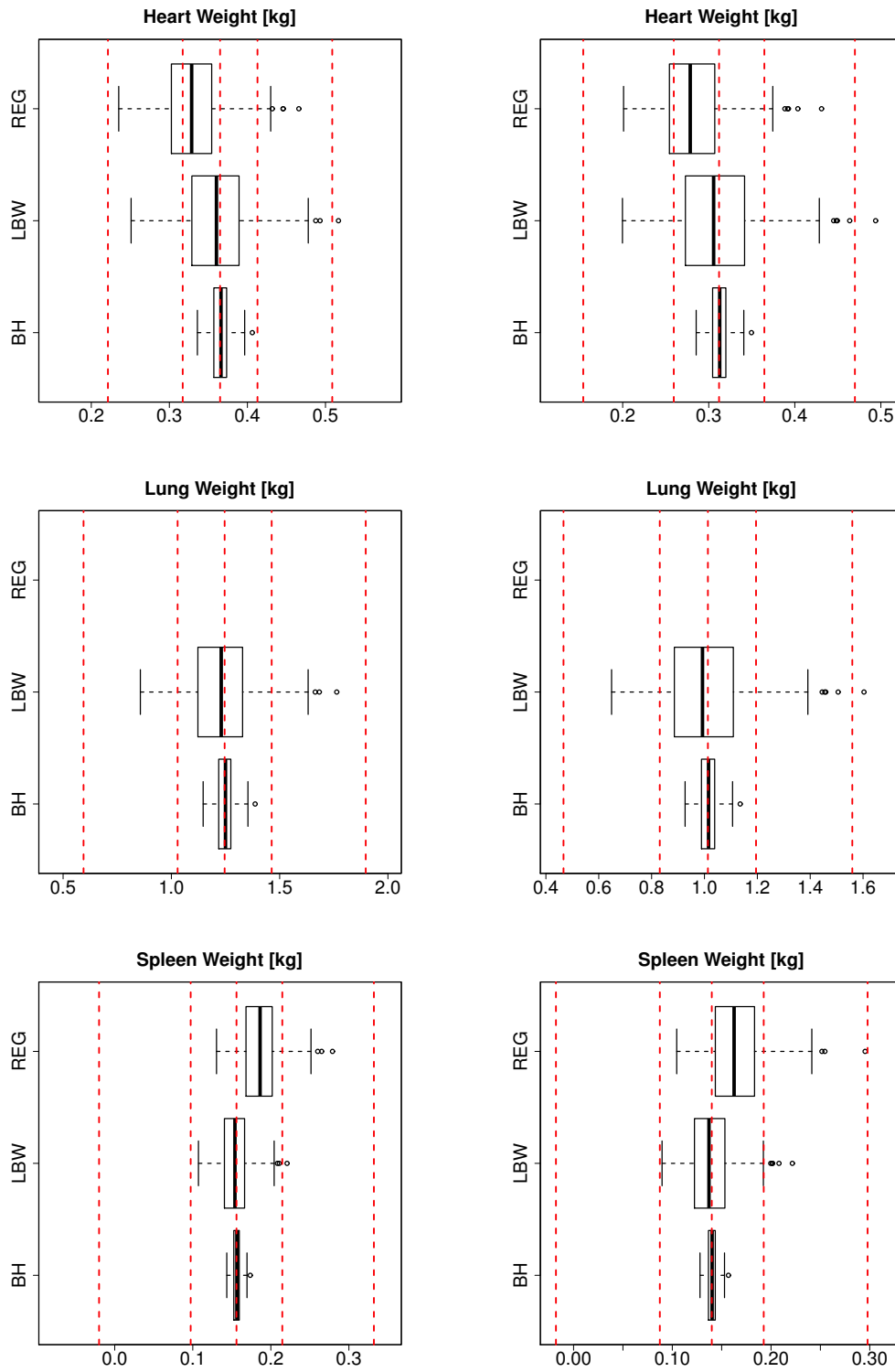
Figure 7.3: *For description, see caption of Fig. 7.2. For lung, also a lean body weight (LBW) scaling approach is used in [143].*

Table 7.3: *Characteristics of the autopsy study by De La Grandmaison et al. [163].*

	Males (n = 355)		Female (n = 329)	
	Mean ± SD	Range	Mean ± SD	Range
Age (years)	42 ± 17		49 ± 20	
Body height (cm)	172 ± 7.5		161 ± 7.5	
Body weight (kg)	68 ± 11		58 ± 13.2	
BMI (kg/m^2)	22.8 ± 3.3		22.5 ± 4.5	
Heart (g)	365 ± 71	$90 - 630$	312 ± 78	$174 - 590$
Right lung (g)	663 ± 239	$200 - 1593$	546 ± 207	$173 - 1700$
Left lung (g)	583 ± 216	$206 - 1718$	467 ± 174	$178 - 1350$
Liver (g)	1677 ± 396	$670 - 2900$	1475 ± 362	$508 - 3081$
Right Kidney (g)	162 ± 39	$53 - 320$	135 ± 39	$45 - 360$
Left Kidney (g)	160 ± 41	$50 - 410$	136 ± 37	$40 - 300$
Spleen (g)	156 ± 87	$30 - 580$	140 ± 78	$33 - 481$

weight with BW, BH or BMI has been observed in females in [164], and might be attributable to its "spongy" structure [143].

7.3 Classical compartment models with mechanistically integrated covariates

In comparison to empirical, purely descriptive models, mechanism-based pharmacokinetic models (i.e. classical compartment models and whole-body PBPK models) contain key elements to characterize, in a strictly quantitative manner, processes affecting the pharmacokinetic properties of drugs. The addition of mechanistic covariate models reinforces the predictability of such models.

7.3.1 Derivation of lumped parameters

The starting point is the previously described whole-body PBPK model whose anatomical & physiological parameters incorporate important anthropometric characteristics. Based on the lumping approach described in [91], the dimensionality of the PBPK model is reduced to compartment models with lumped volumes V_L, lumped blood flows Q_L, lumped tissue-to-blood partition coefficients K_L and blood clearance CL.

On the basis of the scaling relations (7.7)-(7.14) and the lumping approach [91], parameters of the lumped model are given as

$$V_L = \sum_{tis} SV_{tis} \cdot V_{tis,ref} \tag{7.15}$$

$$K_L = \frac{1}{V_L} \sum_{tis} SV_{tis} \cdot V_{tis,ref} \cdot SK \cdot \widehat{K}_{tis} \tag{7.16}$$

$$Q_L = \sum_{tis} SQ_{co} \cdot Q_{tis,ref},$$

where the sum is taken over all tissues that are grouped together in the lumped compartment 'L'. Above, $\widehat{K}_{tis}$ denotes the elimination-corrected tissue-to-blood partition coefficient

$$\widehat{K}_{tis} = (1 - E_{tis})K_{tis},$$

where E_{tis} is the tissue-specific extraction ratio (see [91] for details). In the generic PBPK model, it is $E_{liv} = E_{hep} > 0$ and $E_{tis} = 0$ for all other tissues. For artery and vein, we formally set $\widehat{K}_{ven} = \widehat{K}_{art} = 1$.

If tissue volumes are all scaled with identical $SV = SV_{tis}$, then eq. (7.15) can be simplified to

$$V_L = \sum_{tis} SV_{tis} \cdot V_{tis,ref} = SV \cdot \sum_{tis} V_{tis,ref} = SV \cdot V_{L,ref}. \tag{7.17}$$

Thus, the individual volume V_L can be derived from the reference volume $V_{L,ref}$ via the simple scaling relation $V_L = SV \cdot V_{L,ref}$. In general, however, volume scaling factors might differ between tissues. To bridge the gap to the simplicity of common empirical covariate relations, an approximate scaling factor is defined so that eq. (7.17) holds approximately.

For the LBW-scaling approach, we define the common scaling factors as

$$SF_{LBW} = \frac{LBW}{LBW_{ref}} \quad \text{and} \quad SF_{adi} = \frac{BW - LBW}{BW_{ref} - LBW_{ref}}. \tag{7.18}$$

For all tissues except brain and skin, SF_{LBW} provides an excellent approximation to the scaling factors SV_{tis} in eq. (7.9). For brain and skin, the approximation has to be seen in the light of eq. (7.17). Since brain and skin comprise only 8% of LBW (reference adult), the error introduced to the lumped volume V_L in eq. (7.17) is negligible. Regarding the blood flows, we also approximate the scaling factor SQ by SF_{LBW} in view of eq. (7.11). Finally, we approximate $SK = 1$ in eq. (7.13).

7.3.2 Low-dimension compartment models integrating mechanistic covariate models

The mechanistic approach to covariate modeling is applied to derive commonly used 2-compartment models describing the blood concentration time profiles of SMDs.

The model incorporates the mechanistic covariate models, consistent with the generic whole-body PBPK model and the inter-individual variability based on the LBW-scaling approach.

For the generic situation, i.e. the liver is lumped into the central compartment and the adipose tissue is part of the peripheral compartment (see [91] for details), we obtain

$$
\begin{aligned}
V_1 \frac{d}{dt} C_1 &= Q(C_2 - C_1) - CL \cdot C_1 + r_{admin}, \\
V_2 \frac{d}{dt} C_2 &= Q(C_1 - C_2)
\end{aligned}
$$

with mechanistic covariate models

$$
\begin{aligned}
V_1 &= \Theta_1 \cdot SF_{LBW} & (7.19) \\
V_2 &= \Theta_2 \cdot SF_{LBW} + \Theta_{adi} \cdot SF_{adi} & (7.20) \\
Q &= \Theta_Q \cdot SF_{LBW} \\
CL &= \Theta_{CL} \cdot SF_{LBW}.
\end{aligned}
$$

The scaling factors are defined in eq. (7.18). The population parameters satisfy

$$
\Theta_1 = \sum_{tis} \widehat{K}_{tis,ref} \cdot V_{tis,ref},
$$

where the sum is taken over all tissues of the central compartment;

$$
\Theta_2 = \sum_{tis \neq adi} \widehat{K}_{tis,ref} \cdot V_{tis,ref},
$$

where the sum is taken over all tissues of the peripheral compartment except adipose tissue; and finally

$$
\begin{aligned}
\Theta_{adi} &= \widehat{K}_{adi,ref} \cdot V_{adi,ref} \\
\Theta_Q &= Q_{L,ref} \\
\Theta_{CL} &= CL_{ref}.
\end{aligned}
$$

All population parameters have a mechanistic interpretation. The volume of distribution at steady state for the reference individual $V_{ss,ref}$ is given by

$$
V_{ss,ref} = \Theta_1 + \Theta_2 + \Theta_{adi}. \tag{7.21}
$$

Figure 7.4 compares the venous blood concentrations of Lidocaine (400mg, 60min i.v. infusion) predicted by the whole-body PBPK and the compartment model with mechanistically integrated covariates for a single individual (left) and a larger virtual population (right). All predictions are in excellent agreement and in line with theoretical expectations. They illustrate the predictive power of the new approach to mechanistic covariate modeling.
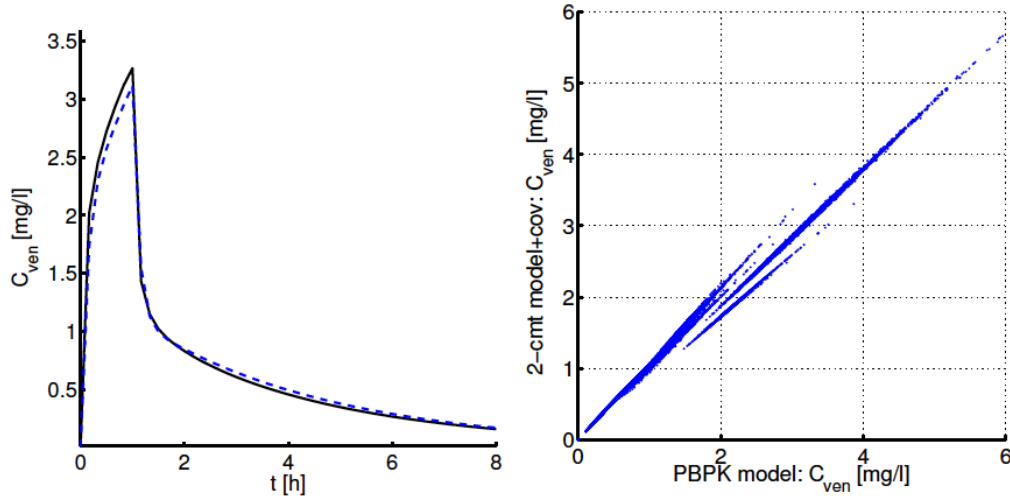
Figure 7.4: *PBPK model vs. associated 2-compartment model with mechanistically integrated covariates. Prediction of venous blood concentration after administration of 400mg Lidocaine (60min i.v. infusion). Left: Comparison for a single individual based on the PBPK model (solid black) and the 2-compartment model (dashed blue). Right: Comparison for the virtual De La Grandmaison population with n = 684 male/female individuals.*

7.4 Integrating IIV in PBPK models for mAbs

We described above how to integrate inter-individual variability in PBPK models for SMDs based on a set of common anthropometric characteristics that have mechanistic, physiological and clinical pertinence and proved to be of significant relevance in covariate analyses. Such analyses are also performed routinely to describe and understand the IIV in PK data of monoclonal antibodies. Bodyweight is often reported to be a significant covariate on the volume of distribution and/or clearance [3]. In this section, we adapt the LBW-approach and exemplify how to introduce inter-individual variability in the *simplified* PBPK model for mAbs. Individual tissue volumes V_{tis}, plasma flows Q_{tis}, lymph flows L_{tis} and tissue partition coefficients K_{tis} can be predicted from parameter values of a reference individual based on scaling factors:

$$V_{tis} = SV_{tis} \cdot V_{tis,ref}, \quad Q_{tis} = SQ_{tis} \cdot Q_{tis,ref}, \quad L_{tis} = SL_{tis} \cdot L_{tis,ref}, \quad K_{tis} = SK_{tis} \cdot K_{tis,ref},$$

where SV_{tis}, SQ_{tis}, SL_{tis} and SK_{tis} denote the scaling factors for tissue weights, plasma flows, lymph flows and partition coefficients, respectively, and 'ref' refers to the reference individual.

89

7.4.1 Scaling organ volumes with the LBW-scaling approach

In [78], Borvark and co-workers study the distribution of a murine IgG1 in mice. They show that skin, muscle and adipose play a major role in the distribution of mAbs; the same observation is reported for SMDs by Pilari and Huisinga in [91]. This similarity motivated us to adapt the LBW-scaling approach previously described for SMDs (in section 7.2.1) to mAbs. The LBW-approach is based on a specific scaling for the organ volumes of adipose and skin while other tissues volumes are scaled similarly. The weight of the adipose is defined by

$$\mathrm{OW_{adi} = BW - LBW.}$$

It follows the scaling factor for the volume of adipose:

$$\mathrm{SV_{adi} = \frac{BW - LBW}{BW_{ref} - LBW_{ref}}.}$$

The volume of skin scales with the body surface area (BSA) [143],

$$\mathrm{SV_{ski} = \frac{BSA}{BSA_{ref}}.}$$

The scaling factor of the remaining tissues is then adjusted and defined as

$$\mathrm{SV_{tis} = \frac{LBW - OW_{ski}}{LBW_{ref} - OW_{ski,ref}}.}$$

7.4.2 Scaling plasma & lymphatic flows

In section 7.2.1, we show that the cardiac output scales accordingly to the tissue volumes:

$$\mathrm{SQ_{co} = SV_{tis}.}$$

Assuming that plasma flows scale like the cardiac output, i.e. $\mathrm{SQ_{tis} = SQ_{co}}$, it is

$$\mathrm{SQ_{tis} = SV_{tis}.}$$

In published PBPK models for mAbs [69, 72–74] and in the herein PBPK models, the peripheral lymphatic flows are defined as a fraction of the tissue plasma flow, i.e. $\mathrm{L_{tis} = \alpha \cdot Q_{tis}}$ with $\alpha = 0.02$ for visceral organs and $\alpha = 0.04$ for non-visceral organs [16, 66, 69]. It follows that the lymph flows scale like the blood flows, i.e. $\mathrm{SL_{tis} = SQ_{tis}}$ yielding

$$\mathrm{SL_{tis} = SV_{tis}.}$$

7.4.3 Scaling partition coefficients

For the *simplified* PBPK model, we define (in section 4.1.2, eq. (4.2)) the tissue-to-accessible plasma partition coefficient, K_{tis}, as

$$\frac{1}{K_{tis}} = (1 - \sigma_{lymph}) \cdot \beta + FR \cdot \alpha \cdot \delta,$$

where FR is the fraction of free mAb recycled from the endosomal space; α and β, are the multiplicative factors relating mAb concentrations in the endosomal space, C_e, and in the interstitial space, C_i, to the tissue concentrations, C_{tis}; and δ is the fraction of lymphatic flow determining the endosomal outflow, $Q_{out,tis}$, such that

$$C_e = \alpha \cdot C_{tis} \text{ and } C_i = \beta \cdot C_{tis} \text{ and } Q_{out,tis} = \delta \cdot L_{tis}.$$

In absence of data supporting otherwise, we assume that α, β and δ are independent of gender, BW and BH. It results that no specific scaling is needed for the tissue partition coefficients, i.e. SK = 1. Therefore,

$$K_{tis} = K_{tis,ref}.$$

The interstitial-to-accessible plasma partition coefficient, K_{int} (defined in section 6.1, eq. (6.6)), scales directly from K_{tis}. Thus, the same scaling principles are applied to K_{int} yielding

$$K_{int} = K_{int,ref}.$$

7.4.4 Scaling tissue intrinsic clearances and total plasma clearance

Scaling the tissue intrinsic clearance

In the *simplified* PBPK model for mAbs, any tissue can be eliminating. Similarly to the intrinsic hepatic clearance determined for SMDs (for details see section 7.2.1), the tissue-specific intrinsic clearance, $CLint_{tis}$, is assumed to scale with the tissue volume, so that

$$CLint_{tis} = V_{tis} \cdot \frac{CLint_{tis,ref}}{V_{tis,ref}} = SV_{tis} \cdot CLint_{tis,ref}.$$

The tissue extraction ratio, derived in section 4.3.1 (eq. (4.12)), is expressed as

$$E_{tis} = \frac{CLint_{tis} \cdot K_{tis}}{CLint_{tis} \cdot K_{tis} + L_{tis}}.$$

Exploiting $SL_{tis} = SV_{tis}$ and $SK_{tis} = 1$ (for details, see paragraph above), it yields

$$E_{tis} = \frac{CLint_{tis,ref} \cdot K_{tis,ref}}{CLint_{tis,ref} \cdot K_{tis,ref} + L_{tis,ref}} = E_{tis,ref}.$$

Scaling the tissue plasma clearance

For a given eliminating tissue, the peripheral plasma clearance (see section 4.3.3) is given by

$$\mathrm{CLpla_{tis}} = \mathrm{E_{tis}} \cdot (1 - \sigma_{\mathrm{tis}}) \cdot \mathrm{L_{tis}}$$

with σ_{tis} denoting the effective tissue reflection coefficient. Assuming that σ_{tis} is gender, BW and BH independent, it follows for the individual tissue plasma clearance

$$\mathrm{CLpla_{tis}} = \mathrm{E_{tis,ref}} \cdot (1 - \sigma_{\mathrm{tis,ref}}) \cdot \mathrm{SL_{tis}} \cdot \mathrm{L_{tis,ref}}$$
$$\mathrm{CLpla_{tis}} = \mathrm{SL_{tis}} \cdot \mathrm{CLpla_{tis,ref}}.$$

Exploiting $\mathrm{SL_{tis}} = \mathrm{SV_{tis}}$ it is finally

$$\mathrm{CLpla_{tis}} = \mathrm{SV_{tis}} \cdot \mathrm{CLpla_{tis,ref}}. \tag{7.22}$$

Scaling the total clearance

The total clearance is previously defined in eq. (4.22), i.e.

$$\mathrm{CLtot} \quad = \quad \sum_{\mathrm{tis} \neq \mathrm{pla}} \mathrm{CLpla_{tis}} + \mathrm{CLpla}.$$

From the above equation, scaling the total clearance is directly inferred from scaled peripheral plasma clearances, $\mathrm{CLpla_{tis}}$, and scaled plasma clearance occurring from the plasma compartment, CLpla. The scaling of peripheral plasma clearances $\mathrm{CLpla_{tis}}$ is defined in previous paragraph. In the sequel, we justify the scaling of the plasma clearance.

CLpla, is derived from the plasma clearance of a reference individual scaled with the plasma volume, namely

$$\mathrm{CLpla} = \mathrm{V_{pla}} \cdot \frac{\mathrm{CLpla_{ref}}}{\mathrm{V_{pla,ref}}}.$$

We define the scaling factor for the plasma volume $\mathrm{SV_{pla}}$ such that

$$\mathrm{V_{pla}} = \mathrm{SV_{pla}} \cdot \mathrm{V_{pla,ref}}. \tag{7.23}$$

The volume associated with the plasma compartment $\mathrm{V_{pla}}$ represents the sum of the volumes of artery and vein and the peripheral vascular volumes. It is defined as

$$\mathrm{V_{pla}} = \sum_{\mathrm{tis} \neq \mathrm{art;\,ven;\,adi;\,ski}} \mathrm{V_{p,tis}} + \mathrm{V_{art}} + \mathrm{V_{ven}} + \mathrm{V_{p,ski}} + \mathrm{V_{p,adi}}. \tag{7.24}$$

Under the general assumption that vascular volumes scale like tissue volumes i.e. with SV_{tis}, SV_{adi} and SV_{ski}, eq. (7.24) also reads

$$V_{\text{pla}} = \text{SV}_{\text{tis}} \cdot V_{\text{p,tis,ref}} + \text{SV}_{\text{ski}} \cdot V_{\text{p,ski,ref}} + \text{SV}_{\text{adi}} \cdot V_{\text{p,adi,ref}} \quad (7.25)$$

$$\text{with } V_{\text{p,tis,ref}} = \sum V_{\text{p,tis,ref}} + V_{\text{art,ref}} + V_{\text{ven,ref}}.$$
$$\text{tis} \neq \text{art}; \text{ven}; \text{adi}; \text{ski}$$

Dividing by $V_{\text{pla,ref}}$, eq. (7.25) becomes

$$V_{\text{pla}} = \left(\text{SV}_{\text{tis}} \frac{V_{\text{p,tis,ref}}}{V_{\text{pla,ref}}} + \text{SV}_{\text{ski}} \frac{V_{\text{p,ski,ref}}}{V_{\text{pla,ref}}} + \text{SV}_{\text{adi}} \frac{V_{\text{p,adi,ref}}}{V_{\text{pla,ref}}} \right) V_{\text{pla,ref}}.$$

It follows the scaling factor for plasma,

$$\text{SV}_{\text{pla}} = \text{SV}_{\text{tis}} \frac{V_{\text{p,tis,ref}}}{V_{\text{pla,ref}}} + \text{SV}_{\text{ski}} \frac{V_{\text{p,ski,ref}}}{V_{\text{pla,ref}}} + \text{SV}_{\text{adi}} \frac{V_{\text{p,adi,ref}}}{V_{\text{pla,ref}}}. \quad (7.26)$$

For the reference individual (across species, gender and age classes), it is reasonable to consider that $V_{\text{p,ski,ref}}$ & $V_{\text{p,adi,ref}} \ll V_{\text{pla,ref}}$. In mice, skin and adipose volumes account only for 3.27% and 0.66% of total plasma space, respectively [67, 103, 112]. Thus, Equation (7.26) simplifies to

$$\text{SV}_{\text{pla}} = \text{SV}_{\text{tis}} \cdot \frac{V_{\text{p,tis,ref}}}{V_{\text{pla,ref}}}.$$

From eqs. (7.22) and (7.23), scaled individual total clearance is finally expressed as

$$\text{CLtot} = \sum \text{SV}_{\text{tis}} \cdot \text{CLpla}_{\text{tis,ref}} + \text{SV}_{\text{pla}} \cdot \text{CLpla}_{\text{ref}}.$$
$$\text{tis} \neq \text{pla}$$

We earlier highlighted in Chapter 4 that it is not possible to infer which tissues are involved and to which extent into the unspecific elimination, i.e. the total clearance CLtot, from common experimental data (only plasma, or plasma and tissue data). We also discussed that the simplest way to parameterize the simplified PBPK model is based on eqs. (4.8)-(4.9) with the total clearance occurring from the plasma space, i.e. $\text{CLpla} = \text{CLtot}$ (for details see Section 4.3.3, CLpla given in Table 4.6 (sc. 7)) and $E_{\text{tis}} = \text{CLint}_{\text{tis}} = 0$ for all tissues. This indeed impacts the scaling of CLtot, i.e. one need to consider that $\text{CLpla} = \text{CLtot}$ for both the reference individual and the studied individual. Here, the scaling for the total clearance becomes $\text{CLtot} = \text{SV}_{\text{pla}} \cdot \text{CLpla}_{\text{ref}}$.

7.5 Discussion

In the first part of this chapter, we propose a new scaling approach of physiological and anatomical parameters in PBPK models. There are several approaches to model inter-individual variability of physiological parameters in PBPK models for SMDs [141–145, 165]; but only few provide all necessary information to predict it. Price et al. [143] review various regression equations describing the variations of physiological parameter observed in different studies as a function of different covariates. A general disadvantage of the regression analysis approach is its dependence on the characteristics of the underlying study population.

Willmann et al. [142] take a different approach restricting their set of covariates essentially to BH and BW, and including additional random perturbations to create a virtual population. Adipose tissue weight is defined as the weight that remains after scaling all other tissues. Hence, any error in scaling non-adipose tissues impacts the accuracy of adipose weight. Young et al. [145] take an intermediate approach. They fit up to fifth-order polynomials in BW. As in the Willmann et al. approach, adipose weight is defined as the difference between BW and the sum of all remaining tissue weights, resulting in the above mentioned disadvantage.

In contrast, the present approach is based on a set of common anthropometric characteristics that have proven to be of relevance in the covariate analyses of clinical pharmacokinetic data and that are underpinned by mechanistic considerations. Due to its important role in PK, adipose weight is defined as accurately as possible using its definition $BW - LBW$.

This new approach suggests a new covariate relation for the volume of distribution at steady state V_{ss} that seamlessly integrates both, BW and LBW as covariates. Combining eqs. (7.19),(7.20) and (7.21) yields

$$V_{ss} = V_{ss,ref} \cdot \left((1 - R) \cdot \frac{LBW}{LBW_{ref}} + R \cdot \frac{BW - LBW}{BW_{ref} - LBW_{ref}} \right), \qquad (7.27)$$

where the drug-specific parameter $R = \theta_{adi}/V_{ss,ref}$ denotes the adipose-to-total volume of distribution ratio for the reference individual.

Whether or not LBW and BW are systematically measured and reported data depends on the underlying study design (and occasionally on the training of staff in clinical investigation centers). However, for some drugs with small therapeutic window, reliable scaling relations are mandatory for extrapolation. To circumvent missing LBW and BW data, we rewrite eq. (7.8) to define the percentage lean body weight

$$\%LBW := \frac{LBW}{BW} = \frac{M_{BMI}}{K_{BMI} + BMI}.$$

The term $(1 - \%LBW)$ represents the percentage of body fat, a common measure of obesity [166–168].

We obtain $LBW = \%LBW \cdot BW$ and $OW_{adi} = BW - LBW = (1 - \%LBW) \cdot BW$. If the studied population only includes volunteers/patients such that (approximately)

$$BMI = \text{const}, \quad \text{or equivalently} \quad \%LBW = \text{const}, \tag{7.28}$$

then $LBW/LBW_{ref} = BW/BW_{ref} = (BW - LBW)/(BW_{ref} - LBW_{ref})$. This is typically the case in Phase I studies. In such a case, the scaling equation (7.27) simplifies to

$$V_{ss} = V_{ss,ref} \cdot \frac{BW}{BW_{ref}}.$$

Most importantly, this equation holds *for any value of* R, i.e., for any drug. For a population satisfying condition (7.28), scaling with BW is equally appropriate, and—depending on the actual clinical data—might even result in the best covariate relation. BW-based scaling, however, could be completely misleading, when R is indeed large; i.e. for the typical individual of a given population, the weight of adipose accounts for a non negligible fraction of the total volume of distribution $V_{ss,ref}$. In this case, extrapolation to an obese population based on BW would result in erroneous predictions. If precise scaling is mandatory, the design of a clinical study including volunteers with a range of %LBW values is expected to be more informative. In this context, pre-clinical data may be exploited to generate expectations. For example, in [169], a prolonged accumulation of diazepam in obese was found. Elimination half-life was greatly prolonged in the obese subjects (82 vs. 32 hours), with no change in total metabolic clearance. Instead, a large increase in volume of distribution (228 vs. 70 liters) was the reason for prolongation of elimination half-life [169]. Pre-clinical rat data in [162] on tissue-to-plasma partition coefficients show a marked difference with $K_{adi} \geq 4.8 \cdot K_{tis}$ (for tis $\neq$ adi). Hence, translating data from rat to human would have at least flagged this issue. This knowledge is important for the appropriate design of clinical trials, following the spirit of the "learning vs. confirming" approach [27, 28, 30, 36, 170, 171].

In the second part of this chapter, we theoretically establish how to include IIV in the simplified PBPK model for mAbs, based on the LBW-scaling approach previously developed for PBPK models for SMDs. As just discussed, this approach is relevant for human when LBW, BW or BMI are measured/determined. However, the simplified PBPK model is developed and validated in mice. BMI is not a metric that is calculated for pre-clinical species. Measuring LBW can prove to be challenging: Formulas do not apply to animal species, experimental measurements including impedance analysis and imaging techniques are too costly to be routinely used, finally, weighing fat tissue for each animal requires a lot of effort from *in-vivo* teams and more importantly is against animal welfare. Most of laboratory animal species are genetically very similar. In animals of same age, one does no expect much variability of organ weights and eq. (7.9) can be approximated by $SV_{tis} = BW \ / \ BW_{ref}$.

Summary and conclusion

Monoclonal antibodies (mAbs) are engineered immunoglobulins G (IgG) used for more than 20 years as targeted therapy in disease areas where specific antigens are identified, mainly oncology, infectious diseases and (auto-)immune disorders. mAbs are hydrophilic and charged therapeutic proteins with high and selective affinity for their target. These properties greatly influence the pharmacokinetics (PK) of mAbs: Convective transport via blood and lymph flows, extravasation from the vascular space in tissues via pinocytosis and transcytosis, lysosomal degradation in endosomes, target-mediated drug disposition (TMDD) are key mechanisms governing the disposition of mAbs.

Even with constant growing knowledge of these processes, it is still a challenge to understand and predict the PK of mAbs and to support the extrapolation from animal to human, areas which can gain insights from modeling and simulation. Empirical models are routinely used to analyze PK data of mAbs through research & development while the interest for mechanistic and physiologically-based PK (PBPK) models for mAbs is expending in order to get insight on their biodistribution, preferably at the biophase.

While it is common to use empirical 2-compartment models to analyze clinical PK data of mAbs, there is neither clear consensus nor guidance to, on one hand, identify and account for linear and non-linear components of the total clearance and on the other hand, interpret physiologically *and* mechanistically PK parameters [3, 41, 55, 64]. The mechanistic knowledge present in PBPK models is likely to support a more rational model selection in the empirical approach and thus, a methodology to link empirical and mechanistic PBPK modeling is desirable. However, PBPK models published for mAbs [66–74], are quite diverse in respect to the physiological distribution spaces to consider (vascular, interstitial, endosomal) and the parameterization of the non-specific elimination involving the neonatal Fc receptor (FcRn) and endogenous IgG (IgGendo). The more detailed the description of these processes, the more parameters are needed, yet their values are mostly unknown. The remarkable discrepancy between the simplicity of experimental plasma and tissue profiles and the complexity of published PBPK models translates in parameter identifiability issues.

In this thesis, we address this problem by developing a simplified PBPK model— derived from a hierarchy of more detailed PBPK models—that is consistent with the

current knowledge of processes governing the disposition of mAbs and in agreement with common biodistribution data of mAbs. Based on model reduction (lumping), we derive classical two-compartment models that are comparable to empirical models, yet retaining a mechanistic and physiological interpretation.

Integrating detailed processes at cellular and tissue levels in detailed PBPK models is highly valuable to gain insights in the most influential mechanisms in mAbs disposition. The detailed PBPK models that we developed for mAbs enable to study the relation between FcRn saturation level and steady-state endogenous IgG level and its impact on mAbs disposition. We demonstrate that binding to FcRn can be considered linear if (i) both mAb and endogenous IgG have comparable affinities to FcRn; and (ii) $\text{IgG}_{\text{mAb}} \ll \text{IgG}_{\text{endo}}$. This finding justifies, for the first time, simplification of detailed PBPK models for mAbs based on mechanistic considerations. The key step to substantially reduce the complexity (of the tissue model) is to implicitly consider the endosomal space and the FcRn-mediated salvage mechanism.

With the novel simplified parameterization of the tissue model, we are breaking new grounds in mechanistic modeling of mAbs disposition. In this thesis, we present the simplified PBPK model with extravasation rate-limited tissue distribution that (i) includes explicitly or implicitly the physiological processes relevant to describe mAbs disposition; (ii) is parameterized by a minimum number of parameters to allow stable parameter estimation; and (iii) allows reproducing typically observed characteristics of concentration-time profiles in plasma and tissues. We demonstrate that it is not possible to infer from common experimental data (only plasma, or plasma and tissue data) which tissues are involved in the unspecific elimination. We provide a new approach to predict tissue partition coefficients based on mechanistic insights: We directly link tissue partition coefficients (K_{tis}) to data-driven and species-independent antibody biodistribution coefficients (ABC_{tis}) recently published by Shah and Betts [18] and thus, we assure the extrapolation from pre-clinical species to human with the simplified PBPK model.

By extending the lumping approach from [91] to monoclonal antibodies, we identify which low-dimensional compartment models are consistent with the simplified PBPK model and experimental data. Hence, we provide a rational to guide empirical model development for analysis of mAbs PK data when we outline that a common interpretation of empirical two-compartment models for mAbs disposition—identifying the central compartment with the total plasma volume and the peripheral compartment with the interstitial space (or part of it)—is not consistent with current knowledge.

While the main focus of the thesis was to derive a simplified PBPK model to describe the disposition of mAbs in absence of target, we show here how to integrate

a target into the simplified PBPK model. The first results, based on simulation, support the statement in [71] that in the presence of a significant target mediated elimination pathway, the linear component of the total clearance plays a minor role in determining the disposition of monoclonal antibodies.

Empirical models are commonly used in late stage clinical development in the context of population analysis to identify covariates that contribute to explain observed inter-individual variability (IIV) in clinical PK data [27, 136–140]. Although most covariate models are likely to be motivated by mechanistic or (patho-)physiological considerations, a formal derivation from underlying mechanistic principles is rarely presented. In the literature, several approaches to model inter-individual variations in physiological parameters in PBPK models for small molecule drugs (SMDs) have been proposed [141–145]. The most relevant approaches, however, allowed only poorly to reproduce experimentally observed inter-individual variability.

In this thesis, we extend the lumping approach from [91] established for PBPK models for SMDs that integrate variability present in physiological and anatomical parameters typically used as covariates for the PK parameters in empirical models, e.g. clearance and volume of distribution. Individual parameter values are derived from reference physiological data which are corrected with scaling factors that account for additional individual characteristics, e.g. body height, body weight, lean-body weight, etc. From the extended lumping approach, we define a new mechanistic approach to covariate modeling that is applied to derive commonly used 2-compartment models describing the PK profiles of SMDs and that can directly be used in population analysis.

Given that clinical PK data of mAbs are greatly influenced by the interaction with the target and that the simplified PBPK model integrating a target requires further development and validation in pre-clinical species and human, we theoretically present the methodology to include IIV in the simplified PBPK models without a target that will serve as basis for future derivation of a lumping approach to support the development of low-dimensional compartment models for mAbs accounting for linear and non-linear clearances.

In conclusion, the work presented in this thesis greatly contributes to the expending field of mechanistic modeling of monoclonal antibodies disposition. The simplified PBPK model provides an integrative framework to integrate current knowledge on relevant processes governing mAbs disposition and to create new learnings on biodistribution peculiarities of monoclonal antibodies. With lumping methodology, the link is now established between physiologically-based pharmacokinetic and classical compartment models for mAbs providing guidance for model development and mech-

anistic interpretation of pharmacokinetic parameters for monoclonal antibodies in late stage clinical development.

APPENDIX

A

PBPK modeling of mAbs disposition

A.1 Software

MATLAB R2010a is used for modeling and simulation (ode15s solver). Parameter estimation is performed using the MATLAB optimization toolbox, version 4.2, and the predefined functions 'lsqcuvefit' using the Levenberg-Marquardt algorithm and 'fminsearch' which uses the simplex search method of Lagarias [172].

A.2 Mice experimental data for model development and evaluation

Experimental data of a murine monoclonal IgG1 antibody, 7E3, in FcRn-KO and WT mice, were extracted from [69] using the software DigitizeIt, version 1.5.8a, Bormann (2001-2006). 7E3 is an anti-platelet mAb with a high affinity for the human glycoprotein IIb/IIIa which does not bind to the murine glycoprotein IIb/IIIa [69]. The experimental data include measurements of 125I-labeled 7E3 after a single IV bolus dose of 8 mg/kg in FcRn-KO and WT mice in venous plasma, in lung, heart, kidney, muscle, skin, gut, spleen and liver. Additionally, the steady-state concentration of endogenous IgG in plasma was reported in [60, 104].

For model evaluation, experimental venous plasma data of a murine monoclonal IgG1 anti-CEA, T84.66, were extracted from [71]. T84.66 was administered intravenously to nude (20g) mice at three dose levels: 1, 10 and 25 mg/kg (n=4 per dose group).

A.3 *Detailed* PBPK model

A.3.1 Parameter estimation

Simulations that include both, monoclonal antibody 7E3 and endogenous IgG, are performed as follows: Endogenous IgG levels prior to 7E3 administration are determined by simulating the PBPK model with initial concentrations of 7E3 set to zero

Table A.1: *Detailed PBPK model for mAbs in mice: Parameters estimates*

Parameter		Reference		Description
k_{in}	1/day	1.75	fit	rate constant of endosomal uptake
k_{out}	1/day	2.91	fit	recirculation rate constant of FcRn-bound antibody
k_{deg}	1/day	0.06	fit	degradation rate constant of free antibody from endosomal space (tissue-specific)
FcRn	nM	1.48e5	fit	FcRn capacity
q_{prod}	nmol/day	2.09	fit	zero-order rate constant of endogenous IgG production

in all compartments. The resulting steady state levels of endogenous IgG serve as initial conditions for the simulations including 7E3 administration.

Since not all parameters are reported and following the same methodology as in [69], five of six unknown model parameters are estimated from the experimental plasma data, given the detailed PBPK model including the brain tissue, as stated in eqs. (3.1) - (3.5). The parameters are the total FcRn capacity $FcRn_{tot}$, the rate constant of uptake into the endosomal compartment k_{in}, the outflow rate constant from the endosomal compartment k_{out}, the degradation rate constant k_{deg}, and the zero-order production rate of endogenous IgG q_{prod} (see Fig. 3.1 for an overview of all model parameters). We further assume $FcRn_{tot}$, k_{in}, k_{out}, and k_{deg} to be tissue-independent. Tissue-specific clearances are obtained as follows:

$$CL_{e,tis} = k_{deg} \cdot V_{e,tis},$$

where $V_{e,tis}$ is the tissue-specific volume of the endosomal space. The sixth unknown parameter is the fraction of recirculated bound antibody FR. It is set to FR = 0.715, as published in [69]. A different approach has demonstrated that the PBPK model is robust to changes of FR values and that its exact value does not influence outcomes of PBPK model simulations and further derivations [173, Sec. 2.4.1, p. 50, and Appendix B.5.2, p. 91].

The unknown parameters are estimated using a two-step approach. In the first step, k_{in} is estimated thanks to the FcRn-KO data for the mAb only; no plasmatic concentration of endogenous IgG in FcRn-KO mice has been reported to date. In the knockout scenario, the recirculation of mAb/IgGendo is prevented since no binding to FcRn takes place which is necessary for exporting mAb/IgGendo out of the endosomal space. Therefore, solely the disappearance of mAb/IgGendo due to the uptake from vascular and interstitial spaces into the endosomal space is reflected by the experimental KO-plasma data. In the second step, the remaining parameters i.e. k_{out}, k_{deg}, $FcRn_{tot}$ and q_{prod} are estimated simultaneously using plasma concentrations of mAb and IgGendo in the WT mice. The parameter values are reported in Tab. A.1.
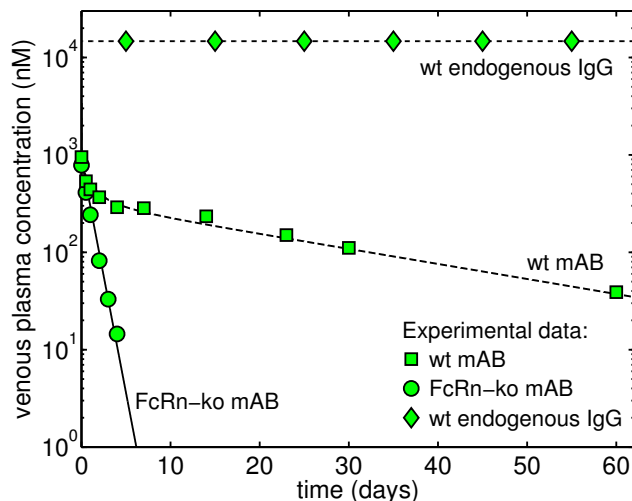
Figure A.1: *Predictions of plasma concentration-time profiles of mAb 7E3 after an IV bolus administration of 8 mg/kg in wild-type (wt) and FcRn-knockout (FcRn-ko) mice (exp. data extracted from [69]) and steady-state plasma concentrations of endogenous IgG as reported in wild-type mice [60, 104?].*

A.3.2 Insight on parameter identifiability

The model predictions of the plasma concentrations, based on the estimated parameters reported in Tab. A.1, are presented in Fig. A.1. The simulated concentration-time profiles in plasma agree very well with the experimental data of the mAb 7E3 after a single IV bolus dose of 8 mg/kg in wild-type and FcRn-knockout mice and with the steady-state concentration of endogenous IgG in wild-type mice.

However, the model fails to reproduce accurately the tissue concentration-time profiles (data not shown). Figure A.2 depicts the simulated steady state level of IgGendo in the different endosomal spaces. For the specific well-perfused organs, i.e lung, liver, spleen and kidney, the endosomal concentrations of total IgGendo are above the threshold of solubility commonly reported, 100 - 150 mg/mL or 6.5e5 - 1e6 nM [174–178].

One attempt to circumvent the failure of the detailed PBPK model to accurately describe the plasma and tissue data of the mAb 7E3 is to estimate the unknown parameters in regards to all data. However, it is that either the estimation step fails or one can estimate a set of parameters allowing to describe plasma data but poorly tissue data or a different set of parameters allowing to describe tissue data but poorly plasma data. Clearly, the detailed PBPK model is over-parameterized given the information embedded in the experimental data and the current knowledge of processes governing the biodistribution of IgGs.
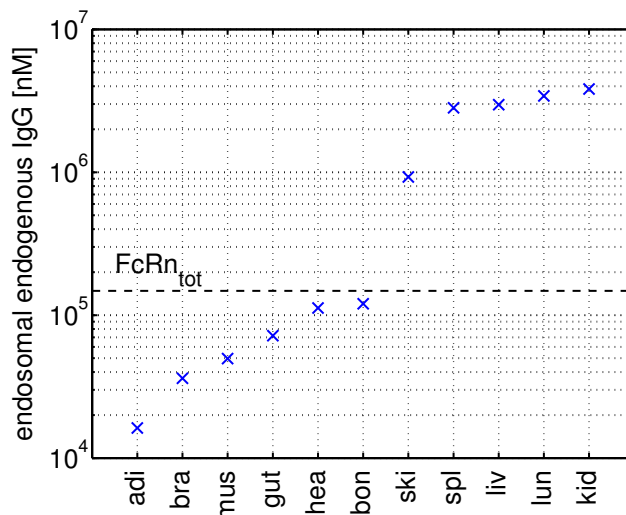
Figure A.2: *Predicted total endogenous concentration in the different endosomal spaces based on a plasma steady state concentration of endogenous* $\text{IgG}_{\text{tot}} = 1.47e4$ *nM [104]. The dashed line corresponds to the total FcRn concentration as given in Table 4.1.*

A.4 *Intermediate* PBPK model

A.4.1 Parameter estimation

Model fitting is performed using the MATLAB optimization toolbox, version 4.2, and the predefined function 'lsqcuvefit' using the Levenberg-Marquardt algorithm. The maximum change in variables for finite-difference gradients was set to 0.001 and the maximum number of functions allowed to be evaluated was set to 5000.

Given the new parameterization of the tissue model, the 21 unknown parameters in WT mice are estimated by fitting the intermediate PBPK model stated in eqs. (3.20)-(3.24) to experimental plasma and tissue data in mice for the mAb, 7E3. The experimental data are treated as described in appendix A.2. The unknown parameters are (i) the rate constant of uptake in the endosomal space, k_{in}; (ii) the tissue-specific endosomal intrinsic clearance, CLint_{e}; (iii) the tissue-specific total FcRn-mediated outflow from the endosomal space, Q_{out}. We further assume that k_{in} is tissue-independent. The fraction of recirculated bound antibody is set to FR = 0.715, as published in [69].

The parameters are estimated following a two-step approach. Firstly, k_{in} is estimated using the venous plasma data in FcRn-KO mice, setting all Q_{out} to 0. In FcRn-KO mice, recirculation of mAb is prevented since no binding to FcRn takes place which is necessary for exporting mAb from the endosomal space. Therefore, solely the disappearance of mAb due to its uptake from plasma and interstitial into

endosomal spaces is reflected in FcRn-KO plasma data. In the following step, k_{in} is fixed to its estimated value. The PBPK model is fitted to WT plasma and tissue data to estimate $CLint_{e,wt}$ and Q_{out}, in WT mice. While the focus is indeed to develop a PBPK model in WT mice to further extrapolate to other species, i.e. non-human primates (NHPs) and human, one can also estimate $CLint_{e,ko}$, for FcRn-KO mice. They are obtained by fitting the intermediate PBPK model to the FcRn-KO tissue data. In FcRn-KO mice, $CLint_{e,ko}$ represents the maximum clearance due to the lysosomal degradation.

A.4.2 Model performance

The intermediate PBPK model is fitted to plasma and tissue data of the mAb 7E3 after an IV bolus administration to FcRn-KO and WT mice. The parameter estimation is highly sensitive to initial values and several set of parameters could accurately characterize the venous plasma data as well as the organ/tissue data after correction by the residual blood (for details, see appendix A.5). The rate constant of endosomal uptake kin is estimated to be 1.65 /day. Tissue-dependent parameters, i.e. $CLint_{e,wt}$ and Q_{out} in WT mice and $CLint_{e,ko}$ for FcRn-KO mice are reported in Table A.2. The resulting venous plasma and tissue predictions are shown in Fig. A.3. *However, it is recommended to read and interpret these results with caution, in regards to the comment above made on the high sensitivity to initial values and the high likelihood that another set of parameters could describe the data equally well* as those reported in Table A.2.

In absence of FcRn, the IgGs present in the endosomal space cannot undergo the salvage process mediated by FcRn and therefore are entirely cleared by proteolytic degradation in the lysosomes. $CLint_{e,ko}$, in KO mice, accounts for the maximum linear clearance solely due to the lysosomal degradation. The fraction unbound in the endosome, fu, is deduced from the ratio of the clearance in WT to the clearance in KO mice:

$$fu = \frac{CLint_{e,wt}}{CLint_{e,ko}},$$

fu values are reported in Table A.2. For all tissues, the fraction unbound for 7E3 remains lower than 0.6, indicating that FcRn is not saturated.

A.5 Correction for residual blood

As it is expected for any low volume of distribution drug, residual blood can have a major impact on experimentally measured tissue concentration [113, Table III, p. 105].
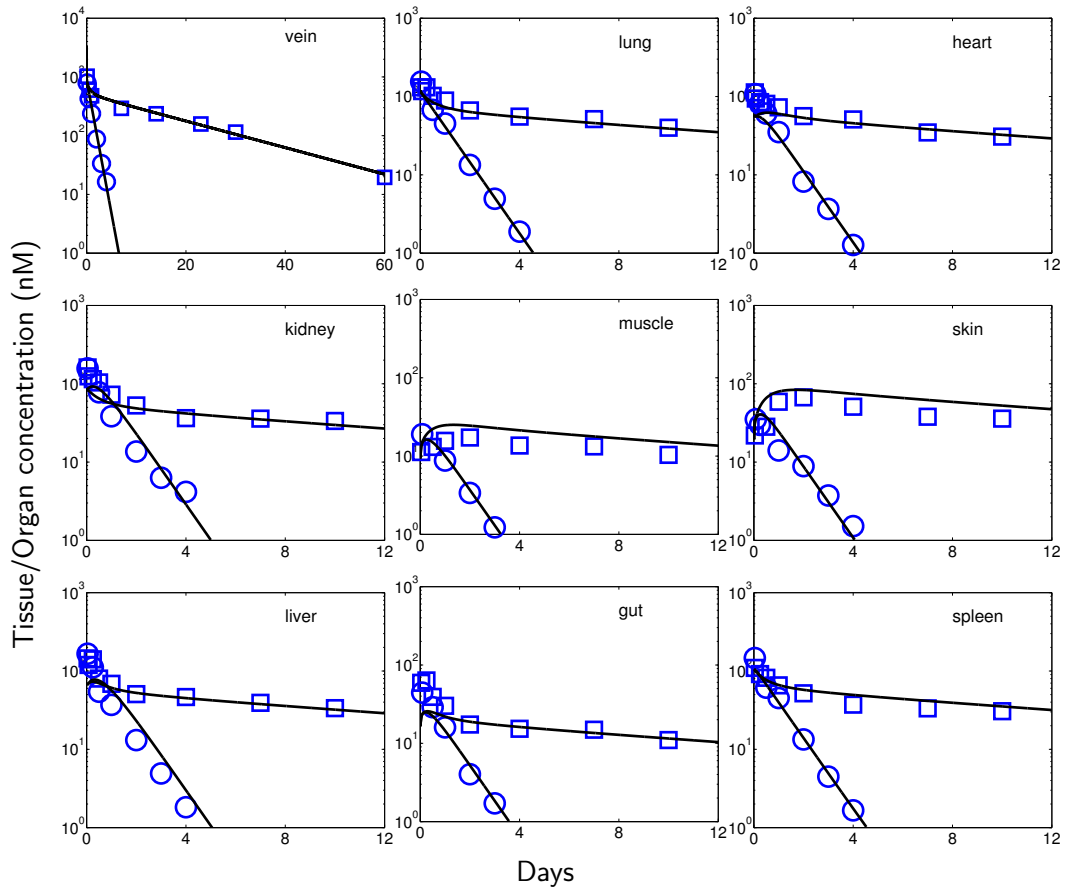
Figure A.3: *Predictions of venous plasma and tissue concentration-time profiles vs. observed concentrations in WT (blue square) and FcRn-KO mice (blue rounds) of mAb 7E3 after an IV bolus administration of 8 mg/kg, based on the intermediate PBPK model. The data are represented as mean data and were extracted from [69].*

Table A.2: *Intermediate PBPK model for mAbs in mice: Parameter estimates*

	Q_{out} (10^{-6}ml/min)	$CLint_{e,wt}$ (10^{-6}ml/min)	$CLint_{e,ko}$ (10^{-6}ml/min)	fu_{tis} -
Lung	18.175	0.0173	15.555	0.001
Adipose	16.083	0.277	6.944	0.040
Bone	1.405	0.641	6.113	0.105
Gut	53.560	5.351	47.260	0.113
Heart	0.026	1.004	1.685	0.597
Kidney	24.570	0.032	2.933	0.011
Liver	17.602	0.194	7.773	0.025
Muscle	37.496	0.772	97.910	0.008
Skin	11.174	0.985	45.306	0.022
Spleen	25.278	0.069	5.758	0.012
Artery	-	-	-	-
Vein	-	-	-	-

We parameterize the PBPK models in such a way that predictions are independent of residual blood. Instead, correction for residual blood is a post-simulation step.

We denote the residual blood volume related to a given tissue by $V_{res,blo}$ and the tissue volume including residual blood by

$$V_{exp} = V_{tis} + V_{res,blo}.$$

The subscript tis in V_{exp} and other parameters is omitted to keep notation simple. Data on residual blood are typically reported in terms of some ratio relating residual blood to tissue volume or weight. Here, we use the ratio res_{blo} of residual blood volume to blood-contaminated tissue volume, i.e.,

$$res_{blo} = \frac{V_{res,blo}}{V_{exp}};$$

see Table 4.2 for experimentally determined ratios in mice. Based on V_{exp}, we determine the residual blood volume according to $V_{res,blo} = res_{blo} \cdot V_{exp}$.

Denoting by A_{res} the amount of drug in the residual blood yields

$$V_{res,blo} \cdot C_{blo} = A_{res} = V_{res,pla} \cdot C_{pla},$$

where the residual plasma volume is obtained using the hematocrit (hct) via $V_{res,pla} = (1-\text{hct})V_{res,blo}$. The residual blood-contaminated tissue concentration C_{exp} is defined as

$$C_{exp} = \frac{V_{tis} \cdot C_{tis} + V_{res,pla} \cdot C_{pla}}{V_{exp}}. \tag{A.1}$$

Hence, based on the prediction of C_{pla} and C_{tis} by the PBPK model, we can directly predict C_{exp} based on the above equation. If experimental data have already been corrected for residual blood, the PBPK model does not need to be altered.

B

PBPK modeling of SMDs disposition

B.1 Software

MATLAB R2010b (version 7.5) is used for modeling & simulation and R (version 2.12.0) for statistical analysis.

B.2 Algorithm for creating a virtual population

BH is assumed normally distributed with mean μ_{BH} and standard deviation σ_{BH}, i.e.,

$$\mathrm{BH} \sim \mathcal{N}(\mu_{\mathrm{BH}}, \sigma_{\mathrm{BH}}^2).$$

We further assume that BMI is log-normally distribution with parameters μ_{BMI} and σ_{BMI}^2, i.e.,

$$\mathrm{BMI} \sim \ln\mathcal{N}(\hat{\mu}_{\mathrm{BMI}}, \hat{\sigma}_{\mathrm{BMI}}^2).$$

Both assumptions are in line with the NHANES study [179]. In this study, the difference between a normal and a log-normal distribution for BH of Caucasians is negligible; so alternatively, one might also assume a log-normal distribution for BH. In the NHANES study, BH and BMI are weakly correlated, so assuming these two covariates as uncorrelated seems a reasonable approximation.

To generate a virtual population in terms of N pairs of $(\mathrm{BH}, \mathrm{BW})$ of a given sex, we require the parameters μ_{BH}, σ_{BH}, μ_{BMI} and σ_{BMI} as input. The work flow to generate a single pair of BH and BW is the following:

1. Sample a BH value from $\mathcal{N}(\mu_{\mathrm{BH}}, \sigma_{\mathrm{BH}}^2)$.

2. Sample a BMI value from $\ln\mathcal{N}(\hat{\mu}_{\mathrm{BMI}}, \hat{\sigma}_{\mathrm{BMI}}^2)$. If only a descriptive statistics on BMI is available (rather than on log BMI), sample a transformed $\widehat{\mathrm{BMI}}$ value from the normal distribution $\mathcal{N}(\hat{\mu}_{\mathrm{BMI}}, \hat{\sigma}_{\mathrm{BMI}}^2)$ with mean and variance

$$\hat{\mu}_{\mathrm{BMI}} = \log\left(\frac{\mu_{\mathrm{BMI}}^2}{\sqrt{\mu_{\mathrm{BMI}}^2 + \sigma_{\mathrm{BMI}}^2}}\right), \quad \hat{\sigma}_{\mathrm{BMI}}^2 = \log\left(\frac{\sigma_{\mathrm{BMI}}^2}{\mu_{\mathrm{BMI}}^2} + 1\right),$$

where μ_{BMI} and σ_{BMI} denote the mean and standard deviation of the descriptive statistics. Finally, set $\mathrm{BMI} = \exp(\widehat{\mathrm{BMI}})$.

3. Finally, determine BW according to

$$\mathrm{BW} = \mathrm{BH}^2 \cdot \mathrm{BMI}.$$

The above steps are repeated N times. For example, to create a virtual population with the characteristics of the autopsy study [163] listed in Table 7.3, we choose for the male adults: $n = 355$, $\mu_{\mathrm{BH}} = 1.72$ [m], $\sigma_{\mathrm{BH}} = 0.075$ [m], $\mu_{\mathrm{BMI}} = 22.8$ [kg/m^2] and $\sigma_{\mathrm{BMI}} = 3.3$ [kg/m^2]. The above algorithm enforces a correlation between BH and BW, as observed in the NHANES study [179].

Given the ensemble of N individual (BH, BW) pairs, we use the LBW-scaling approach together with the parameters of the reference adult (Table 7.2+7.1) and the compound specific input (Table 3 in [91]) to generate all parameters required to parameterize the generic PBPK model.

B.3 Determining the individual blood-to-plasma ratio

Given sex and age dependent changes in binding protein concentrations [159–161], the fraction unbound in plasma fuP was considered a potentially age/sex dependent parameter. It was assumed that BP was measured in healthy male adults (ad/m). Using this values we determined the erythrocyte-to-unbound plasma partition coefficient $K\mathrm{u}_e$ from

$$K\mathrm{u}_e = \frac{\mathrm{BP}_{(\mathrm{ad/m})} - (1 - \mathrm{hct}_{(\mathrm{ad/m})})}{\mathrm{hct}_{(\mathrm{ad/m})} \cdot \mathrm{fuP}_{(\mathrm{ad/m})}}.$$

Assuming $K\mathrm{u}_e$ to be age/sex-independent, we determined the age/sex-specific blood-to-plasma ratio for other age classes by

$$\mathrm{BP} = \mathrm{hct} \cdot K\mathrm{u}_e \cdot \mathrm{fuP} + (1 - \mathrm{hct}).$$

B.4 Allometric scaling approach

A common approach for extrapolation of classical compartment models from adults to children is based on allometric scaling see, e.g., [147] and references therein. Most body size relations take the form

$$Y = a \cdot \mathrm{BW}^b,$$

where Y is the biological characteristic to be predicted, BW is the body weight, and a and b are empirically derived constants. Following Table 1 in [147], the exponent is $b = 1$ for volumes & organ weights, and $b = 3/4$ for cardiac output, blood flows and

clearances. Allometric scaling from a reference adult (with body weight BW_{adult} and parameters V_{adult}, Q_{adult}, and CL_{adult}) to a child of body weight BW yields:

$$V = \left(\frac{V_{adult}}{BW_{adult}}\right) \cdot BW$$

and

$$Q = \left(\frac{Q_{adult}}{BW_{adult}^{3/4}}\right) \cdot BW^{3/4}, \qquad CL = \left(\frac{CL_{adult}}{BW_{adult}^{3/4}}\right) \cdot BW^{3/4}.$$

Bibliography

[1] P. Ehrlich. *Beiträge zur Theorie und Praxis der histologischen Färbung*. PhD thesis, Universität Leipzig, 1878. 1

[2] N.L. Dirks and B. Meibohm. Population pharmacokinetics of therapeutic monoclonal antibodies. *Clinical Pharmacokinetics*, 49(10):633–659, 2010. 1, 9, 71

[3] R. Keizer, A.D.R. Huitema, J.H.M. Schellens, and J.H. Beijnen. Clinical Pharmacokinetics of Therapeutic Monoclonal Antibodies. *Clinical Pharmacokinetics*, 49:493–507, 2010. 1, 9, 15, 32, 53, 89, 97

[4] W.D. Morell, A. Terry and T. Waldman. Metabolic properties of IgG subclasses in man. *Journal of Clinical Investigation*, 49(4):673–680, 1970. 1

[5] W.F. Richter, S.G. Bhansali, and M.E. Morris. Mechanistic determinants of biotherapeutics absorption following SC adnministration. *The AAPS Journal*, 14(3):559–570, 2012. 2

[6] B. Rippe and B. Haraldsson. Transport of macromolecules accross microvascular walls: the two-pore theory. *Physiological reviews*, 1:163–219, 1994. 2, 11, 12

[7] H. Wiig and O. Tenstad. Interstitial exclusion of positively and negativerly charged IgG in rat skin and muscle. *American journal of Physiology Heart and Circulatory Physiology*, 280:H1505–H1512, 2001. 1, 65, 72

[8] R.R. Porter. Structural studies of immunoglobulins. *Science*, 180(4087):713–716, 1973. 1

[9] G.M. Edelman. Antibody structure and molecular immunology. *Science*, 180(4088):830–840, 1973.

[10] P.J. Capel. Heterogeneity of human IgG Fc recpetors. *Immunomethods*, 4(1):25–34, 1994. 1, 3

[11] T.A. Waldman and W. Strober. Metabolism of immunoglobulins. *Progress in Allergy*, 13:1–110, 1969. 1

[12] S.A. Peters. *Physiologcally-based pharmacokinetic (PBPK) modeling and simulations: Principels, methods, and applications to pharmaceutical industry*, chapter

Chapter 10: Physiologically-based pharmacokinetics of biotherapeutics, pages 209–259. Wiley, 2012. 2

[13] T.N. Tozer and M. Rowland. *Introduction to Pharmacokinetics and Pharmacodynamics.* Lippincott Williams & Wilkins, 2006. 2, 3, 4

[14] CJ. Porter and S.A. Charman. Lymphatic transport of proteins after subcutaneous administration. *Journal of Pharmaceutical Sciences*, 89(3):297–310, 2000. 2

[15] CJ. Porter, G.A. Edwards, and S.A. Charman. Lymphatic transport of proteins after s.c. injection: implications of animal model selection. *Advanced Drug Delivrey Reviews*, 50:157–171, 2001. 2

[16] M.A. Swartz. The physiology of the lymphatic system. *Advanced Drug Delivrey Reviews*, 50:3–20, 2001. 2, 90

[17] F. Brambell, W. Hemmings, and I. Morris. A theoretical model of gamma-globulin catabolism. *Nature*, 203:1352–1355, 1964. 3

[18] D.K. Shah and A.M. Betts. Antibody biodistribution coefficients: Inferring tissue concentrations of monoclonal antibodies based on the plasma concentrations in several preclinical species and human. *mAbs*, 5:2:297–305, 2013. 3, 9, 41, 46, 47, 50, 51, 61, 72, 98

[19] M. Dostalek, I. Gardner, B. M. Gurbaxani, R.H. Rose, and M. Chetty. Pharmacokinetics, pharmacodynamics and physiologically-based pharmacokinetic modelling of monoclonal antibodies. *Clinical Pharmacokinetics*, 52:83–124, 2013. 3, 4, 9

[20] M. Raghavan, V.R. Bonagura, S.L. Morrison, and P.J. Bjorkman. Analysis of the pH dependence of the neonatal Fc receptor/immunoglobulin G interaction using antibody and receptor variants. *Biochemistry*, 34:14649Ű57, 1995. 4

[21] S. Popov, J.G. Hubbard, J.K. Kim, B. Ober, V. Ghetie, and E.S. Ward. The Stoichiometry and Affinity of the Interaction of Murine Fc Fragments with the MHC Class I-Related Receptor, FcRn. *Molecular Immunology*, 33(6):521–530, 1996. 4, 21

[22] V. Ghetie, J.G. Hubbard, M-F. Kim, J-K.and Tsen, Y. Lee, and E.S. Ward. Abnormally short serum half-lives of IgG in 2-microglobulin-deficient mice. *European Journal of Immunology*, 26:690–696, 1996. 43

[23] V. Ghetie and S. Ward. Multiple roles for the major histocompatibility complex class-I related receptor FcRn. *Annual Review of Immunology*, 18:739–766, 2000.

[24] K. Kim, W.L. Hayton, J.M Robinson, and C.L. Anderson. Kinetics of FcRn-mediated recycling of IgG and albumin in human: Pathophysiology and therapeutic implications using a simplified mechanism-based model. *Clinical Immunology*, 122(2):146Ŭ155, 2007. 4

[25] F. Nimmerjahn and J.V. Ravetch. Fcγ recptors: old friends and new family members. *Immunity*, 24(1):19–28, 2006. 3

[26] M.A. Tabrizi and L.K. Roskos. *Phrmacokinetics and Pharmacodynamics of biothech drugs: Principles and case studies in drug development*, chapter Exposure-response relationships for therapeutic biologic products, pages 295–330. Wiley-VCH Verlag, 2006. 3

[27] B. Sheiner and J.-L. Steimer. Pharmacokinetic/Pharmacodynamic Modeling in Drug Development. *Annual Review of Pharmacology and Toxicology*, 40:67–95, 2000. 3, 4, 75, 95, 99

[28] B. Meibohm and M. Derendorf. Pharmacokinetic/pharmacodynamic studies in drug product development. *Journal of Pharmaceutical Sciences*, 91(1):18–31, 2002. 95

[29] C.F. Burman, B. Hamren, and P. Olsson. Modelling and simulation to improve decision-making in clinical development. *Pharmaceutical Statistics*, 4:47–58, 2005.

[30] K.G. Lalonde, R.L. andKowalski, M.M. Hutmacher, W. Ewy, D.J. Nichols, B.W. Milligan, P.A.and Corrigan, S.A. Lockwood, P.A.and Marshall, L.J. Benincosa, T.G. Tensfeldt, K. Parivar, P. Amantea, M. asnd Glue, H. Koide, and R. Miller. Model-based Drug Development. *Clinical Pharmacology and Therapeutics*, 82:21–32, 2007. 5, 95

[31] H.M. Jones, I.B. Gardner, and K.J. Watson. Modelling and PBPK simulation in drug discovery. *The AAPS Journal*, 11(1):155–166, 2009. 75

[32] H. Derendorf, L.J. Lesko, P. Chaikin, W.A. Colburn, P. Lee, R. Miller, R. Powell, G. Rhodes, D. Stanski, and J. Venitz. Pharmacokinetic/Pharmacodynamic modeling in drug research and development. *Journal of Clinical Pharmacology*, 40:1399–1418, 2000.

[33] L.Z. Benet. *Pharmacokinetics: Basic principles and its use as a tool in drug metabolism.* Drug metabolism and drug toxicity, Rave press New-York, 1984. 3

[34] R.D. Schoenwald. *Pharmacokinetics in drug discovery and development.* Pharmacokinetics in drug discovery and development, 2002. 3, 4

[35] N. Parrott, H. Jones, and T. Paquereau, N. Lavé. Application of full physiological models for pharmaceutical drugs candidate selection and extrapolation of pharmacokinetics to man. *Journal of Pharmacology & Toxicology*, 96:193–199, 2005. 4

[36] B. Sheiner. Learning versus confirming in clinical drug development. *Clinical Pharmacology and Therapeutics*, 61:275–291, 1997. 95

[37] J. Gabrielsson and D. Weiner. *Pharmacokinetic and Pharmacodynamic data analysis: Concepts and Applications.* 2000. 9

[38] P.L. Bonate. *Pharmacokinetic-Pharmacodynamic Modeling and Simulation.* Springer-Verlag, New York, 2nd edition edition, 2011. 5, 75

[39] T. Lavé, N. Parrott, H.P. Grimm, A. Fleury, and M. Reddy. Challenges and opportunities with modelling and simulation in drug discovery and drug development. *Xenobiotica*, 37:1295–1310, 2007. 4, 6

[40] S. Zhao and R. Iyengar. Systems Pharmacology: network analysis to identify multiscale mechanisms of drug action. *Annual Review of Pharmacology and Toxicology.*, 52:505–521, 2012. 5

[41] H.M. Jones, K. Mayawala, and P. Poulin. Dose selection based on physiologically based pharmacokinetic (PBPK) approaches. *The AAPS Journal*, 15(2):377–387, 2013. 8, 15, 50, 97

[42] K. Luu, E. Kraynov, B. Kuang, P. Vicini, and WZ. Zhong. Modeling, simulation, and translation framework for the preclinical development of monoclonal antibodies. *The AAPS Journal*, 15(2):551–558, 2013. 5

[43] E. Nelson. Kinetics of drug absorption, distribution, metabolism and excretion. *Journal of Pharmaceutical Sciences*, 50:181–192, 1961. 4

[44] J. Gabrielsson and D. Weiner. Non-compartmental analysis. *Computational Toxicology Methods in Molecular Biology*, 929:377–389, 2012. 5

[45] J. Bulitta and N.H.G. Holford. An introductory guide to non-compartmental analysis. *Wiley Encyclopedia of Clinical Trials*, pages 1–21, 2008. 5, 9

[46] B. Hood and H. Derendorf. The impact of systems approaches on biological problems in drug discovery. *Nature Biotechnology*, 22:1215–1217, 2004. 6

[47] P.H. Van der Graaf and N. Benson. Systems pharmacology: bridging systems biology and pharmacokinetics-pharmacodynamics (PKPD) in drug discovery and development. *Pharmaceutical Research*, 28:1460–1464, 2011.

[48] M. Rowland, C. Peck, and G. Tucker. Physiologically-based pharmacokinetics in drug development and regulatory science. *Annual Review of Pharmacology and Toxicology*, 51:45–73, 2011. 6, 75

[49] H.M. Jones, N. Parrott, K. Jorga, and T. Lavé. A novel strategy for physiologically based predictions of human pharmacokinetics. *Clinical Pharmacokinetics*, 45(5):511–542, 2006. 8

[50] M. Danhof, J. De Jongh, E. De Lange, O. Della Pasqua, B.A. Ploeger, and R.A. Voskuyl. Mechanism-based pharmacokinetic-pharmacodynamic modeling: Biophase distribution, receptor theory, and dynamical systems analysis. *Annual Review of Pharmacology and Toxicology*, 47:357–400, 2007. 6

[51] C. Lüpfert and A. Reichel. Development and Application of Physiologically Based Pharmacokinetic Modeling Tools to Support Drug Discovery. *Chemistry and Biodiversity*, 2:1462–1486, 2005. 6

[52] L.E. Gerlowski and R.K. Jain. Physiologically Based Pharmacokinetic Modeling: Principles and Application. *Journal of Pharmaceutical Sciences*, 72(10):1103–1127, 1983.

[53] I.A. Nestorov. Whole Body Pharmacokinetic Models. *Clinical Pharmacokinetics*, 42(10):883–908, 2003. 6, 8

[54] M. Bouvier d'Yvoire, M. Prieto, B.J. Baauboer, F.Y. Bois, A. Boobis, C. Brochot, S. Coecke, A. Freidig, U. Gundert-Remy, T. Hartung, M.N. Jacobs, T. Lavé, D.E. Leahy, H. Lennernäs, G.D. Loizou, B. Meek, M. Pease, M. Rowland, M. Spendiff, J. Yang, and M. Zeilmaker. Physiologycally-based kinetic modelling (PBPK modelling): Meeting the 3Rs agenda. *ATLA*, 35:661–671, 2007. 8

[55] Y. Vugmeyster, X. Xu, FP. Theil, L.A. Khawli, and M.W. Leach. Pharmacokinetics and toxicology of therapeutic proteins: Advances and challenges. *World Journal of Biological Chemistry*, 3(4):73–92., 2012. 9, 15, 97

[56] C. Starr and S. Taggart. *Biology: The unity and diversity of life.* Brooks/Cole, 1989. 9

[57] D.W.A. Bourne. *Mathematical Modeling of Pharmacokinetic Data.* Technomic Publishing Company, Inc., 1995. 9

[58] L Michaelis and M.L. Menten. Die Kinetik der Invertinwirkung. *Biochemestry Zeitung*, 49:333–369, 1913. 9, 63, 71

[59] J. Wagner. Properties of the Michaelis-Menten equation and its integrated form which are useful in pharmacokinetics. *Journal of Pharmacokinetics and Biopharmaceutics*, 1:103–121, 1973. 9

[60] R.J. Hansen and J.P. Balthasar. Pharmacokinetic/Pharmacodynamic modeling of the effects of intravenous immunoglobulin on the disposition of antiplatelet antibodies in a rat model of immune thrombocytopenia. *Journal of Pharmaceutical Sciences*, 92(6):1206–1215, 2003. 9, 10, 12, 25, 31, 45, 103, 105

[61] Y. Zheng, H. Scheerens, J.C. Davis Jr, R. Deng, S.K. Fischer, C. Woods, P.J. Fielder, and E.G. Stefanich. Translational pharmacokinetics and pharmaco-dynamics of an FcRn-variant anti-CD4 monoclonal antibody from preclinical model to phase I study. *Clinical Pharmacology and Therapeutics*, 89(2):283–289, 2011. 10

[62] J.T. Andersen, R. Pehrson, V. Tolmachev, M.B.D. Daba, L. Abrahmsen, and C. Ekblad. Extending half-life by indirect targeting of the neonatal Fc receptor (FcRn) using a minimal albumin binding domain. *The Journal of Biological Chemistry*, 286:5234–5241, 2011.

[63] A. Datta-Mannan, D.R. Witcher, Y. Tang, J. Watkins, and V.J. Wroblewski. Monoclonal antiboy clearance: impact od modulating the interaction of IgG with the neonatal Fc receptor. *The Journal of Biological Chemistry*, 282(3):1709–1717, 2007. 10

[64] JJ Xiao. Pharmacokinetic models for FcRn-Mediated IgG disposition. *Journal of Biomedicine and Biotechnology*, 2012:282989, 2012. 10, 15, 25, 31, 32, 45, 97

[65] BF. Krippendorff, DA. Oyarzún, and Huisinga W. Predicting the F(ab)-mediated effect of monoclonal antibodies in vivo by combining cell-level kinetic and pharmacokinetic modelling. *Journal of Pharmacokinetics and Pharmacody-namics*, 39(2):125–139., 2012. 10, 15, 63, 67, 71

[66] D.G. Covell, J. Barbet, O.D. Holton, C.D.V. Black, RJ Parker, and J.N. Weinstein. Pharmacokinetics of monoclonal immunoglobulin G_1, $F(ab')_2$, and Fab' in mice. *Cancer Research*, 46(8):3969–3978, 1986. 11, 12, 15, 21, 30, 39, 41, 90, 97

[67] L.T. Baxter, H. Zhu, D.G. Mackensen, and R.K. Jain. Physiologically-based pharmacokinetic model for specific and nonspecific monoclonal antibodies and fragments in normal t and Human tumor xenografts in nude mice. *Cancer Research*, 54:1517–1528, 1994. 11, 12, 19, 20, 22, 34, 38, 39, 40, 50, 93

[68] G.Z. Ferl, A.M. Wu, and J.J. Distefano. A predictive model of therapeutic monoclonal antibody dynamics and regulation by the neonatal Fc receptor (FcRn). *Annals of Biomedical Engeneering*, 33(11):1640–1652, 2005. 11, 21

[69] A. Garg and J.P. Balthasar. Physiologically-based pharmacokinetic (PBPK) model to predict IgG tissue kinetics in wild-type and FcRn-knockout mice. *Journal of Pharmacokinetics and Pharmacodynamics*, 34:687–709, 2007. 12, 13, 17, 19, 20, 21, 22, 28, 29, 30, 33, 34, 36, 38, 39, 40, 41, 42, 49, 54, 90, 103, 104, 105, 106, 108

[70] J.P. Davda. A physiologically based pharmacokinetic (PBPK) model to characterize and predict the disposition of monoclonal antibody CC49 and its single chain Fv constructs. *International Immunopharmacology*, 8:401–413, 2008. 12, 19, 50

[71] S.R. Urva, C.Y. Yang, and J.P. Balthasar. Physiologically based pharmacokinetic model for T84.66: A monoclonal anti-CEA antibody. *Journal of Pharmaceutical Sciences*, 99(3):1582–1600, 2010. 13, 21, 33, 39, 43, 49, 72, 99, 103

[72] Y. Chen and J.P. Balthasar. Evaluation of a catenary PBPK model for predicting the in vivo disposition of mAbs engineered for high-affinity binding to FcRn. *The AAPS Journal*, 14(4):850–859, 2012. 13, 90

[73] D.K. Shah and A.M. Betts. Towards a platform PBPK model to characterize the plasma and tissue disposition of monoclonal antibodies in preclinical species and human. *Journal of Pharmacokinetics and Pharmacodynamics*, 39:67–86, 2012. 13, 21, 32, 33, 36, 38, 49

[74] Y. Cao, J. P. Balthasar, and W. J. Jusko. Second-generation minimal physiologically-based pharmacokinetic model for monoclonal antibodies. *Journal of Pharmacokinetics and Pharmacodynamics*, 40(5):597–607, 2013. 11, 14, 15, 64, 66, 90, 97

[75] B. Davies and T. Morris. Physiological parameters in laboratory animals and humans. *Pharmaceutical Research*, 10:1093–1095, 1993. 11, 20, 22, 38, 41

[76] R.B. Sothern and S.A. Gruber. Further commentary: Physiological parameters in laboratory animals and human. *Pharmaceutical Research*, 11(2):349–350, 1994. 11

[77] T. Fukumoto and M.R. Brandon. Importance of the liver in immunoglobulin catabolism. *Research in Veterinary Science*, 32:62–69, 1982. 12

[78] J. Borvak, J. Richardson, C. Medesan, F. Antohe, C. Radu, C. Simionescu, V. Ghetie, and Ward E.S. Functional expression of the MHC class I-related receptor, FcRn, in endothelial cells of mice. *International Immunology*, 10(9):1289–1298, 1998. 12, 47, 48, 90

[79] F. Antohe, L. Radulescu, A. Gafecu, V. Ghetie, and M. Simionescu. Expression of functionnally active FcRn and the differenciated biderectinal transport of IgG in human placenta endothelial cells. *Human Immunology*, 62:93–105, 2001. 12

[80] A. Praetor, I. Ellinger, and W. Hunziker. Intracellular traffic of the MHC class I-like IgG Fc receptor, FcRn, expressed in epithelial MDCK cells. *Journal of Cell Science*, 112(14):2291–2299, 1999.

[81] E.D. Lobo, R.J. Hansen, and J.P. Balthasar. Antibody pharmacokinetics and pharmacodynamics. *Journal of Pharmaceutical Sciences*, 93(11):2645–2648, 2004. 12, 71

[82] J. Zhou, J.E. Johnson, V. Ghetie, R.J. Ober, and Ward. Generation of mutated variants of the human form of the MHC class I-related receptor, FcRn, with increased affinity for mouse immunoglobulin G. *Journal of Molecular Biology*, 332:901–913, 2003. 12

[83] C.R. Hopkins and I.S. Trowbridge. Internalization and processing of transferrin and the transferrin receptor in human carcinoma A431 cells. *Journal of Cell Biology*, 97(2):508–521, 1983. 13

[84] P.F. Davies and R. Ross. Mediation of Pinocytosis in cultured arterial smooth muscle and endothelial cells by platelet-derived growth factor. *The Journal of Cell Biology*, 79:663–671, 1978.

[85] P.F. Davies, R.Selden 3rd S.C. Ross, and S.M. Schwartz. Enhanced rates of fluid pinocytosis during exponential growth and monolayer regeneration by cultured arterial endothelial cells. *Journal of Cellular Physiology*, 102(2):119–127, 1980. 13

[86] H. Sarin. Physiologic upper limits of pore size of different blood capillary types and another perspective on the dual pore theory of microvascular permeability. *Journal of Angiogenesis Research*, 2:14, 2010. 13, 38, 39, 41

[87] I.A. Nestorov, L.J. Aarons, P.A: Arundel, and M. Rowland. Lumping of Whole-Body Physiologcally Based Pharmacokinetic Models. *Journal of Pharmacokinetics and Pharmacodynamics*, 26(1):21–46, 1998. 14

[88] C. Brochot, J. Toth, and F.Y. Bois. Lumping in Pharmacokinetics. *Journal of Pharmacokinetics and Pharmacodynamics*, 32(5-6):719–736, 2005.

[89] I. Gueorguieva, I.A. Nestorov, and M. Rowland. Reducing Whole Body Physiologically Based Pharmacokinetic Models Using Global Sensitivity Analysis: Diazepam Case Study. *Journal of Pharmacokinetics and Pharmacodynamics*, 33(1):1–27, 2006.

[90] S. Björkman. Reduction and Lumping of Physiologically Based Pharmacokinetic Models: Prediction of the Disposition of Fentanyl and Pethidine in Human by Successively Simplified Models. *Journal of Pharmacokinetics and Pharmacodynamics*, 30(4):285–307, 2003.

[91] S. Pilari and W. Huisinga. Lumping of physiologically-based pharmacokinetic models and a mechanistic derivation of classical compartmental models. *Journal of Pharmacokinetics and Pharmacodynamics*, 37:365–405, 2010. 14, 16, 53, 54, 76, 77, 80, 86, 87, 88, 90, 98, 99, 112

[92] J.F. Lu, R. Bruno, S. Eppler, W. Novotny, B. Lum, and J. Gaudreault. Clinical Pharmacokinetics of Bevacizumab in Patients with Solid Tumors. *Cancer Therapy and Pharmacology*, 62:779–786, 2008. 15, 53

[93] P. Wiczling, M. Rosenzweig, L. Vaickus, and W.J. Jusko. Pharmacokinetics and Pharmacodynamics of a Chimeric/Humanized Anti-CD3 Monoclonal Antibody, Otelixizumab (TRX4), in Subjects With Psoriasis and With Type 1 Diabetes Mellitus. *The Journal of Clinical Pharmacology*, 50:494–506, 2010. 15, 53

[94] N.L. Dirks, A. Nolting, A. Kovar, and B. Meibohm. Population pharmacokinetics of cetuximab in patients with squamous cell carcinoma of the head and neck. *Journal of Clinical Pharmacology*, 48:267–278, 2008. 15, 53

[95] N. Azzopardi, T. Lecomte, D. Ternant, F. Piller, M. Ohresser, H. Watier, E. Gamelin, and G. Paintaud. Population Pharmacokinetics and Exposition-PFS Relationship of Cetuximab in Metastatic Colorectal Cancer. *Population Approach Group Meeting*, 2010. 15, 53

[96] J.J. Lammerts van Bueren, W.K. Bleeker, H.O. Bogh, M. Houtkamp, J. Schuurman, J.G.J. van de Winkel, and P.W.H.I. Parren. Effect of Target Dynamics on Pharmacokinetics of a Novel Therapeutic Antibody against the Epidermal Growth Factor Receptor: Implications for the Mechanisms of Action. *Cancer Research*, 66(15):7630–7638, 2006. 15, 53

[97] DE. Mager and WJ. Jusko. General Pharmacokinetic Model for Drugs Exhibiting Target-Mediated Drug Disposition. *Journal of Pharmacokinetics and Pharmacodynamics*, 28:507–532, 2001. 15, 63, 71

[98] D.E. Mager and W. Krzyzanski. Quasi-Equilibrium Pharmacokinetic Model for Drugs Exhibiting Target-Mediated Drug Disposition. *Pharmaceutical Research*, 22:1589–1596, 2005.

[99] L. Gibiansky, E. Gibiansky, T. Kakkar, and P. Ma. Approximations of the target-mediated drug disposition model and identifiability of model parameters. *Journal of Pharmacokinetics and Pharmacodynamics*, 35:573–591, 2008. 71

[100] H.P. Grimm. Gaining insights into the consequences of target-mediated drug disposition of monoclonal antibodies using quasi-steady-state approximations. *Journal of Pharmacokinetics and Pharmacodynamics*, 36:407–420, 2009. 63

[101] BF. Krippendorff, K. Kuester, C. Kloft, and W. Huisinga. Nonlinear pharmacokinetics of therapeutic proteins resulting from receptor mediated endocytosis. *Journal of Pharmacokinetics and Pharmacodynamics*, 36:239–260, 2009. 15, 63, 67, 71

[102] H.A. El-Masri and C.J. Portier. Physiologically Based Pharmacokinetics Model of Primidone and Its Metabolites Phenobarbital and Phenylethylmalonamide in Humans, Rats, and Mice. *Drug Metabolism and Disposition*, 26(6):585–594, 1998. 20, 22, 38, 39, 40

[103] R. Kawai, M. Lemaire, J.L. Steimer, A. Bruelisauer, W. Niederberger, and M. Rowland. Physiologically Based Pharmacokinetic Study on a Cyclosporine Derivative, SDZ IMM 125. *Journal of Pharmacokinetics and Pharmacodynamics*, 22(5):327–365, 1994. 20, 22, 38, 40, 45, 93

[104] RP Junghans and CL Anderson. The protection receptor for IgG catabolism is the β_2-microglobulin-containing neonatal intestinal transport receptor. *Proceedings of the national academy of sciences of the United States of America*, 93(11):5512–5516, 1996. 25, 31, 103, 105, 106

[105] J.W. Stoop, B. J. M. Zegers, P. C. Sander, and R. E. Ballieux. Serum Immunoglobulin levels in healthy children and adults. *Clinical & Experimental Immunology*, 4:101–112, 1969. 31

[106] EMA. Summary of product characteristics of cetuximab, 2014. 31

[107] EMA. Summary of product characteristics of infliximab, 2012. 31

[108] EMA. Summary of product characteristics of rituximab, 2014. 31

[109] EMA. Summary of product characteristics of trastuzumab, 2014. 31

[110] EMA. Summary of product characteristics of golimumab, 2014. 31

[111] EMA. Summary of product characteristics of tocilizumab, 2014. 31

[112] R.P. Brown, M.D. Delp, S.L. Lindstedt, L.R. Rhomberg, and R.P. Beliles. Physiological parameter values for physiologically based pharmacokinetic models. *Toxicology and Industrial Health*, 13(4)(4):407–484, 1997. 40, 78, 93

[113] A. Garg. *Investigation of the Role of FcRn in the Absorption, Distribution, and Elimination of Monoclonal Antibodies*. PhD thesis, Faculty of the Graduate School of State University of New York at Buffalo, 2007. 38, 40, 50, 107

[114] S. Akilesh, G.C. Christianson, D.C. Roopenian, and A.S. Shaw. Neonatal FcR Expression in Bone Marrow-Derived Cells Functions to Protect Serum IgG from Catabolism. *The Journal of Immunology*, 179:4580, 2007. 47, 48

[115] H.P. Montoyo, C. Vaccaro, M. Hafner, R.J. Ober, W. Mueller, and E.S. Ward. Conditional deletion of the MHC class I-related receptor FcRn reveals the sites of IgG homeostasis in mice. *PNAS*, 106(8):2788–2793, 2009. 47, 48

[116] T. Rodgers, D. Leahy, and M. Rowland. Physiologically-based pharmacokinetic modeling 1: Predicting the tissue distribution of moderate-to-strong bases. *Journal of Pharmaceutical Sciences*, 94:1259–1276, 2005. 49, 82

[117] A. Bernareggi and M. Rowland. Physiologic modeling of cyclosporin kinetics in rat and man. *Journal of Pharmacokinetics and Biopharmaceutics*, 19:21–50, 1991. 50

[118] T. Rodgers and M. Rowland. Physiologically-based pharmacokinetic modeling 2: Predicting the tissue distribution of acids, very weak bases, neutrals and zwitterions. *Journal of Pharmaceutical Sciences*, 95(6):1238–1257, 2006. 50

[119] M. Friden, B. Ljungqvist, H.Middleton, U. Bredberg, and M. Hammarlund-Udenaes. Improved measurement of drug exposure in the brain using drug-specific correction for residual blood. *Journal of Cerebral Blood Flow and Metabolism*, 30:150–161, 2010. 50

[120] S.P. Khor and M. Mayersohn. Potential error in the measurement of tissue to blood distribution ocefficients in physiological pharmacokinetic modeling. Residual Tissue Blood. I. Theoretical Considerations. *Drug Metabolism and Disposition*, 19(2):478:485, 1991. 50

[121] W. Huisinga, A. Solms, L. Fronton, and S. Pilari. Modeling interindividual variability in physiologically-based pharmacokinetics and its link to mechanistic covariate modeling. *CPT: Pharmacometrics & Systems Pharmacology*, 1(e4):1–10, 2012. 61

[122] D.E. Mager. Target-mediated drug disposition and dynamics. *Biochemical Pharmacology*, 72(1):1–10, 2006. 63, 71

[123] L. Gibiansky and E. Gibiansky. Target-mediated drug disposition model: relationships with indirect response models and application to population PK-PD analysis. *Journal of Pharmacokinetics and Pharmacodynamics*, 36:341–351, 2009.

[124] L.A. Peletier and J. Gabrielsson. Dynamics of target-mediated drug disposition. *European Journal of Pharmaceutical Sciences*, 38(5):445–464, 2009.

[125] L. Gibiansky and E. Gibiansky. Target-mediated drug disposition model for drugs that bind to more than one target. *Journal of Pharmacokinetics and Pharmacodynamics*, 37:323–346, 2010. 63, 71

[126] H. Wiig, G.A. Kaysen, H.A.. Al-Bander, M. De Carlo, L. Sibley, and E.M. Renkin. Interstitial excludion of IgG in rats tissues estimated by continuous infusion. *American Journal of Physiology*, 266:H212–H219, 1994. 65, 72

[127] H. Wiig, O. Tenstad, P.O. Iversen, R. Kalluri, and R. Bjerkvig. Interstitial fluid: the overlooked component of the tumor microenvironment? *Firbrogenesis and Tissue Repair*, 3(12):1–11, 2010. 65, 72

[128] D. Mould and K. Sweeney. The pharmacokinetics and pharmacodynamics of monoclonal antibodies mechanistic modeling applied to drug development. *Current Opinion in Drug Discovery and Development*, 10(1):84–96, 2007. 71

[129] M.A. Tabrizi and L.K. Roskos. Preclinical and clinical safety of monoclonal antibodies. *Drug Discovery Today*, 12(13-14):540–547, 2007. 71

[130] H.C. Kimko and S.B. Duffull. Simulation for designing clinical trials: A pharmacokinetic-pharmacodynamic modeling perspective. *Drugs and the Pharmaceutical Sciences*, 2003. 75

[131] X. Hashimoto and B.S. Sheiner. Designs for population pharmacodynamics: value of pharmacokinetic data and population analysis. *Journal of Pharmacokinetics and Biopharmaceutics*, 19(3):333–353, 1991. 75

[132] E.N. Jonsson, J.R. Wade, and M.O. Karlsson. Comparison of some practical sampling strategies for population pharmacokinetic studies. *Journal of Pharmacokinetics and Biopharmaceutics*, 24(2):245–263, 1996.

[133] E.N. Jonsson and M.O. Karlsson. Automated covaraite model building with NONMEM. *Pharmaceutical Research*, 15(9):1463–1468, 1998. 75

[134] F. Mentré and A. Mallet. Handling covariates in population pharmacokinetics. *International Journal of Bio-Medical Computing*, 36:25–33, 1994. 75

[135] S.B. Duffull, D.F.B. Wright, and H.R. Winter. Interpreting population pharmacokineticpharmacodynamic analyses—a clinical viewpoint. *British Journal of Clinical Pharmacology*, 71:807–814, 2011. 75

[136] C.F. Minto, T.W. Schnider, T.D. Egan, E. Youngs, H.J.M. Lemmens, P.L. Gambus, V. Billard, J.F. Hoke, K.H.P. Moore, K.T. Hermann, D.J. abd Muir, J.W. Mandema, and S.L. Shafer. Influence of Age and Gender on the Pharmacokinetics and Pharmacodynamics of Remifentanil: I. Model Development. *Anesthesiology*, 86(1):10–23, 1997. 75, 99

[137] T.W. Schnider, C.F. Minto, P.L. Gambus, C. Andresen, D.B. Goodale, S.L. Shafer, and E.J. Youngs. The Influence of Method of Administration and Covariates on the Pharmacokinetics of Propofol in Adult Volunteers. *Anesthesiology*, 88(5):1170–1182, 1998.

[138] U.S. Department of Health, Human Services, FDA, CDER, and CBER. *Guidance for Industry: Population Pharmacokinetics*, 1999.

[139] A. Sansone-Parsons, G. Krishna, J. Simon, P. Soni, B. Kantesaria, J. Herron, and R. Stoltz. Effects of Age, Gender, and Race/Ethnicity on the Pharmacokinetics of Posaconazole in Healthy Volunteers. *Antimicrobial Agents and Chemotherapy*, 51(2):495–502, 2007.

[140] M. Joerger. Covariate Pharmacokinetic Model Building in Oncology and its Potential Clinical Relevance. *The AAPS Journal*, 14(1):119–132, 2012. 75, 99

[141] M. Jamei, G.L. Dickinson, and A. Rostami-Hodjegan. A framework for assessing inter-individual variability in pharmacokinetics using virtual human populations and integrating general knowledge of physical chemistry, biology, anatomy, physiology and genetics: A tale of 'bottom-up' vs 'top-down' recognition of covariates. *Drug Metabolism and Pharmacokinetics*, 24:53–75, 2009. 75, 94, 99

[142] S. Willmann, K. Höhn, A. Edginton, M. Sevestre, J. Solodenko, W. Weiss, J. Lippert, and W. Schmitt. Development of a Physiologically-Based Whole-Body Population Model for Assessing the Influence of Individual Variability on the Pharmacokinetics of Drugs. *Journal of Pharmacokinetics and Pharmacodynamics*, 34(3):401–431, 2007. 83, 94

[143] P.S. Price, R.B. Conolly, C.F. Chaisson, E.A. Gross, J.S. Young, E.T. Mathis, and D.R. Tedder. Modeling interindividual variation in physiological factors used in PBPK models of humans. *Critical Reviews in Toxicology*, 33(5):469–503, 2003. 79, 80, 83, 85, 86, 90, 94

[144] F. Yang, X. Tong, R.N. McCarver, D.G. andHines, and D.A. Beard. Population-based analysis of methadone distribution and metabolism using an age-dependent physiologically based pharmacokinetic model. *Journal of Pharmacokinetics and Pharmacodynamics*, 33:485–518, 2006.

[145] J.F. Young, R.H. Luecke, B.A. Pearce, T. Lee, H. Ahn, S. Baek, H. Moon, D.W. Dye, T.M. Davis, and S.J. Taylor. Human organ/tissue growth algorithms that include obese individuals and black/white population organ weight similarities from autopsy data. *Journal of Toxicology and Environmental Health*, 72:527–540, 2009. 75, 94, 99

[146] International Commission on Radiological Protection (ICRP). *Basic Anatomical and Physiological Data for Use in Radiological Protection: Reference values*. In ICRP Publication 89, 2002. 77, 78, 79, 80

[147] B.J. Andersen and N.H.G. Holford. Mechanism-based concepts of size and maturity in pharmacokinetics. *Annual Review of Pharmacology and Toxicology*, 48:303–332, 2008. 79, 112

[148] P.Y. Han, S.B. Duffull, C.M.J. Kirkpatrick, and B. Green. Dosing in obesity: A simple solution to a big problem. *Clinical Pharmacology and Therapeutics*, 82:743–744, 2007. 80

[149] S. Janmahasatian, S.B. Duffull, S. Ash, N.M. Byrne, B. Green, and L.C. Ward. Quantification of lean bodyweight. *Clinical Pharmacokinetics*, 44(10):1051–1061, 2005. 80

[150] R.D. Mosteller. Simplified calculation of body-surface area. *The New England Journal of Medicine*, 317(17):1098, 1987. 81

[151] J.K.J. Li. *Dynamics of the vascular system*. World Scientific Publishing Co. Pte. Ltd., 2004. 81

[152] E.H. Starling and M.B. Visscher. The regulation of the energy output of the heart. *The Journal of Physiology*, 62(3):243–261, 1929. 81

[153] S.L. Bacharach, M.V. Green, J.S. Borer, J.E. Hyde, S.P. Farkas, and G.S. Johnston. Left-ventricular peak ejection rate, filling rate, and ejection fraction-frame rate requirements at rest and exercise: Concise communication. *Journal of Nuclear Medicine*, 20(3):189–193, 1979. 81

[154] J.K. Alexander. Obesity and cardiac performance. *The American Journal of Cardiology*, 14(6):860–865, 1964. 82

[155] H.W. Hense, B. Gneiting, M. Muscholl, U. Broeckel, B. Kuch, A. Doering, G.A.J. Riegger, and H. Schunkert. The associations of body size and body composition with left ventricular mass: Impacts for indexation in adults. *Journal of the American College of Cardiology*, 32(2):451–457, 1998. 82

[156] F.E. Dewey, D. Rosenthal, D.J. Murphy Jr, V.F. Froelicher, and E.A. Ashley. Does size matter?: Clinical applications of scaling cardiac size and function for body size. *Circulation*, 117(17):2279–2287, 2008. 82

[157] S.R. Daniels, T.R. Kimball, J.A. Morrison, P. Khoury, S. Witt, and R.A. Meyer. Effect of lean body mass, fat mass, blood pressure, and sexual maturation on left ventricular mass in children and adolescents: Statistical, biological, and clinical significance. *Circulation*, 92(11):3249–3254, 1995. 82

[158] J.N. Bella, R.B. Devereux, M.J. Roman, M.J. O'Grady, T.K. Welty, R.R. E.T. Lee, Fabsitz, and B.V. Howard. Relations of left ventricular mass to fat-free and adipose body mass: The strong heart study. *Circulation*, 98(23):2538–2544, 1998. 82

[159] S.M. Wallace and R.K. Verbeeck. Plasma protein binding of drugs in the elderly. *Clinical Pharmacokinetics*, 12(1):41–72, 1987. 82, 112

[160] J. Woo. Age-related changes in protein binding of drugs: implications for therapy. *Journal of the Hong Kong geriatrics society*, 9(1):14–17, 1999.

[161] M.K. Grandisson and F.D. Boudinot. Age-related changes in protein binding of drugs: implications for therapy. *Clinical Pharmacokinetics*, 38(3):271–290, 2000. 82, 112

[162] T. Rodgers and M. Rowland. Physiologically based pharmacokinetic modeling 2: Predicting the tissue distribution of acids, very weak bases, neutrals and zwitterions. *Journal of Pharmaceutical Sciences*, 95(6):1238–1257, 2006. Errata in Journal of pharmaceutical sciences, 96, 2007. 82, 95

[163] G.L. De La Grandmaison, I. Clairand, and M. Durigon. Organ weight in 684 adult autopsies: new tables for a Caucasoid population. *Forensic Science International*, 119(2):149–154, 2001. 83, 84, 86, 112

[164] A. Sheikhazadi, S.S. Sadr, M.H. Ghadyani, S.K. Taheri, A.A. Manoucherhri, B. NAzparvar, O. Mehrpour, and M. Ghorbani. Study of the normal internal organ weights in Tehrans̀ population. *Journal of Forensic and Legal Medicine*, 17:78–83, 2010. 86

[165] T.N. Johnson and A. Rostami-Hodjegan. Resurgence in the use of physiologically based pharmacokinetic models in pediatric clinical pharmacology: parallel shift

in incorporating the knowledge of biological elements and increased applicability to drug development and clinical practice. *Pediatric Anesthesia*, 21:291–301, 2011. 94

[166] K.M. Flegal, J.A. Shepherd, A.C. Looker, B.I. Graubard, L.G. Borrud, C.L. Ogden, T.B. Harris, J.E. Everhart, and N. Schenker. Comparisons of percentage body fat, body mass index, waist circumference, and waist-stature ratio in adults. *The American Journal of Clinical Nutrition*, 89:500–508, 2009. 94

[167] J.J. Reilly. Assessment of obesity in children and adolescents: synthesis of recent systematic reviews and clinical guidelines. *Journal of Human Nutrition and Dietetics*, 23:205–211, 2010.

[168] A.M. Nevill, A. Stavropoulos-Kalinoglou, G.S. Metsios, Y. Koutedakis, R.L. Holder, G.D. Kitas, and M.A. Mohammed. Inverted BMI rather than BMI is a better proxy for percentage of body fat. *Annals of Human Biology*, 38:681–684, 2011. 94

[169] Greenblatt D. J. Divoll B. S. M. Abernethy, D. R. and R. I. Shader. Prolonged accumulation of diazepam in obesity. *Journal of clinincal pharmacology*, 23:369–376, 1983. 95

[170] L. Aarons, M.O. Karlsson, F. Mentré, F. Romboutd, J.-L. Steimer, and A. van Peer. Role of modelling and simulation in Phase I drug development. *European Journal of Pharmaceutical Sciences*, 13(2):115–122, 2001. 95

[171] J.Y. Chien, S. Friedrich, M.A. Heathman, D.P. de Alwis, and V. Sinha. Pharmacokinetics/pharmacodynamics and the stages of drug development: Role of modeling and simulation. *The AAPS journal*, 7(3):E544–E559, 2005. 95

[172] J.C. Lagarias, J. A. Reeds, M. H. Wright, and P. E. Wright. Convergence Properties of the Nelder-Mead Simplex Method in Low Dimensions. *Journal of Optimization*, 9(1):112–147, 1998. 103

[173] S. Pilari. *Novel approaches to mechanistic pharmacokinetic / pharmacodynamic modeling Lumping of PBPK models and system biology*. PhD thesis, Freie Universität Berlin, 2011. 104

[174] S.J. Shire, Z. Sharokh, and J. Liu. Challenges in the Development of High Protein Concentration Formulations. *Journal of Pharmaceutical Sciences*, 93(6):1390–1402, 2004. 105

[175] A.L. Daugherty and R.J. Mrsny. Formulation and delivery issues for monolclonal antibody therapeutics. *Advanced Drug Delivrey Reviews*, 58:686–706, 2006.

[176] W. Wang, S. Singh, D.L. Zeng, K. King, and S. Nema. Antibody Structure, Instability, and Formulation. *Journal of Pharmaceutical Sciences*, 96:1–26, 2007.

[177] W. Wang, E.Q. Wang, and J. Balthasar. Monoclonal Antibody Pharmacokinetics and Pharmacodynamics. *Clinical Pharmacology and Therapeutics*, 84(5):548–58, 2008.

[178] S. Spencer, D. Bethea, T.S. Raju, J. Giles-Komar, and Y. Feng. Solubility evaluation of murine hybridoma antibodies. *mAbs*, 4:3:319–325, 2012. 105

[179] NHANES III. Centers for disease control and prevention (CDC). national center for health statistics (NCHS). national health and nutrition examination survey data. Technical report, Hyattsville, MD: U.S. Department of Health and Human Services, Centers for Disease Control and Prevention, 1988-1994. 111, 112

Declaration of Originality

I declare that this is a true copy of my thesis and that this thesis has not been submitted for a higher degree to any other University or Institution. Information derived from the work of others has been acknowledged in the text and references are given in the bibliography.

Basel, 14/11/2014

LudivineFronton